University of Washington
Department of Civil and Environmental Engineering

ASSESSING THE INFLUENCE OF DIGITAL ELEVATION MODEL RESOLUTION ON HYDROLOGIC MODELING

Anthony M. Dubin
Dennis P. Lettenmaier

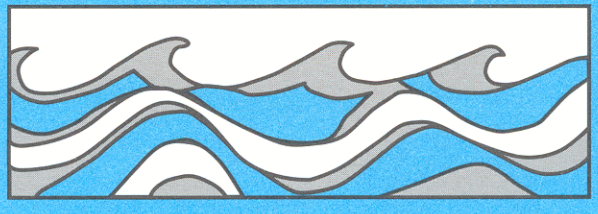

Water Resources Series
Technical Report No.159
January 1999

Seattle, Washington
98195

Department of Civil Engineering
University of Washington
Seattle, Washington 98195

ASSESSING THE INFLUENCE OF DIGITAL ELEVATION MODEL RESOLUTION ON HYDROLOGIC MODELING

Anthony M. Dubin
Dennis P. Lettenmaier

Water Resources Series
Technical Report No. 159

January 1999

Abstract

A digital elevation model (DEM) derived from aircraft synthetic aperture radar (AirSAR) C-band interferometry flown on board the NASA DC-8 during the Fall 1996 Pacific Rim Mission was evaluated for the Paul Creek and Tarrawarra catchments in Victoria, Australia. The AirSAR DEM had an absolute vertical error of 3 m and a relative vertical error of 1.2 m when compared with a high quality 5 m DEM supplied by Andrew Western and Rodger Grayson (Melbourne University) for the 10.2 Ha Tarrawarra catchment. High frequency noise, which was evident in a DEM derived from Shuttle-born SIR-C interferometry previously analyzed at Mahantango Creek, PA was not present in the AirSAR DEM for Tarrawarra. The AirSAR DEM was further evaluated using hydrologic model simulations for the larger 21 km^2 Paul Creek catchment, for pixel sizes ranging from the 10 m native resolution, up to 200m. The simulated peak flows were most sensitive to pixel size for storms in which near surface quickflow (without complete soil column saturation) dominates the hydrologic response. In simulations where saturation excess was dominant, model pixel size had less effect.

TABLE OF CONTENTS

List of Figures

Number *Page*

LIST OF TABLES

ACKNOWLEDGEMENTS

The research described in this report is based on the Masters thesis of the first author, funding for which was provided by the National Aeronautics and Space Administration. The advice of University of Washington Professors Stephen Burges and Derrick Booth, who served on the first author's thesis committee, is greatly appreciated.

Thanks also go to the many people who provided support for this project. Andrew Western of the University of Melbourne provided background information on his field investigation within the Tarrawarra catchment, as well as topographic and meteorological and stream flow data used in support of our hydrologic modeling effort. Tim Green of CSIRO provided preliminary information on the Tarrawarra and Paul Creek catchments and facilitated communication with various Australian government agencies for the difficult task of data gathering. Paul Pretto of the University of Melbourne provided the written observational and stream gauging records for Paul Creek. Ellen O'Leary and Eric Fielding of the NASA Jet Propulsion Laboratory provided specifications of the Airborne Synthetic Aperture Radar equipment, the NASA 1996 Pacific Rim Mission, and their interferometric data processing techniques, and most importantly, the processed ASAR digital topographic data used in this study. Mark Imhof and Ruth Lourey of the Victoria Department of Natural Resources located a soil survey (performed some 45 years ago) of the Paul Creek area, and provided us with the data. Finally, thanks go to graduate students and staff members in the University of Washington Hydrology Group, including Tracey Kenward, Bart Nijssen, Pascal Storck, Jonathan LaMarche, Laura Bowling, Bernt Matheussen and Greg O'Donnell, who assisted with various aspects of the modeling and data processing.

CHAPTER 1: INTRODUCION

The use of spatial data in hydrological research has expanded rapidly in the past decade. This trend can be attributed to advances in computing capability, data availability and the emergence of Geographical Information Systems (GIS) as tools for management and display of spatial data. These advances have led to a new generation of hydrologic models that incorporate spatially distributed data into simulations of watershed conditions. At the same time, remote sensing of terrestrial features for use in hydrology has become increasingly common. One feature which is particularly amenable to remote sensing is surface topography. Remote sensing instruments have the potential to provide cost-effective, fine resolution and high accuracy digital elevation models (DEMs). As DEMs availability and utilization within hydrologic models have increased, the effect of data quality has become an area of interest.

Previously studies have established that a relationship exists between digital elevation model (DEM) pixel size and various topographically derived parameters of interest in hydrology, such as slope and contributing area (Wolock and Price, 1994; Garbrecht and Mertz, 1994). As pixel size is increased, extreme topographic features are averaged out and catchment parameters tend towards a mean value (Figure 1.1). This narrows the distribution of topographic features and reduces the accuracy to which catchment boundaries and drainage features can be extracted. In addition, the effect of aggregation on catchment parameters such as elevation and slope is non-linear, as is the relationship between pixel size and catchment response. Previous studies have mostly used the topography-based, semi-distributed TOPMODEL (Beven and Kirkby, 1979; Quinn et al., 1995) to demonstrate that increasing DEM pixel size reduces the model's ability to reproduce observed saturated areas, hydrograph timing and magnitude (Zhang and Montgomery, 1994; Bruneau et al., 1995). While neither of these results is surprising, they establish that integrated catchment response predicted from spatial data sets is

dependent upon the scale of investigation. However, these studies do not provide a causal relationship between DEM scale and catchment response expressed in terms of constituent hydrologic processes.

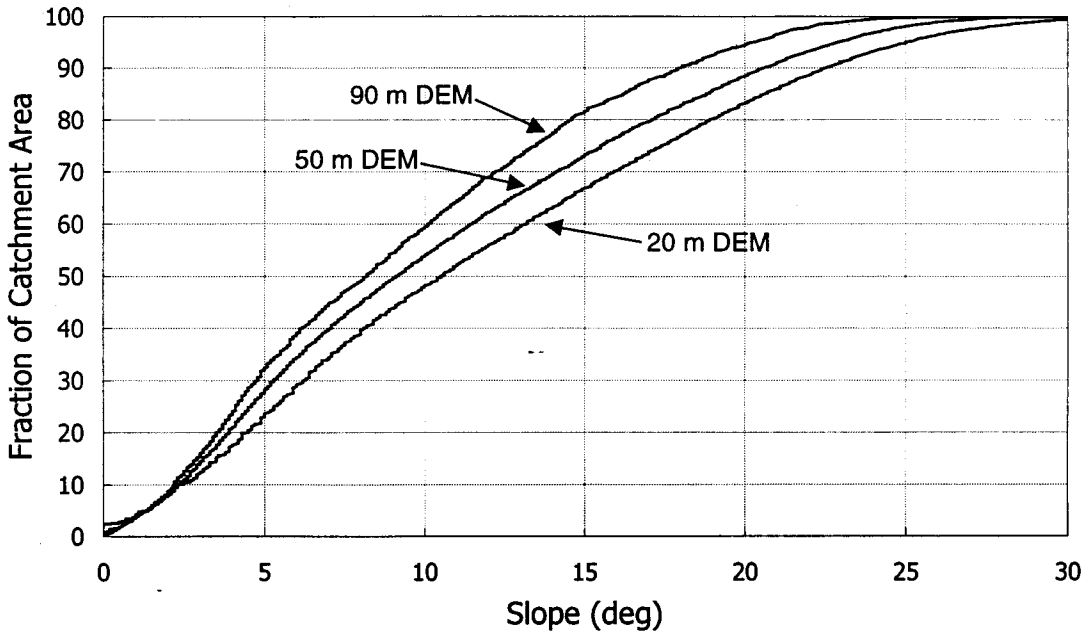

Figure 1.1 Schematic representation of the distribution of slopes within a catchment for 20, 50 and 90 m DEMs. Aggregation smoothes topography resulting in fewer steep slopes.

In this study a different tool is used to assess hydrologic response as a function of topographic grid scale: an explicit physical-process driven, spatially distributed catchment hydrology model. Distributed, physically based hydrologic models use mathematical equations that describe to varying degrees the processes that contribute to catchment response to precipitation. The use of physical relationships gives some confidence to a model's ability to predict hydrological fluxes beyond the range of the initial testing data (Abbott et al., 1986; Grayson et al., 1992a). The use of spatial data (topography, soils, vegetation) within the framework of physical models allows direct

testing of scale-dependence in terms of the constituent hydrologic processes that generate catchment response.

Spatially distributed, physically based hydrologic models have evolved considerably over the last decade. They have been used to assess the effects of land-use changes, the connection between field-scale observations and model parameters, methods of model calibration and many other applications (Grayson et al., 1992a; Refsgaard, 1997; Bowling and Lettenmaier, 1997). However, the fundamental question of finding an appropriate spatial scale remains. Typically, models are run at either the scale of the finest DEM available, or at the next finest scale that provides an acceptable model computation time. In the past several years, remote sensing has increased the amount of spatial data available for hydrologic models, and the application of remote sensing is expected to expand greatly in the coming decades (NASA, 1995). When available, remote sensing data often have finer horizontal and vertical resolutions. As the accuracy of remote sensing of topography improves, the question of how DEM quality affects hydrologic model predictions must be addressed in order to derive suitable goals for remote sensing instruments.

Kenward and Lettenmaier (1997) showed that distributed hydrology model predictions are sensitive to vertical DEM resolution by comparing hydrologic modeling results using three different DEM products for the 7.2 km^2 catchment at Mahantango, PA: a high-quality reference DEM produced from low altitude stereo-photography, a standard USGS DEM and a DEM derived from the Shuttle Imaging Radar (SIR-C) flown aboard the space shuttle Columbia. In comparison with the reference DEM, the USGS and SIR-C DEMs had errors in the spatial distribution of elevations, and the SIR-C DEM had a large vertical offset. These differences, particularly for the SIR-C DEM, resulted in errors in the model's representation of catchment boundaries, slopes and stream networks, which in turn affected model estimates of storm flows, average flows, and saturated areas. The DEMs were compared at 30 m pixel size, so the differences in elevations were attributable to vertical accuracies of the individual data sets.

This investigation follows an approach similar to that pursued by Kenward and Lettenmaier (1997) in determining the required DEM accuracy for hydrologic prediction purposes. A 10 m DEM derived from NASA's Aircraft Synthetic Aperture Radar (AirSAR; Zebker et al., 1992) was evaluated for vertical and positional accuracy. This DEM was then spatially aggregated, creating DEMs at various pixel sizes up to 200 m. Each of these DEMs were used with a spatially distributed, physically based hydrologic model to evaluate the effect of spatial resolution on hydrologic model predictions. The specific objectives and methods are described in the following sections of this chapter.

1.1 OBJECTIVES

The broad goal of this investigation is to improve the understanding of the connection between spatial data quality and hydrologic prediction. The specific objectives of this study are as follows:

- To evaluate the potential of topographic data collected using aircraft-based interferometric synthetic aperture radar
- To investigate the impact of horizontal DEM resolution on the predictions of a spatially distributed, physically based hydrology model

1.2 HORIZONTAL RESOLUTION IN HYDROLOGIC MODELING

Before attempting to quantify the influence of pixel size on hydrologic model predictions, it is important to differentiate between catchment parameters that are observed at pixel scale and those which are disaggregated from observations at much larger scales. Soils and vegetation characteristics are two spatial data types that for most catchments have traditionally only been available at coarse resolution[1]. Provided the source soil and

[1] Some higher resolution vegetation data have become available. For example, NASA's Thematic Mapper can produce vegetation maps with resolutions of 20 to 30 m. However, for most catchments such high resolution vegetation data are still rare and require considerable ground truth efforts.

vegetation data are coarser than the model pixel size, resampling the soil and vegetation maps to match the model pixel size will not affect the hydrologic parameters derived from the maps, regardless of the particular pixel size chosen. For example, if the observed soil maps are available at $1km^2$ resolution, increasing the model pixel size from 10 m to 100 m will not result in a loss of soils information. By contrast, each DEM pixel is at least as small as each model pixel. If the model pixel size is coarser than that of the DEM, then the DEM must be aggregated accordingly. Aggregating a DEM to coarser resolutions affects the values and gradients of elevations and other topographically-defined parameters. Hydrologic processes that are modeled in terms of these topographic parameters will therefore be a function of pixel size. Therefore the differences in model predictions at different model pixel sizes are attributable to differences in topographic data rather than soils or vegetation data. Appendix A contains a broader discussion of spatial variability of soil and vegetation characteristics.

1.3 THE DISTRIBUTED HYDROLOGY SOILS VEGETATION MODEL

Since the introduction of the Systeme Hydrologique Europeen (SHE) model (Abbott et al., 1986), there has been a steady growth in use of spatially distributed, physically-based hydrology models. An increase in computing power, availability and accuracy of spatial data sets and understanding of the interactions among vegetation-soil-hydrology layers has led to improvement in both the formulation and implementation of this type of model (Grayson et al., 1992a; Garrote and Bras, 1995).

The Distributed Hydrology Soil Vegetation Model (DHSVM) is a spatially distributed, physically based hydrology model (Wigmosta et al., 1994; Bowling and Lettenmaier, 1997). Movement of water through a catchment is simulated via a detailed energy and water balance for each pixel and an explicit channel routing routine. A two-layer vegetation model includes separate overstory and understory zones with algorithms for calculation of interception, storage and vertical movement of water, accumulation and

ablation of snow, evaporation and transpiration of water from each layer, as well as associated sensible and latent fluxes (Figure 1.2). A multi-layer soil model is used to calculate the vertical and lateral distribution of water through each pixel. Infiltration rate, layer depth, porosity, field capacity, rooting zone depth and vertical and lateral soil hydraulic conductivity are used to characterize the hydraulic behavior of each soil zone. Surface flow is assumed to be generated by the saturation excess mechanism which has been shown to be the dominant means by which overland flow occurs in humid temperature, non-urban environments. Overland flow is routed through the catchment using an explicit Muskinghum - Cunge scheme (Bowling and Lettenmaier, 1997; Fread, 1993). A recent addition to the channel routing scheme is a road algorithm, developed specifically for modeling the effects of (logging) roads on channel connectivity, and the timing and magnitude of hydrologic response (Bowling and Lettenmaier, 1997; LaMarche and Lettenmaier, 1998).

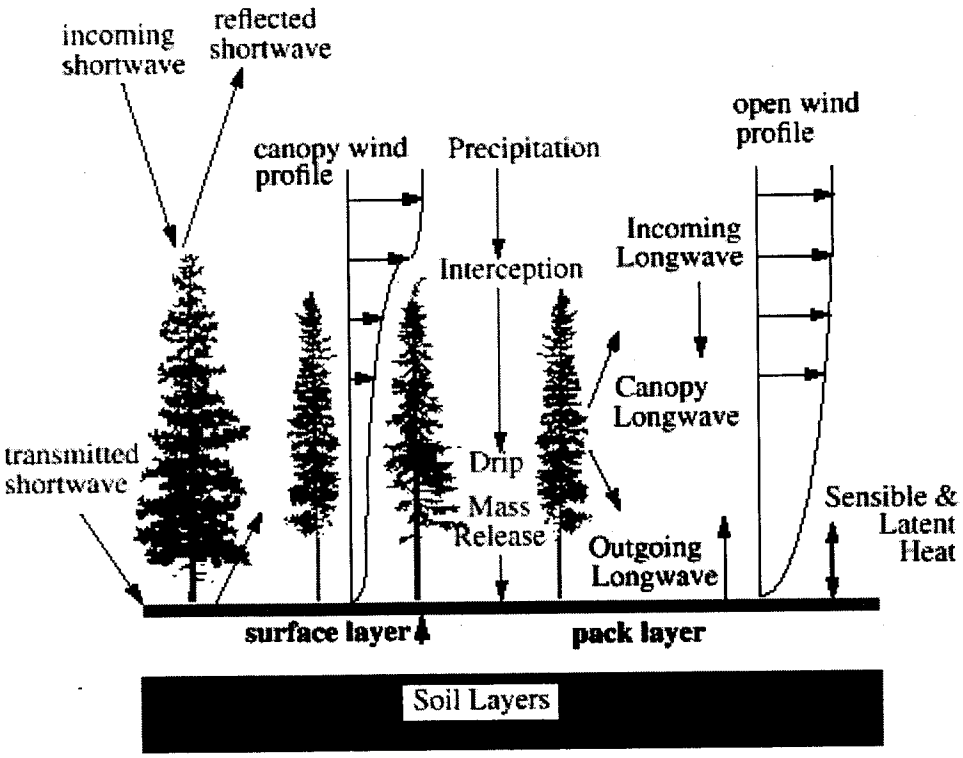

Figure 1.2 DHSVM energy balance schematic.

1.4 APPROACH

A combination of spatial analysis and hydrologic modeling was used to evaluate both the AirSAR data set and the influence of DEM pixel size on model predictions. The specific methods used are as follows:

1. The positional and vertical accuracy of the AirSAR 10 m DEM and the Australian Surveying and Land Information Group (AUSLIG) 90 m DEM were compared to the Tarrawarra 5 m DEM (Western and Grayson, 1998) at the 10.2 Ha Tarrawarra catchment located in the Upper Yarra River Basin, Victoria, Australia. This comparison was performed to establish the adequacy of the AirSAR and AUSLIG

DEMs for use in hydrological modeling studies. Adequate data sets should capture terrain features evident in the reference DEM and not possess large vertical biases. Chapter 3 contains a complete description of the analyses performed.

2. Two separate aggregation methods were used to produce coarser DEMs from the 10 m AirSAR DEM: bilinear interpolation, and a modified-fractal interpolation method (Bindlish and Barros, 1996). The influence of pixel size on DEM derived catchment parameters such as delineated area, average elevation, outlet elevation, and the distribution of slopes were calculated for a series of DEMs with pixel sizes ranging from 10 m to 200 m for the 21 km^2 Paul Creek catchment which is located adjacent to Tarrawarra. These results are presented in Chapter 4.

3. The hydrology of the Paul Creek catchment was examined at 10, 20, 30, 50, 90 and 200 m resolutions in a modeling study using the Distributed Soil Vegetation Hydrology Model (DHSVM). Various hydrological fluxes were examined at each resolution to illustrate the dependence of model prediction on DEM resolution. These model experiments are described in detail in Chapters 5 and 6.

In addition, Chapter 2 contains a review of the application of remote sensing of topography in hydrology, with particular emphasis on synthetic aperture radar and AirSAR.

CHAPTER 2: REMOTE SENSING OF TOPOGRAPHY

Over the past 3 decades, the potential for remote sensing of terrestrial features has been demonstrated in a variety of fields including urban planning, archaeology, meteorology, planetary science and earth science. Remote sensing offers important advantages over ground-based observations: large areas can be observed nearly simultaneously, and regions which are not easily accessible (e.g. polar regions) can be observed remotely. This chapter contains a overview of remote sensing technology as applied in hydrology and topographic mapping. Particular emphasis is given to synthetic aperture radar (SAR) products which have been used extensively in this investigation.

2.1 REMOTE SENSING OVERVIEW

A number of technologies have been applied to the remote sensing of the earth's surface. For topographic mapping, there are three main approaches: stereography, laser altimetry, and synthetic aperture radar. The two former techniques are discussed in this section while SAR is discussed in greater detail in the next several sections.

Aerial photography combined with photogrammetric methods of interpretation have been used extensively to develop digital elevation models, including USGS topographic maps (Lillesand and Kiefer, 1994). Separate images of the same site are created from observations at different locations. These images are combined to form a stereo pair which can be analyzed to reconstruct an elevation model. Kenward and Lettenmaier (1997) used a high-quality DEM created through stereo-correlation and low altitude photography to investigate the effects of vertical topographic resolution on hydrologic modeling at Mahantango, PA. While photogrammetry, particularly for low-altitude photography, has been shown to be an effective method for developing high resolution DEMs, there are drawbacks which prevent wider implementation of this technology.

Stereographaphic image interpretation is time consuming and as a result high resolution DEMs must be created individually for small areas (tens of square kilometers). Aerial photography can be hindered by poor weather and associated poor visibility, and ground surface observations can be limited in areas of dense vegetation.

Satellite based visible imagery has also been used for topographic and thematic mapping of the earth's surface. The Systeme Pour l'Observation de la Terre (SPOT) series of satellites (http://www.spot.com) have been collecting visible and near-infrared images since the launch of SPOT-1 in 1986. At present SPOT-2 and SPOT-3 are operational, and SPOT-4 which was launched in April, 1998 is scheduled to become fully operational in the near future. These satellites have movable optics, allowing scanning up to 27° (approximately 470 km) to the side of the craft, enabling imaging of the same location from different positions on repeat passes. These two images form a stereo pair which can be processed into a DEM using techniques similar to photogrammetry. DEMs are processed to a 20 m pixel size, with 11 – 17 m absolute vertical accuracy. Endreny et al (1998a) have performed a detailed analysis of SPOT imagery for the Little Washita River, OK watershed, minimized vertical errors in the data and assessed the influence of these errors on geomorphic variables.

More recently, laser altimeters have been used to estimate vegetation canopy and ground surface elevations (Blair, 1994; Harding, 1998). These instruments work by accurately measuring the return-trip travel time of an emitted laser pulse. The returned signal is a combination of backscattered signals from the vegetation canopy and the ground surface. A vertical profile is reconstructed to estimate both surface elevation, canopy height and structure. Because the emitted signal is highly collimated, the beam spreads very little and only a small area can be sampled with each pulse. As a result, high resolution elevation measurements are obtainable (7.5 m horizontal, < 1 m vertical; Harding, 1998), but only small swaths can be imaged. Because of its extremely narrow swath width, laser altimetry may be best suited to elevation benchmarking rather than construction of catchment-scale DEMs.

2.2 SYNTHETIC APERTURE RADAR

Synthetic aperture radar systems use advanced signal processing techniques along with the motion of the host craft (e.g. airplane, orbiting satellite) to approximate the function of a large antenna radar while using a much smaller antenna. SAR systems are active forms of radar, i.e. the instrument transmits a series of pulses (or chirps) and receives the echoed response, rendering background illumination unnecessary. Within clouds, radio frequencies are long enough to average the properties of air and water droplets, so that while some attenuation occurs the overall coherence of the radar signal remains intact. These two properties provide a distinct operating advantage over optical sensors: SAR can effectively image the ground surface day or night, regardless of the weather.

Since radar image resolution is related to the amount of information received by the SAR, maximizing the strength of the returned signal is important. The strength of the returned signal is a function of (1) the transmission power of the instrument, (2) the antenna size and (3) the fraction of the transmitted signal that is backscattered by the imaging surface. Transmission power is related to the length of each emitted pulse. Longer pulses contain more energy and consequently have a greater chance of returning to the SAR. Unfortunately, the length of the signal pulse is also inversely related to the range resolution[2] (see section 2.6.1). Generally, a pulse duration is chosen to provide both adequate signal strength and range resolution (Fitch, 1988). Different SAR instruments operate at different wavelengths. The degree of atmospheric attenuation generally increases for shorter wavelengths. However, serious atmospheric effects are mostly confined to wavelengths below 3 cm. Since SARs operate at wavelengths above 3 cm, the effects of atmospheric attenuation on the strength of the returned signal are similar in different wavebands (Lillesand and Kiefer, 1994).

---

[2] Range resolution is measured in the direction perpendicular and to the side of the craft's direction of travel. There are two variations on range resolution: ground range which is measured along the ground and slant range which is measured is the direction of the emitted pulse. Hereafter *range* refers to *ground range*.

A space-based conventional radar system capable of producing high resolution (i.e. 30 m or less) images of the ground surface would require an antenna hundreds of meters in length. However, in air and space radar applications, the size of the antenna is limited by practical constraints. To overcome the limitations of antenna size, SAR systems use the motion of the host craft along with rapid signal pulses to sample an object from many different locations, approximating the resolution of a large stationary antenna with an antenna a couple of meters long. SAR derives its name from this *synthetic* increase in effective aperture size (Figure 2.1).

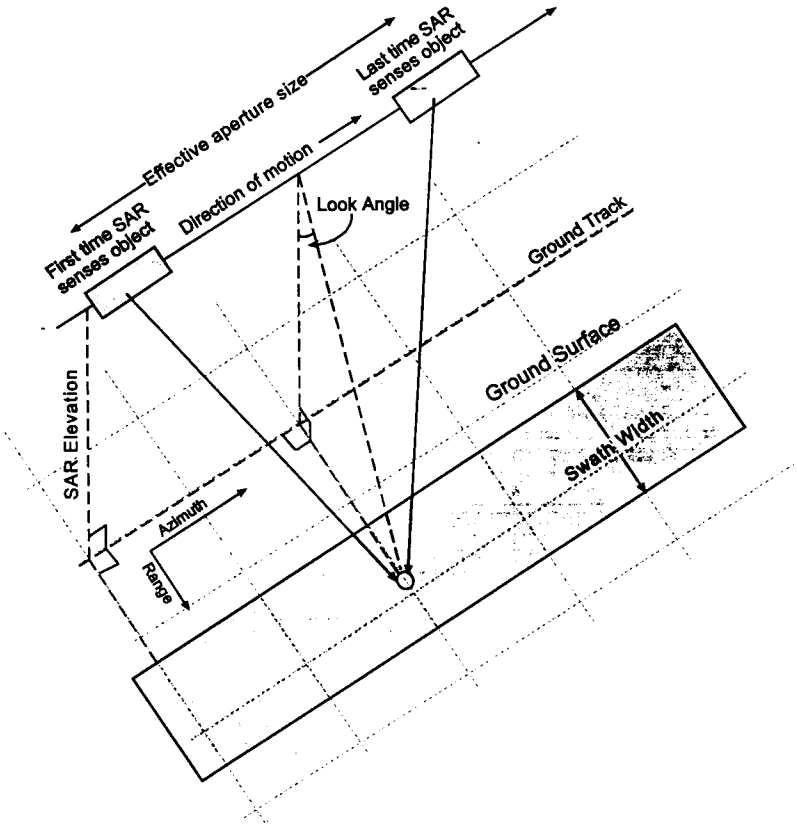

Figure 2.1 Schematic shows the increased effective aperture size of SAR system. Each ground location is scanned by the SAR from several locations. The scale in the direction of motion is greatly exaggerated relative to elevation of SAR.

Table 2.1 shows common operating wavelengths for SAR instruments. Each of these wavebands are more appropriate for certain SAR applications than others. Because

objects with surface variations at the scale of the radar wavelength tend to result in stronger backscattering, an operating wavelength is selected during the design phase based on the intended applications of the instrument. For example, leaves or small stems a few centimeters in diameter may backscatter C- and X-band radiation but allow L and P-band to partially penetrate through to the tree trunk where the remainder of the beam will be scattered (Figure 2.2). C-band radar has been shown to be sensitive to snow properties of interest to hydrologists, including snow-water equivalent and snow extent (NASA, 1995). L-band radar is able to detect soil moisture in the top 5 cm of the soils column, although present algorithms have given the best results in regions with bare soils and sparse vegetation (Dubois et al., 1995; Lin et al., 1994).

Table 2.1 Commonly implemented SAR wavelengths.

	Wavelength (cm)
X-band	3.0 - 3.75
C-band	3.75 - 7.5
L-band	15 - 30
P-band	30 - 100

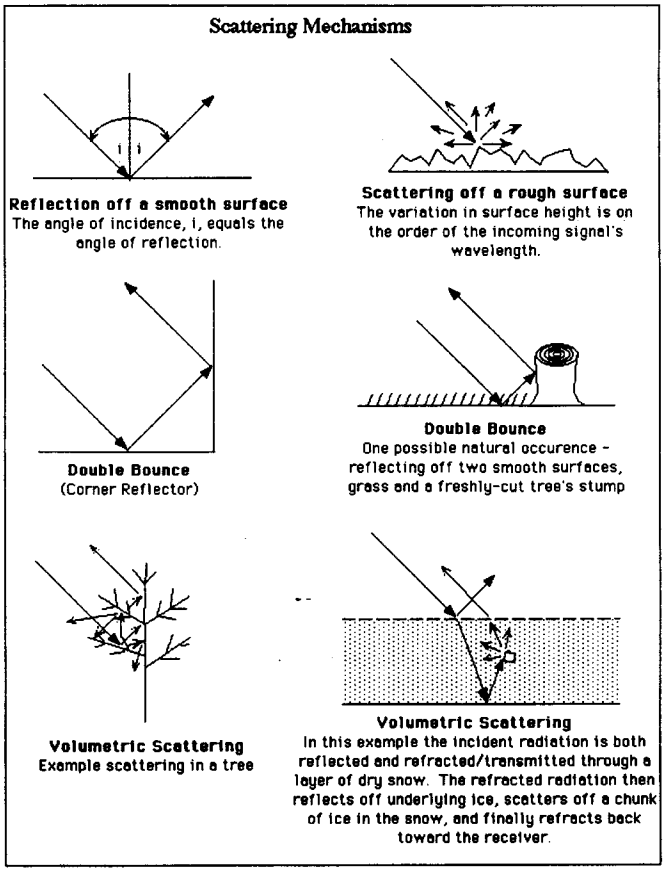

Figure 2.2 Physical examples of scattering induced by different surfaces. Source: Alaska SAR Facility (http://www.ask.alaska.edu).

2.3 PREVIOUS SPACEBORNE SARS RELEVANT TO THE GEOSCIENCES

This section describes the capabilities and accomplishments of various SARs that have been in operation during the past three decades.

SEASAT SAR:

The L-band (23 cm) SAR carried aboard Seasat was the first space-based imaging radar used for earth science observation. Launched in June, 1978, in a near-polar orbit at an altitude of 800 km, the imaging radar had a swath width of 100 km and a resolution of approximately 25 m. The primary mission of Seasat was to monitor and investigate

oceanic phenomena. Seasat SAR proved useful for determining the direction of ocean waves, manifestations of internal waves and the motion of polar ice. During its 3 month life span, there were opportunities to image large sections of North America. These images demonstrated that SAR can be used to characterize geological features, land-water interfaces, vegetation extent and other land-use patterns (Fitch, 1988). Despite these successes, Seasat SAR was limited by its short life span and its single wave length, polarization and angle of incidence.

SHUTTLE IMAGING RADAR A AND B (SIR-A AND SIR-B):

SIR-A was flown aboard the Space Shuttle Columbia in November, 1981. The SAR technology was similar to that used by Seasat. The instrument proved useful for mapping geological features, particularly in areas of low-relief (this limitation was due to SIR-A's high incidence angle). SIR-A images led to the discovery of previously unmapped sub-surface dry stream beds in Saharan Africa, showing the ability of L-band radar to penetrate through hyperarid sands to a depth of several meters. SIR-B employed a moveable antenna capable of imaging a surface with incidence angles between 15 and 60 degrees. These first multiple incidence angle images demonstrated the sensitivity of the backscatter signatures of natural surfaces to the incidence angle of the radar signal.

SHUTTLE IMAGING RADAR C (SIR-C):

Aided by the development and operation of earlier Shuttle Imaging Radar missions and early implementations of AirSAR, the SIR-C/X-SAR represented a *second-generation* of SAR instrumentation with multi-frequency, multi-polarization and variable incidence angle providing a rich polarimetric data set. For the fist time, backscatter spectra were processed on-board the spacecraft allowing direct data downlinking of processed information. The multi-parameter capability of SIR-C/X-SAR opened up a wide-range of new research opportunities and observations. Improvements included better estimation of

soil moisture for bare soil areas, areal extent of flooding and oil spills, volcanic ash deposits and lava flows, as well as snow pack coverage and snow-water equivalent.

EUROPEAN SPACE AGENCY'S REMOTE SENSING SATELLITES (ERS-1 & ERS-2):

The European Space Agency's ERS-1 has been collecting single polarization, C-band radar images of the earth from an altitude of 780 km since 1991. A twin satellite, ERS-2 was launched in 1995 and operates in orbital tandem with ERS-1. ERS-2 also carries instrumentation for the Global Ozone Monitoring Experiment (GOME) which infers the chemical composition of the atmosphere including stratospheric ozone. This mission has focused on gathering information on remote regions in the Arctic and Southern Oceans for which little was previously known. These satellites have also supported research into interferometric topographic modeling. One limitation of the ERS satellites is that no data storage capability is carried on board, meaning that data are only collected when the satellites are within range of a ground receiving station, such as the Alaska SAR Facility (ASF). The range of ASF extends to 3000 km from Fairbanks, Alaska.

JAPANESE EARTH SCIENCE RESOURCES SATELLITE (JERS-1):

JERS-1 was launched in 1992 and carries an L-band sensor which is still in operation. Unlike most of its predecessors, JERS-1 has on-board tape recorders, so images can be taken of anywhere on the globe, regardless of whether a receiving station is within transmission range. JERS-1 was designed specifically for land-surface applications, such as resource exploration, land surveying, forestry, and coastal monitoring. Operating at a longer wavelength, JERS-1 is better suited to land-surface studies than ERS satellites, because L-band SAR is able to penetrate vegetative canopies more effectively than C-band SAR. JERS-1 has been used to collect terrestrial data in support of the Global Rain Forest Mapping Study of the Amazon.

RADARSAT:

RADARSAT is a C-band, single polarization SAR operated by the Canadian Space Agency. With a variable incidence angle (20 to 50°), the instrument is capable of operating in several modes scanning 50 to 500 km swaths at resolutions of 10 to 100 m. RADARSAT carries on-board data recorders for data collection and storage outside the range of receiving stations. Launched in 1995 with an expected operational life of 5 years, the objectives of RADARSAT are to produce daily maps of sea ice along the shipping lanes of the Arctic Ocean and Hudson Bay, a global set of stereographic SAR images, Antarctic maps and soil moisture measurements for crop forecasting.

2.4 APPLICATION OF SAR TO TOPOGRAPHIC MAPPING:

SAR can be used to infer the spatial and temporal distribution of hydrologically important surface variables over large areas. Variables amenable to remote sensing include topography, snow extent, snow-water equivalent, near-surface soil moisture, land-use characteristics and biomass estimation. Remote sensing data are commonly used in support of modeling studies at all scales, from global circulation models (GCMs) to catchment-scale hydrology models such as DHSVM. Because a remote sensing DEM has been used in this modeling investigation, the application of SAR to topographic mapping is emphasized in this section.

2.4.1 TOPOGRAPHY

Topography controls the movement of moisture through a catchment, both at the surface and subsurface. Traditionally, topographic maps have been created either through extensive field surveys or from aerial photography. Consequently, regions with difficult access and/or limited economic and technical resources have been relatively sparsely mapped. This has not been a problem in the U.S. because the USGS has produced gridded topographic maps of the contiguous states at 3 arc second (~90 m) resolution or

higher, although substantial errors in these data sets have been previously documented (Carter, 1989). Kenward and Lettenmaier (1997) showed that vertical errors in USGS and SIR-C DEMs had a significant effect on hydrologic model predictions, making the case for more accurate DEMs to support modeling studies. Topographic data derived from single instrument interferometric SAR can be used to generate high-resolution images of remote regions with a minimum of ground-truthing. SAR operating in tandem with similar orbital patterns, like ERS-1 and ERS-2 can function as an interferometer with the distance separating the instruments (in the direction perpendicular to the flight line) forming an interferometric baseline. In some applications, interferometric SAR systems have shown promise for developing high resolution topographic maps in a cost effective manner. In flatter terrain, SAR DEMs have compared favorably with other methods of DEM development (Zebker et al., 1992). Some earlier applications of SAR to have suffered from large vertical offsets and fine-scale vertical variability similar to white noise (Kenward and Lettenmaier, 1997).

2.5 AIRCRAFT SYNTHETIC APERTURE RADAR (AIRSAR)

Aircraft-based SAR research has been actively pursued by NASA since the early-1970's with missions conducted using an L-band radar aboard the Ames Research Center's Airborne Laboratory. In the last decade, NASA's Jet Propulsion Laboratory (JPL) and Ames Research Center have developed an aircraft-based active multi-band, multi-polarization synthetic aperture radar (SAR) instrument, termed AirSAR. AirSAR is flown aboard NASA's DC-8 aircraft, typically at an altitude of 8 km and a speed of 750 km/h. In polarimetric mode, AirSAR transmits and receives at three microwave wavelengths: C-band (6 cm), L-band (25 cm) and P-band (70 cm), collecting multi-polarization (HH, HV and VV) backscatter characteristics of the imaging surface in each waveband. A C-band radar interferometer (TOPSAR) has been added to the AirSAR platform for topographic imaging. The interferometer is formed by two oppositely polarized antennae mounted on the airplane's fuselage and separated by 2 meters. While operating in

TOPSAR mode, multi-polarization backscatter data are still collected at L- and P-bands. Separate C- and L-band antennae are located near the nose of the aircraft. Together with antennae located near the wings, these form an along-track interferometer (ATI). ATI mode is useful for imaging oceanic phenomena, such as wave breaking and ocean currents. AirSAR has flown in missions over parts of the United States, Canada, Mexico, Greenland, Europe and the Pacific Rim. Currently, AirSAR is the only C, L and P-band polarimetric SAR that can collect fully polarimetric data in all three frequencies simultaneously.

2.5.1 AIRSAR OPERATIONS

While aircraft-based SAR has the potential to provide all of the benefits of space-based SAR with an added advantage of finer resolution resulting from the lower elevation of the radar, there are numerous complications associated with aircraft-based SAR which must be addressed. AirSAR flights typically begin with a warm-up period during which time a number of system features are calibrated. Unlike satellites which operate in established orbital tracks at near vacuum conditions, the DC-8 aircraft carrying AirSAR is not strictly held on course by gravitational forces and is subject to atmospheric turbulence. Pilot and crew make sure the aircraft is flying straight, level and on-course before data collection commences. To aid in navigation, a GPS antenna mounted near the nose of the aircraft and an inertial navigation system are also used. Previous implementations of AirSAR have suffered from uncertainty in the aircraft roll angle (Zebker et al., 1992), but an improved roll compensation system has since been installed. Before the start of data collection, the pre-chirp (i.e. no transmission) received signal is measured to gauge the background noise (generally small in the microwave range) and to test each of the sensors.

For each flight, data are collected for a strip of land measuring approximately 60 km along the direction of flight and 10 to 15 km wide. The actual swath width is determined by the aircraft elevation and the range of the look angle (see Figure 2.1). Data are written

directly to one of three on-board high density digital tape drives (HDDT). The HDDTs are sent directly to JPL for processing. A quick-look processor carried aboard the DC-8 is used to produce reduced resolution images within approximately 10 minutes during flight, helping the flight crew verify that the correct sites were imaged. The quick-look images are then sent to investigators for initial interpretation and to aid in deciding which regions to have fully processed.

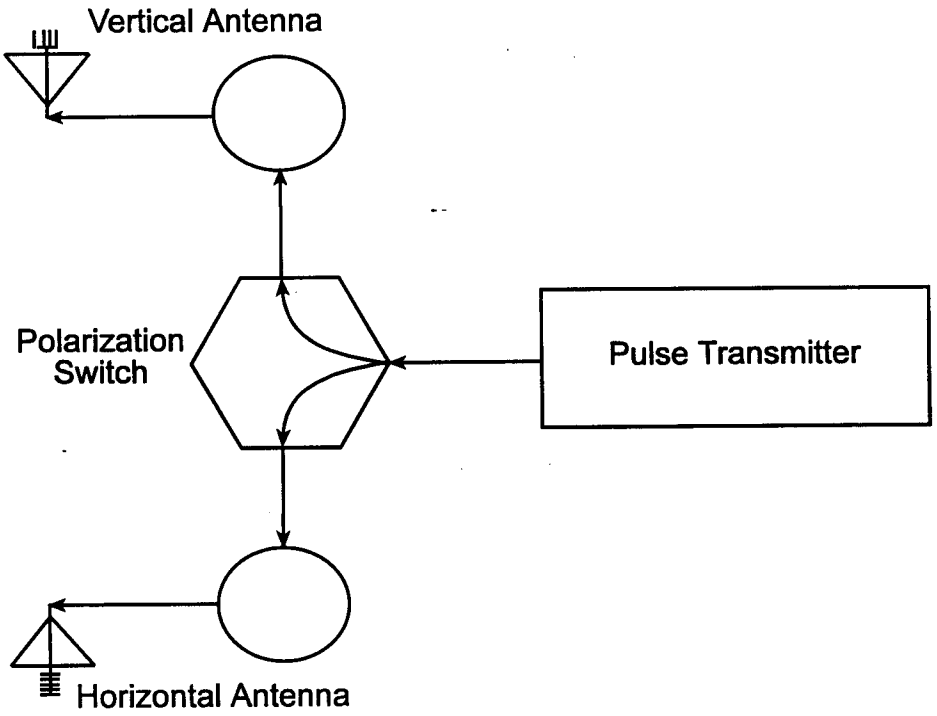

Figure 2.3 Schematic of transmission signal polarization in TOPSAR mode.

During data collection, series of digital pulses 10 μs in duration are emitted from either of two spatially separate and oppositely polarized, but otherwise identical antennae. The pulses are generated by a single transmitter, alternately polarized and sent to the appropriate antenna (Figure 2.3). The polarization switches with each emitted pulse (e.g. horizontal, vertical, horizontal, etc.). During the inter-pulse period (0.5 - 1.0 ms), each antenna receives the echoed signal oriented to its polarization. Therefore the full, 2-dimensional wave is recorded simultaneously. The received signal is entirely from a

single pulse helping to preserve the coherence of transmitted-received signal (Figure 2.4). The setup is slightly different when operating in TOPSAR mode: the interferometer consists of two C-band antennae separated by ~2.5 m, each vertically polarized. Digital pulses are transmitted from only one antenna and the echoed signal is received by both.

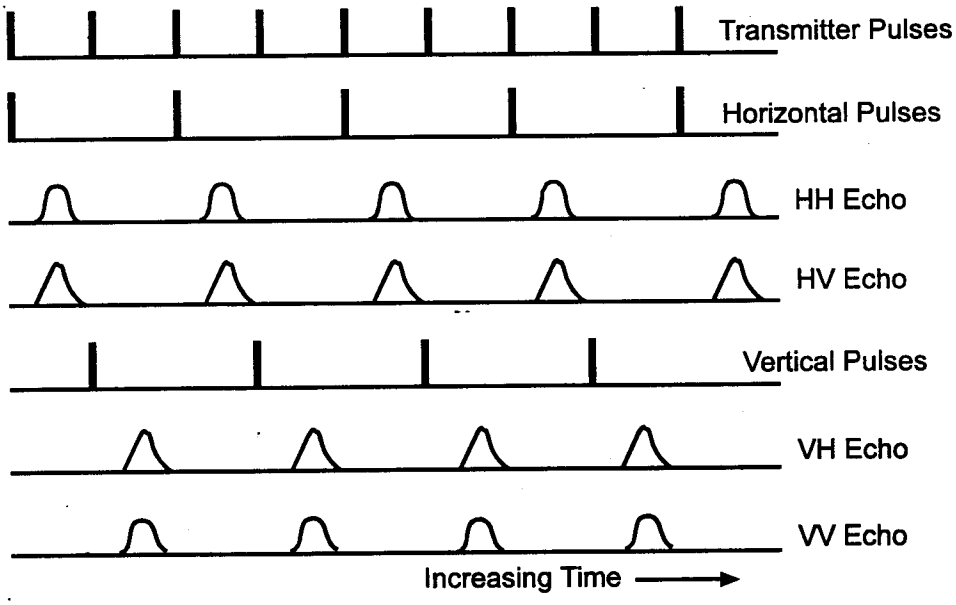

Figure 2.4 Pulses are evenly divided between vertical and horizontal polarizations. Echoes return before the next pulse preserving signal coherence. Note HV and VH are identical but sampling rate is doubled.

2.6 AIRSAR DATA PROCESSING

For conventional side-looking radar (i.e. non-SAR), the ground resolution for both the range and azimuth directions is controlled by the pulse length and the beam width of the antenna. The method for determining the range resolution for SAR systems is straight-forward and similar to non-SAR systems. Determining the azimuth resolution is more complex because of the special data collection and processing techniques used by SAR systems (see Figure 2.1). However, it is this complexity which reduces the azimuth resolution to useful levels. Both range and azimuth resolution are addressed in this section.

2.6.1 RANGE RESOLUTION

The return echo from each transmitted pulse is spread out over a period of time. The distance from the aircraft to the scattering surface is estimated from the return time of the beam, so scattering from the near range is registered before scattering from the far range. The side-looking configuration is necessary because if the antennae were oriented directly below the aircraft, the timing of the echoed signal would not correspond to a unique position but two equally likely positions. In order for two ground features to be distinguished from one another their echo patterns must be separable. In terms of transmitted pulses, this means the distance between the objects (in the range direction) must be greater than one half the pulse length. Figure 2.5 gives an illustrative example of the interference caused by two unresolved yet separate objects. If the objects are too close, rather than registering two separate bounces the scattered signals fuse together and return to the SAR in a single echo. Expressing the resolution in terms of look angle, the range resolution is given by

$$R_r = \frac{c \cdot \tau}{2\sin(\theta_{look})} \tag{1}$$

where c is the speed of light, τ is the pulse duration and θ_{look} is the look angle (see Figures 2.1 and 2.5). Clearly a short pulse duration is desirable for increased resolution, but shortening the pulse duration also reduces the strength of the transmitted signal, reducing the power of the returned signal. As a way around this problem, AirSAR emits a series of chirps at a frequency of 40 MHz within a single pulse duration. This reduces the effective pulse length and increases the range resolution. The following calculations yield range resolution (using typical AirSAR look angle values):

Near Range:
$$R_r = \frac{(3\times10^8 m/s)(40\times10^6 s^{-1})^{-1}}{2\sin(27.1)} = 8.2m \tag{2}$$

Far Range:
$$R_r = \frac{(3\times10^8 m/s)(40\times10^6 s^{-1})^{-1}}{2\sin(63.5)} = 4.2m \tag{3}$$

The near range resolution is coarser and thus forms the minimum range resolution for objects across the image swath. These figures agree with JPL documentation that report a nominal range resolution of approximately 9 m for AirSAR data.

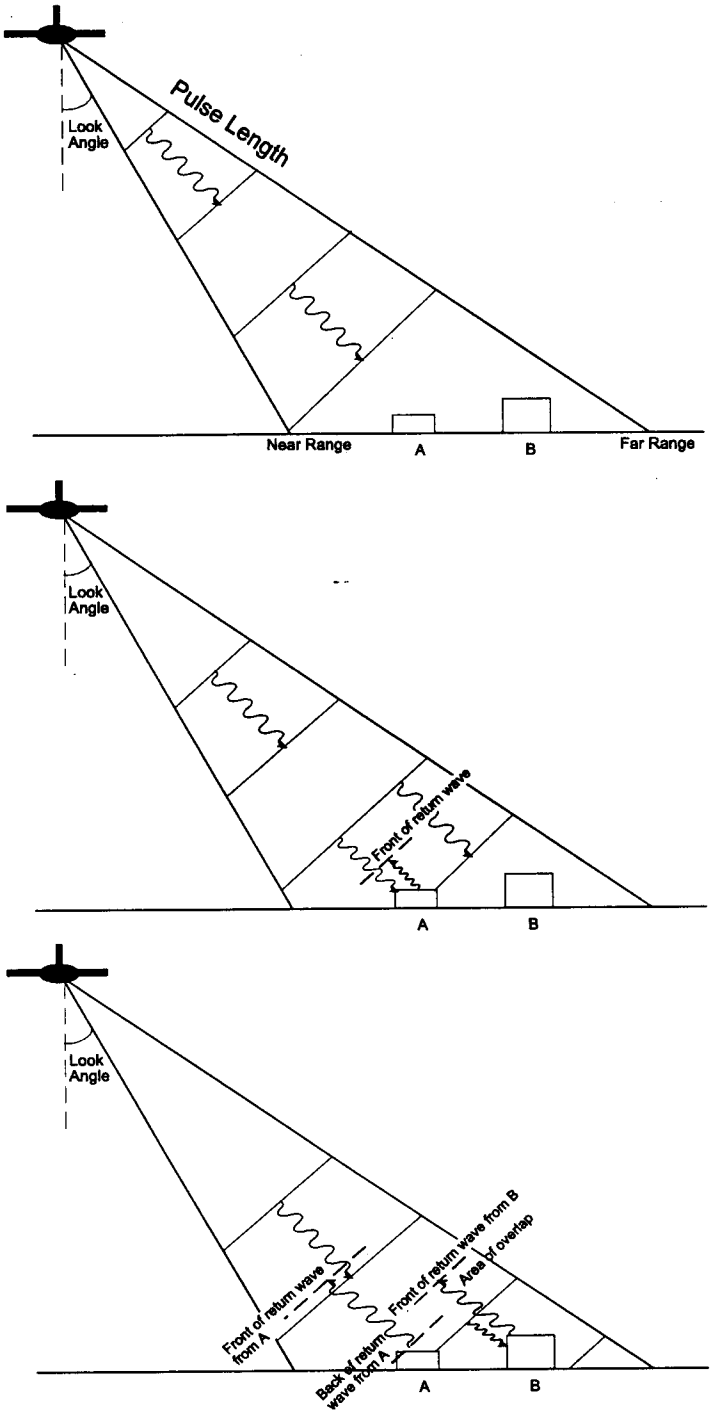

Figure 2.5 These three drawings show the time evolution of transmitted pulse. Scattering objects A and B are located too close together for the echoed signals to be completely resolved.

2.6.2 AZIMUTH RESOLUTION

For conventional side-looking radar, the azimuth resolution is calculated from the characteristic beamwidth of the antenna which is a function of the its size and wavelength. Beamwidth and azimuth resolution are given as follows:

$$\beta = \frac{\lambda}{L} \tag{4}$$

$$R_a = R_r \cdot \beta \tag{5}$$

where λ is the wavelength, L is the length of the antenna and R_r is the ground range. SAR systems narrow the effective beamwidth, discriminating the near-center section of the echoed beam by detecting Doppler shifts in the signal. The section of the beam which has spread in front of the aircraft will be shifted to higher frequencies and vice versa for the portion of the beam which spreads behind the aircraft. The narrowing of the beamwidth is often described as an effective increase in the length of the antenna. Table 2.2 gives the nominal horizontal resolutions as reported in JPL documentation accompanying the Tarrawarra and Paul Creek data sets.

Table 2.2 Resolution of AirSAR data.

	Range (m)	Azimuth (m)
C-band	9	13
L-band	9	26
P-band	9	44

2.6.3 DETERMINATION OF SURFACE ELEVATION FROM INTERFEROMETRIC SAR

It is possible to estimate the surface elevation from the timing of the echoed signal issued and received by a single antenna, but because both the look angle and the topography affect the slant range, the location of the scattering surface cannot be uniquely identified. Interferometry provides another method of precisely estimating surface elevation by recording the difference in phase of the echoed signal as observed by two spatially

separated antennae in addition to the timing of the signal. Figure 2.6 shows the geometry of the transmitted and received signals. The phase difference between the echoed pulses received at each antenna is measured and converted to a path length difference according to the following equation:

$$\delta = \frac{\lambda\phi}{2\pi} \tag{6}$$

where λ is the wavelength and ϕ is the observed phase difference between the two antennae.

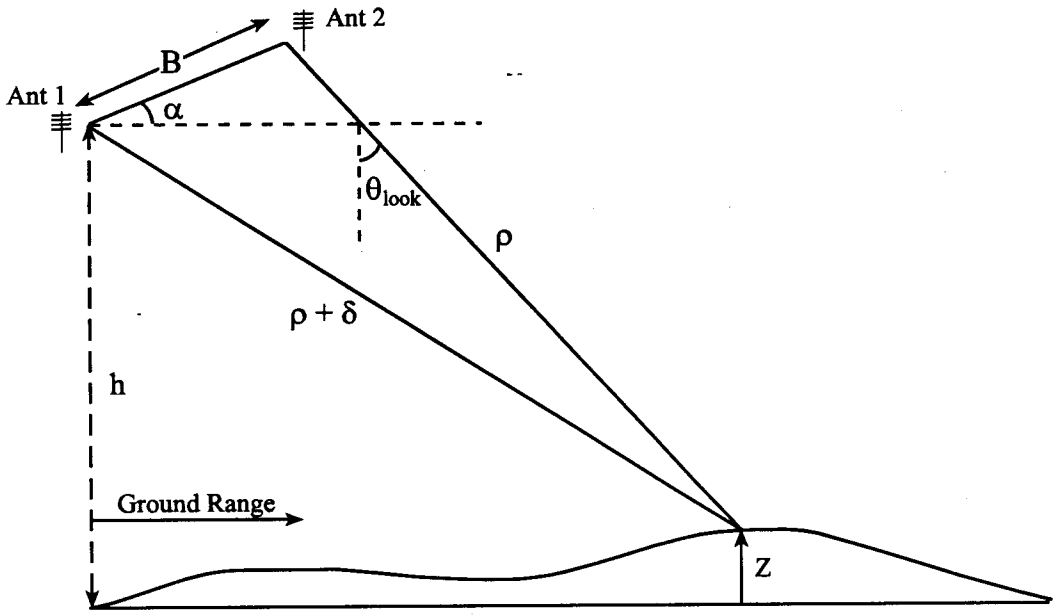

Figure 2.6 Interferometer geometry. The path length difference between antennae δ is shown. This distance is a function of the baseline B, the aircraft elevation h, the mounting angle of the antennae α, the look angle θ_{look} and the slant range ρ.

From Figure 2.6 that the surface elevation can be expressed as:

$$Z = h - r\cos(\theta_{look})$$

except that θ_{look} is not directly measured. The key is to write $\cos(\theta_{look})$ in terms of measured variables: slant range, baseline, phase difference and the mounting angle of the antenna. The first step is to expand $\cos(\theta_{look})$:

$$\cos(\theta_{look}) = \cos\{\alpha - (\alpha - \theta_{look})\} = \cos(\alpha)\cos(\alpha - \theta_{look}) + \sin(\alpha)\sin(\alpha - \theta_{look}) \quad (7)$$

With the aid of the well-known *cosine law* and system geometry:

$$\sin(\alpha - \theta_{look}) = \frac{(\rho + \delta)^2 - \rho^2 - \beta^2}{2\rho\beta} \quad (8)$$

$$z = h - \rho\cos(\alpha)\cos(\alpha - \theta_{look}) - \rho\sin(\alpha)\sin(\alpha - \theta_{look}) \quad (9)$$

An abridged version of this derivation appears in Zebker et al. (1992).

Errors in calculated surface elevation can arise from the inherent uncertainty in the following: (1) phase difference measurement, (2) aircraft attitude – in particular roll angle which translates directly into an error in look angle and (3) reconciling ground position of scattering object.

By differentiating the preceding equations, the standard deviation in the surface elevation can be described in terms of the standard deviation of the phase measurement as follows:

$$\sigma_h = \frac{\lambda\rho}{2\pi\beta}\{\sin(\alpha) - \cos(\alpha)\tan(\alpha - \theta_{look})\}\sigma_\phi \quad (10)$$

The error in elevation can thus be reduced through a combination of increasing the baseline, decreasing the wavelength, shortening the incidence angle and reducing the error in measured phase difference. There are practical limitations to these modifications. As the baseline increases, signal noise also increases up to a critical level, past which the signals are no longer correlated. Reducing the slant range also reduces the swath width, limiting the area that can be effectively sampled with a single pass. For this implementation of TOPSAR, the interferometer was designed to use as much of

AirSAR's existing hardware as possible. Since it has the shortest wavelength and the finest azimuth resolution, C-band antennae were chosen.

The other two errors mentioned arise due to unaccounted for changes in flight direction and uncertainty in the position of the aircraft. This was more of a concern in earlier implementations of AirSAR. For the 1996 Pacific Rim mission, an improved motion compensation system and a new GPS system were installed on the DC-8 aircraft.

The wave data collected at each antenna are made up of amplitude and phase components. These two images are cross-calibrated to identify the influence of experimental equipment and geometry. The images are then resampled and spatially averaged on a point-by-point basis to form the completed image product. Some georeferencing is performed on the images, but experience suggests that the geographic registration must be augmented with ground control points. Zebker et al (1992) provide a more complete discussion of TOPSAR and interferometric derivation of digital topography.

2.7 PACIFIC RIM AIRSAR DEPLOYMENT 1996

Over a seven-week period during the Fall of 1996, NASA flew AirSAR missions at more than 50 sites in 10 countries throughout the Pacific Rim. The teams of investigators were comprised of NASA scientists and scientists from host countries. In addition to topographic mapping, AirSAR data were used for crop and forest classification, soil moisture estimation, geologic mapping, wetland and mangrove forest monitoring, forest biomass and biodiversity estimation, coastal monitoring and floodplain morphology.

In addition to AirSAR, the scientific payload aboard the DC-8 aircraft included the Thermal Infrared Mapper (TIMS), Airborne Emission Spectrometer (AES) and Cloud Radar. Typically, TIMS and AES were used simultaneously to collect complimentary

data over the same site. TIMS was used primarily for imaging of SO_2 concentrations in volcanic gas plumes, while AES was used to provide temperature and humidity profiles.

CHAPTER 3: EVALUATION OF DEMS

A primary objective of this study is to test the AirSAR topographic data for use in hydrologic modeling studies. During the 1996 Pacific Rim mission, interferometric and polarimetric data were collected for both the 21 km^2 Paul Creek and 10.2 Ha Tarrawarra catchments, located near Melbourne in Victoria, Australia. The Tarrawarra location was chosen because it is the site of an intensive, on-going field investigation into the spatial and temporal variability of soil moisture (Western and Grayson, 1998). The adjacent and larger Paul Creek catchment was gauged by Melbourne Water during the late-1970's and early 1980's. Most of the analyses conducted in this study were for the Paul Creek catchment.

The AirSAR DEM was tested via comparison with other available topographic products. Although no reference elevation data are known to exist within the Paul Creek catchment, high quality topographic data exist for the Tarrawarra experimental catchment (4 km south of the Paul Creek stream gauge; Western and Grayson, 1998). Tarrawarra is a gently undulating pasture land used for grazing dairy cows. Even though the Tarrawarra catchment is small and lacks the topographic variability necessary to test these elevation products fully, it provides an opportunity for preliminary evaluation into the viability of the AirSAR DEM for hydrologic studies. An Australian Surveying and Land Information Group (AUSLIG) 3 arc second DEM was also available for the Tarrawarra site. The spatially averaged and spatially varying elevation differences (relative to the reference DEM) have been examined for AirSAR and AUSLIG DEMs.

3.1 DESCRIPTION OF DATA PRODUCTS

Three DEMs were compared for the Tarrawarra catchment: a 5 m reference product, a 10 m product derived from AirSAR – TOPSAR C-band interferometry, and the AUSLIG 3

arc second DEM. The AirSAR and AUSLIG data cover both the Tarrawarra and Paul Creek catchments. The relative accuracy of these DEMs at Tarrawarra can be used to infer the reliability of the AirSAR DEM for the larger Paul Creek catchment.

3.1.1 HIGH RESOLUTION DEM

The Tarrawarra high resolution topographic data set (Western and Grayson, 1998) was developed through field surveying of spot elevations on a 10 m grid throughout the catchment and interpolating to 5 m using the thin plate spline technique of Hutchinson and Gessler (1994). The elevation measurements have a vertical accuracy of 0.01 m and a positional accuracy of 0.1 m. The data are registered to the Univeral Transverse Mercator (UTM, Zone 55) coordinate system using the Australian Geodetic Datum 1966. The DEM was subsequently reprojected to the WGS84 datum for the sake of data consistency. The reprojection was performed using an algorithm within Arc/Info (Environmental Systems Research Institute, Redlands, CA).

3.1.2 AIRSAR DEM

The C-band AirSAR DEM was produced by Eric Fielding at JPL at a 10 m pixel size. As mentioned in Chapter 1, the resolution of an image is the distance at which separate features can be distinguished and is not necessarily the same as pixel size. For AirSAR, resolution varies depending on aircraft motion and experimental design, but for C-band images the horizontal resolution is generally between 9 and 13 m. Vertical errors in AirSAR data arise from a combination of systematic and random sources. Systematic errors can result from errors in ground truthing and instrumentation as described in Section 2.5.3. and generate an offset bias for the entire image. Random or spatially varying errors can result from minor positional errors, changes in the properties of the scattering surface (orientation, roughness, vegetation, etc.), as well as signal and processing noise. Spatially varying errors are not constant throughout the image. Previous implementations of TOPSAR show the data can have a systematic bias up to 40 m and

spatially-varying errors of only a few meters (Zebker et al., 1992). JPL staff have indicated that an improvement in the motion compensation system should reduce vertical errors to 2 - 5 m for the AirSAR DEMs produced from data collected during the 1996 Pacific Rim Mission. A substantial effort was made at JPL to reduce the vertical offset of the AirSAR DEM in response to the large offset observed in the SIR-C DEM for Mahantango, PA (Kenward and Lettenmaier, 1997). Positional errors are largely a function of the degree of georeferencing performed during processing, but can also result in scanning errors by the SAR (Zebker et al., 1992). The scanning errors should be small, especially in areas of low to moderate relief. A more complete discussion of DEM production from interferometric SAR data is presented in Section 2.5. The data produced by JPL were referenced to the UTM coordinate system (zone 55) and the WGS84 datum with some preliminary registration to mapped landmarks.

3.1.3 AUSLIG DEM

The source data for this grid is the spot elevation data held in the AUSLIG TOPO-250K RELIEF Theme: a network of surveyed spot elevations that exists for most populated areas of Australia (http://www.auslig.gov.au). The TOPO-250K data were used by AUSLIG to create the NATMAP series of 1:100,000 topographic maps – analogous to the USGS 7.5 degree quadrangles available in the USA. To create the DEM, spot elevation data and NATMAP contours were interpolated and gridded by AUSLIG to a pixel size of 3 arc seconds (~90 m N-S) and referenced to the Australian Geodetic Datum 1966. The resulting DEM has an absolute vertical error no greater than the 20 m gradations in the NATMAP contour maps. As stated by AUSLIG, the vertical error is generally closer to 5 m for each pixel. The positional error is not more than 25 m. The data were reprojected into UTM coordinates (zone 55) with a 90 m pixel size, using Arc/Info algorithms.

3.2 GEOREFERENCING AIRSAR DATA

Unlike most digital elevation products, such as USGS DEMs, the AirSAR DEM raster was not oriented in a regular, North-South grid. This is because the flight line of the DC-8 aircraft and thus the SAR instrument itself, was not oriented North-South during data collection. JPL reported approximate corner locations for the DEM and polarimetric maps based on in-flight GPS readings, but advised that referencing of features in the data sets to known landmarks would improve the positional accuracy of the AirSAR images. After receiving the AirSAR data from JPL, the following method was used to georeference the resulting images:

- Images were rotated to match the reported flight line of the aircraft
- The locations of features observed in the polarimetric images, such as road crossings, stream bends and railroad tracks were linked to corresponding locations in a NATMAP 1:100,000 topographic map.
- Images were registered to map coordinates using algorithms in Arc/Info.
- Accuracy of registration was verified using 2 separate corner reflectors, the locations of which were provided by Andrew Western of Melbourne University.

In order for the image rows and columns to be aligned with North-South and East-West, respectively, the DEM and polarimetry images were rotated about the lower-left corner by approximately 21.95 degrees counter clockwise to match the reported flight line of the aircraft. The AirSAR DEM pixels were square when the map was oriented along the flight path, but when the DEM was rotated, in order to retain square pixels and have rows of the grid aligned North-South, automatic resampling occurred. To test the effect of the resampling, the rotation was performed with two different methods. First, the output cell size was not explicitly specified and the resulting grid cells were 13.048 m on a side. A decrease in map area of slightly less than 0.04% occurred during the resampling. Next,

the grid was rotated and an output cell size of 10 m was retained via a bilinear resampling algorithm. The map area decreased by slightly less than 0.03%. The 10 m DEM was used in subsequent analyses in order to retain the original data resolution. The rotation resulted in a DEM that was registered approximately to surface feature coordinates to within approximately 150 m.

Coordinate registration was improved by including a set of surface features observed in AirSAR polarimetric images, such as road crossings and stream junctions to coordinates of those features extracted from a NATMAP 1:100,000 topographic map of the area. The AirSAR images were first reprojected from the WGS84 datum to the Australian Geodetic Datum 1966 to be consistent with the NATMAP topographic map other spatial data sets. The coordinates of the landmarks were in general most easily identified in cross-polarized (HV) L-band and P-band images: rivers, roads and train tracks show up as dark regions in these images. With a magnifying glass, the coordinates of the same features were read from a hard copy NATMAP 1:100,000 map to the nearest 50 m. AUSLIG documentation states the positional accuracy of the NATMAP maps are ~25 m. Superimposing these two sources of positional uncertainty, it was assumed that each feature could be read to within 75 m. A series of co-registration coordinates were created for the Paul Creek and the Tarrawarra scenes and the Arc/Info GRIDWARP algorithm was used to refine the fitting of each image to surface features (Table 3.1, Figure 3.1).

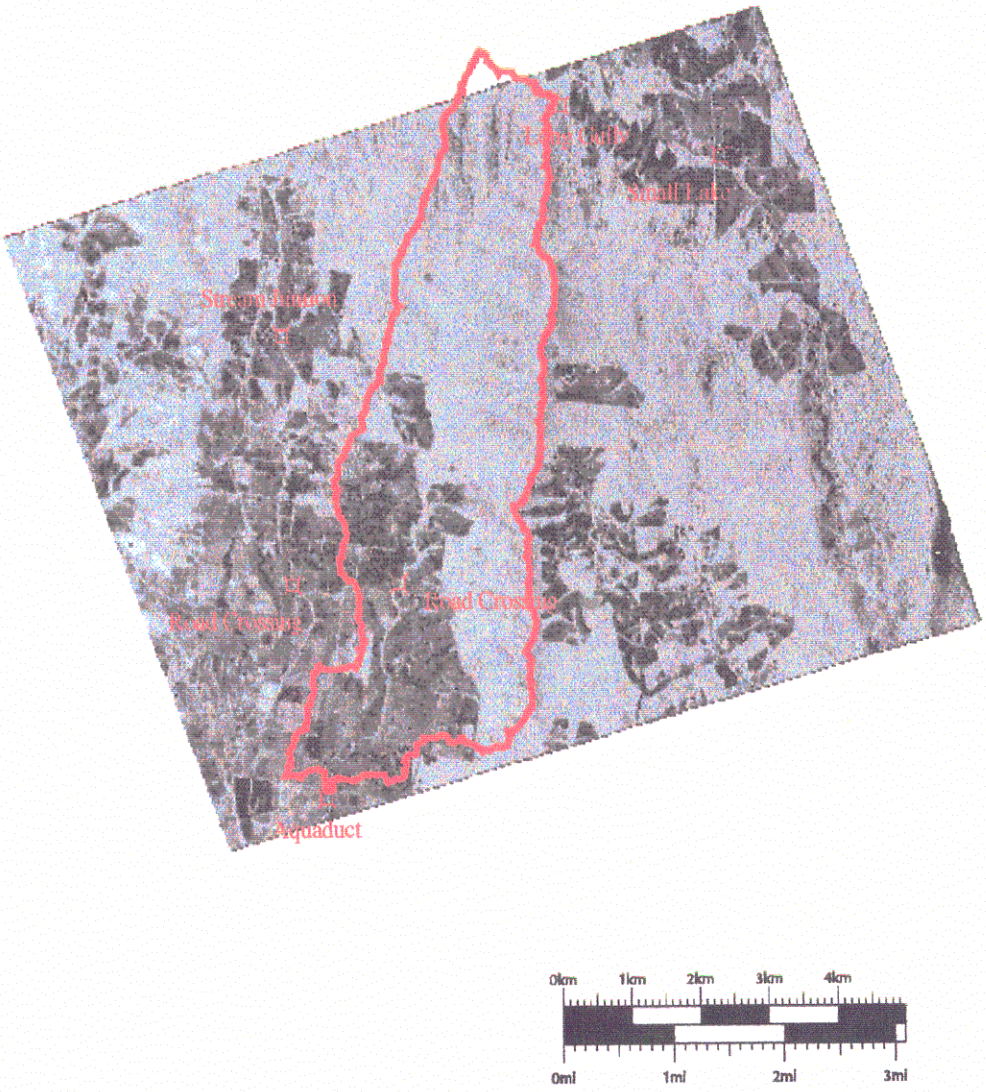

Figure 3.1a L-band HV image of Paul Creek scene with locations of features used to georeference image.

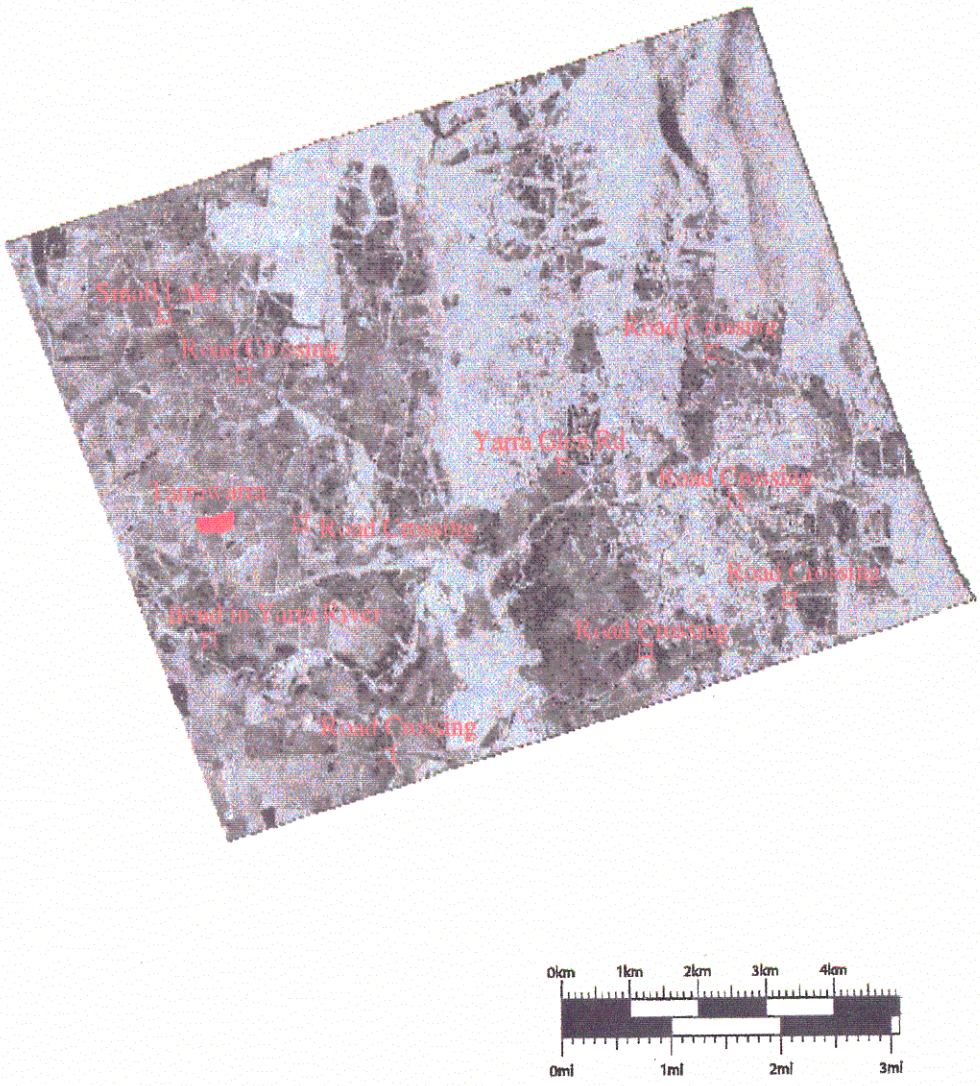

Figure 3.1b L-band HV image of Tarrawarra scene with locations of features used to georeference image.

Table 3.1 Locations of observed surface features used for coordinate registration.

	Column Number	Row Number	NATMAP Easting	NATMAP Northing*	Description
Paul Creek					
	89	207	360960	5834520	Maroondah Aquaduct
	34	793	360340	5840680	Junction on Upper Dixons Creek
	676	1030	366750	5843020	Small Lake, NW corner
	440	424	364420	5843680	Long Gully headwaters
	201	466	362030	5837430	Road crossing on Paul Creek
	48	467	360480	5837410	Road crossing on Dixons Creek
Tarrawarra					
	334	404	362170	5829540	Bend of Yarra River
	591	253	364740	5828030	Stream crossing Maroondah Hwy
	467	557	363500	5831070	Road crossing near Abbey
	852	628	367350	5831780	Yarra Glen Rd and Healesville Rd
	970	385	368530	5829350	Road crossing on Maroondah Hwy
	1183	451	370660	5830010	Road crossing near Healesville
	1104	580	369870	5831300	Road crossing near Healesville
	1072	775	369550	5833250	Road crossing N of Healesville
	387	750	362700	5833000	Road crossing E of Paul Creek
	273	829	361560	5833790	Inlet from Lake to Paul Creek

* As is customary for Southern Hemisphere locations described in UTM coordinates, an offset of 10,000,000 m has been applied so that all Northing coordinates are positive.

To test the accuracy of the image registration, the GPS verified locations of a set of corner reflectors were compared with their observed locations in the L-band VV image. The corner reflectors were not used in the georeferencing procedure, so the comparison of their locations provides an independent verification of registration accuracy. The reflector locations were reported by Andrew Western of Melbourne University (*personal communication*) and are accurate to within 10 m. Corner reflectors backscatter a high fraction of the incident wave and are thus seen as bright spots on the processed polarimetric image. There were four corner reflectors in place during the AirSAR data collection flight, but only two were positively identified in the polarimetric images. One reflector was not visible in the images and the other was surrounded by other sources of high backscatter. Table 3.2 shows the image and GPS locations for two corner reflectors. The data are expressed in UTM coordinates (zone 55) and registered to the Australian

Geodetic Datum 1966. The spatial separation between the image and GPS coordinates was ~20 m for both corner reflectors. This confirms that the additional georeferencing performed on the AirSAR images resulted in accurate image registration.

Table 3.2 Location of corner reflectors.

	Image Easting	Image Northing	GPS Easting	GPS Northing
Reflector 2	365765	5827811	365768	5827831
Reflector 4	364775	5834384	364783	5834399

3.3 DEM COMPARISONS

The results of the comparisons of the AirSAR and AUSLIG DEMs with the reference DEM are summarized in Table 3.3 and Figure 3.2. There was an 3.2 m vertical offset in the AirSAR data relative to the reference DEM. If the offset is removed, the (1 σ) vertical error of the AirSAR DEM is ~ 1.3 m. The high frequency, elevation noise evident in the SIR-C DEM of Mahantango Creek, PA (Kenward, et al., 1997) is not apparent in the AirSAR data at Tarrawarra. Figure 3.2a shows that the character of the hill slope gradients and ridge lines of Tarrawarra are clearly captured by the AirSAR DEM. Based on the limited analysis at Tarrawarra, the AirSAR DEM should provide a high quality topographic data set for hydrological studies of the Paul Creek catchment.

Each AUSLIG pixel contains 324 times the area of the reference DEM pixels. This results in significant averaging: in comparison with the reference DEM, the AUSLIG elevations are lower near the upper boundary of the basin and higher near the outlet. The drainage pattern is also different for the AUSLIG DEM with flow lines leading to the outlet at the southwest corner rather than the south-central part of the catchment. Despite the spatial differences in elevation, on average the AUSLIG DEM is offset from the Tarrawarra DEM by only 1.6 m. However the standard deviation of the elevation differences is 4.9 m suggesting the observed errors in the AUSLIG DEM at Tarrawarra

are a function of data resolution rather than a vertical bias in the AUSLIG data set. It is apparent from the figure that the AUSLIG elevations vary more slowly than the reference data would if aggregated to 90 m. This suggests the true spatial resolution of the AUSLIG DEM is coarser than the 90 m pixel size. Also, Figure 3.2 shows that 90 m cell size of the AUSLIG DEM is probably too coarse to resolve flow paths properly in areas of low relief.

Table 3.3 Comparison of spot elevations with AirSAR and AUSLIG DEMs.

Easting	Northing	Reference (m)	AirSAR (m)	AUSLIG (m)
362060	5830960	89	84	88
362060	5831040	89	86	89
362060	5831120	96	93	90
362140	5830960	82	79	89
362140	5831040	88	86	90
362140	5831120	97	97	91
362220	5830960	82	78	90
362220	5831040	89	86	91
362220	5831120	99	97	93
362300	5830960	89	85	91
362300	5831040	87	84	92
362300	5831120	97	95	94
362380	5830960	95	92	91
362380	5831040	91	87	93
362380	5831120	95	92	95
362460	5831040	98	93	94
362460	5831120	97	93	95
362460	5831200	105	103	98
362520	5831040	101	95	94
362520	5831120	101	98	95
362520	5831200	107	103	98
Average Difference (m)		**N/A**	**-3.2**	**-1.6**
Std Dev of Difference (m)		**N/A**	**1.3**	**4.9**

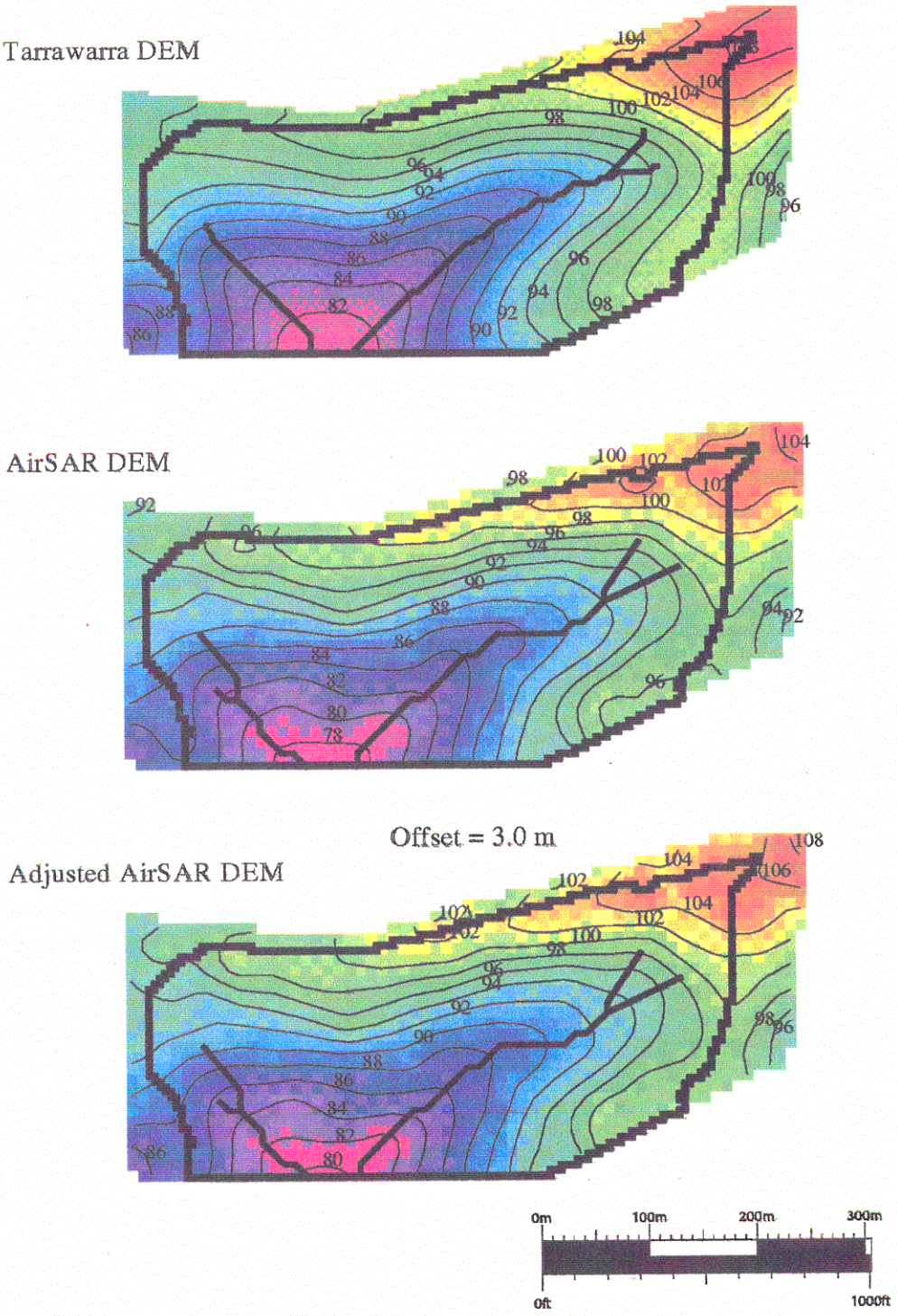

Figure 3.2a Comparison of 10 m AirSAR and 5 m reference Tarrawarra DEMs. A 3 m offset is visible in the AirSAR data. In the third plot, the AirSAR DEM has been raised 3 m to match the reference DEM.

Tarrawarra DEM

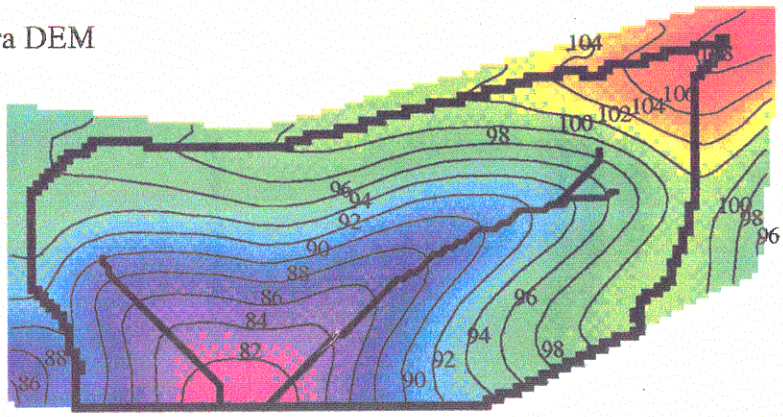

AUSLIG DEM

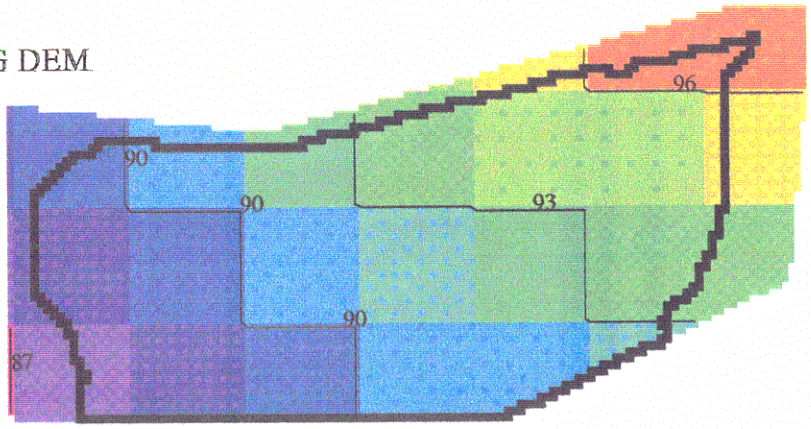

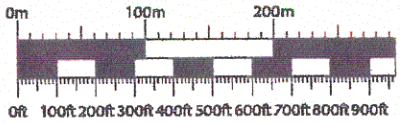

Figure 3.2b Comparison of 90 m AUSLIG and 5 m reference DEMs. Some of the orographic characteristics of the catchment are captured by the AUSLIG DEM. However, the drainage is to the SW rather than S.

CHAPTER 4: COMPARISON OF DEM-DERIVED GEOMORPHIC PARAMETERS

A number of studies have investigated the relationship between DEM spatial resolution and the ability to represent hydrologically important variables, such as the distribution of slopes within a catchment (e.g. Wolock and Price, 1994). Other studies have tested a range of DEM resolutions with hydrology models, such as TOPMODEL (Zhang and Montgomery, 1994). In general, the geomorphic characteristics examined in previous studies have been limited to the distributions of elevation, slope and contributing area.

In this chapter, DEM-derived hydrologic variables which directly affect the predictions of a spatially distributed, physically based hydrology model are examined. The examination of geomorphic characteristics is undertaken first to provide an explanation in terms of physical mechanisms for the differences (and similarities) observed from model simulations at different horizontal resolutions. In addition to general basin characteristics like drainage area and mean elevation, DEM representation of slopes, sub-surface and in-channel path lengths are calculated at a variety of resolutions using two different mathematical approaches to data aggregation.

4.1 AGGREGATING SPATIAL DATA

As spatial data are aggregated to progressively coarser resolutions, higher frequency features apparent on the land surface may not be retained and accurately represented. Peaks and ridges tend to be smoothed, narrow valleys tend to be filled and widened, and sharp hill slope breaks tend to become blurred. Under wet conditions, the rate and directional movement of moisture through a catchment is largely driven by elevation gradients, so a DEM that captures the dominant characteristics of the terrain is highly desirable. In spatially distributed modeling studies, computation time is inversely proportional to the square of the pixel size (length), making larger grid cells desirable. A

fundamental question in the application of such models concerns the appropriate scale for modeling studies. The tendency has been to apply models at the finest resolution made possible by the available spatial data sets and computing power. While it is clear that finer modeling scales can represent more of the high frequency features that contribute to hydrologic response, the relationship between spatial resolution and the behavior of spatially distributed, physically based hydrology models has not been investigated.

Before investigating the effect of pixel size on model predictions, it is necessary to investigate how the chosen method of data aggregation affects the resulting data and if a specific method is particularly well-suited to preserving topographic gradients important for hydrologic modeling studies. Two techniques have been examined in this chapter: a standard bilinear resampling algorithm and an innovative modified fractal scheme.

4.1.1 BILINEAR INTERPOLATION

A bilinear interpolation scheme was chosen because it is widely used and simple to apply. The value of the resampled target cell is calculated using the weighted average of the values of the 4 nearest cells. Figure 4.1 shows a sample elevation grid along with the general expression for the interpolated elevation at a particular pixel (without assuming pixels are square):

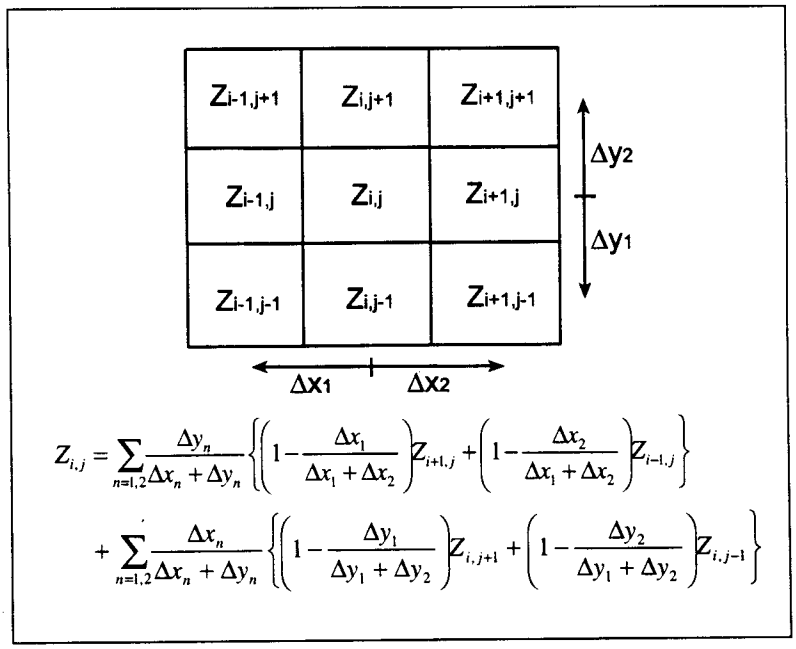

$$Z_{i,j} = \sum_{n=1,2} \frac{\Delta y_n}{\Delta x_n + \Delta y_n} \left\{ \left(1 - \frac{\Delta x_1}{\Delta x_1 + \Delta x_2} \right) Z_{i+1,j} + \left(1 - \frac{\Delta x_2}{\Delta x_1 + \Delta x_2} \right) Z_{i-1,j} \right\}$$
$$+ \sum_{n=1,2} \frac{\Delta x_n}{\Delta x_n + \Delta y_n} \left\{ \left(1 - \frac{\Delta y_1}{\Delta y_1 + \Delta y_2} \right) Z_{i,j+1} + \left(1 - \frac{\Delta y_2}{\Delta y_1 + \Delta y_2} \right) Z_{i,j-1} \right\}$$

Figure 4.1 DEM schematic and bilinear interpolation algorithm.

In the case of a square pixels, the weighting terms drop out of the equation, leaving the calculated value as the average of the grid cells to the left, right, above and below. Interpolation continues across the DEM until the aggregated map meets the following conditions:

$$ncols = \frac{(x_{max} - x_{min})}{\Delta x} \quad \text{and} \quad nrows = \frac{(y_{max} - y_{min})}{\Delta x}$$

If the cell size is not an integral factor of the different between maximum and minimum coordinates, the maximum coordinates are adjusted accordingly. Bilinear interpolation preserves surface volume well, but some smoothing occurs.

4.1.2 MODIFIED FRACTAL INTERPOLATION

The modified fractal interpolation scheme attempts to capture the pattern of underlying irregularity in a topographic surface. The pattern is then applied to representations of the data at coarser resolutions. This is accomplished by calculating the fractal dimension and roughness factor of the original DEM and using these values in a weighting function which is applied in the data aggregation process. This results in a more accurate preservation of higher frequency terrain features that can be important for hydrological studies in areas of high relief. Details of the methods are provided by Bindlish and Barros (1996) and Kenward and Lettenmaier (1997), including an example application of modified fractal interpolation to a hydrological study of the Mahantango Creek watershed, PA.

4.2 GEOMORPHOLOGICAL PARAMETERS

A number of topographically determined basin characteristics influence catchment response to precipitation. In this section, the statistical distribution and magnitude of slopes, subsurface and in-channel flow lengths are evaluated as a function of DEM resolution. The widely used topographic index (Beven and Kirkby, 1979) is also be examined.

4.2.1 AGGREGATION PROCEDURE

A set of DEMs at 20, 30, 50, 90 and 200 m was created using bilinear and the modified-fractal aggregation methods (a total of 10 new DEMs were produced). All aggregated DEMs were created from the same source DEM (AirSAR), i.e. the 30 m DEM was created from a 10 m and not from a 20 m DEM. After aggregation, the boundary of the Paul Creek catchment was delineated for each DEM[3]. A pour point as close as possible to

[3] An unmasked AirSAR DEM was used during the aggregation process in an effort to reduce resampling error near the boundary of the Paul Creek catchment.

the 10 m AirSAR DEM outlet was chosen for the delineation. Two streams intersect in the low-relief region just above the stream gauge. In some cases, the outlet had to be moved southward in order for these streams to intersect. This resulted in an artificial increase in catchment area, particularly for the bilinear 50 m DEM and the fractal 90 m DEM (see Figure 4.2). The streams did not converge for the 50 m fractal interpolation DEM, which reduced the overall catchment area.

4.2.2 Basin Characteristics

The mean, maximum and minimum elevations, and basin area at each resolution for each aggregation scheme are shown in Table 4.1. The DEMs produced using the bilinear aggregation method have mean and maximum elevations closer to the 10 m AirSAR DEM than those produced using the modified-fractal method. Any smoothing that resulted from spatial aggregation did not systematically reduce the standard deviation of the distribution of elevations. The AUSLIG DEM has substantially lower values of mean and maximum elevations, standard deviation and catchment area compared with the bilinear and fractal 90 m DEMs. These could all occur if the catchment boundary delineated from the AUSLIG DEM included significantly less of the high elevation area in the northern portion of the basin. The lower standard deviation of the AUSLIG DEM is also a sign of a smoothed, lower resolution DEM.

Figures 4.2a and 4.2b show spatial images of the DEMs created with each of the two aggregation methods along with the basin outline for the 10 m AirSAR DEM, and Figure 4.3 compares the bilinear and modified-fractal DEMs at 90 m with the AUSLIG DEM. For each of the DEMs, the catchment area remains similar after aggregation in part because area is both added and lost to the catchment relative to the AirSAR basin mask. Table 4.2 summarizes the changes in catchment boundaries in terms of area gained outside the AirSAR mask and area lost inside the AirSAR mask. From the lower values of *area lost* and *area gained*, it is clear the boundaries of the bilinearly interpolated

DEMs vary less relative to the 10 m AirSAR DEM than do those of the modified-fractal DEMs.

Table 4.1 Topographic characteristics of Paul Creek at different horizontal resolutions.

DEM	Area (km^2)	Mean Z (m)	Max Z (m)	Outlet Z (m)	Std Dev	Resolution*
AirSAR (10 m)	21.45	242.2	507	97	101.3	10
Bilinear 20 m	21.37	242.4	505	97	101.1	20
Bilinear 30 m	21.48	243.5	506	97	101.9	30
Bilinear 50 m	21.80	240.3	506	95	102.0	50
Bilinear 90 m	21.50	242.9	501	99	101.7	90
Bilinear 200 m	21.56	238.4	499	96	101.0	200
Fractal 20 m	21.60	239.9	497	97	100.7	20
Fractal 30 m	21.56	240.4	497	97	100.7	30.1
Fractal 50 m	21.19	246.0	500	103	99.6	50.2
Fractal 90 m	21.87	241.2	504	97	102.1	91.4
Fractal 200 m	20.66	251.6	484	100	100.3	213.3
AUSLIG 90 m	20.43	231.3	477	100	87.3	90

*Fractal interpolation algorithm requires integral reduction in numbers of rows and columns. Resulting pixel size was not necessarily an integer

Table 4.2 Changes in catchment area inside and outside of AirSAR DEM mask.

	Area Lost (km^2)	Area Gained (km^2)	Net Change (km^2)	% Diff from AirSAR
Bilinear 20 m	0.17	0.09	-0.08	-0.3
Bilinear 30 m	0.17	0.21	0.04	0.2
Bilinear 50 m	0.19	0.55	0.35	1.7
Bilinear 90 m	0.42	0.47	0.05	0.2
Bilinear 200 m	0.78	0.89	0.11	0.5
Fractal 20 m	0.34	0.49	0.16	0.7
Fractal 30 m	0.25	0.38	0.13	0.6
Fractal 50 m	0.93	0.69	-0.24	-1.1
Fractal 90 m	0.36	0.80	0.44	2.0
Fractal 200 m	2.30	1.51	-0.78	-3.7
AUSLIG 90 m	1.95	0.93	-1.02	-4.7

The change in catchment area and the change in the distribution of elevations are particularly important for hydrologic modeling. The change in catchment area has a near linear effect on model calculations of stream discharge because measured precipitation is distributed throughout the catchment so that an increase in surface area translates to an increase in precipitation volume. A lapse rate is used to vary the precipitation as a function of elevation throughout the catchment so that area gained near the top of the catchment is not quite offset by an equal area lost near the outlet to the catchment. The total effect of the differences in the distribution of elevations is reflected in the average elevation of the catchment. The average elevations of the bilinear DEMs are closer to the average elevation of the source DEM than the fractal DEMs (see Table 4.1). Considering the catchment area and average elevations, the bilinear DEMs should more accurately reproduce the distribution of precipitation derived from the AirSAR DEM than those aggregated using the modified-fractal method.

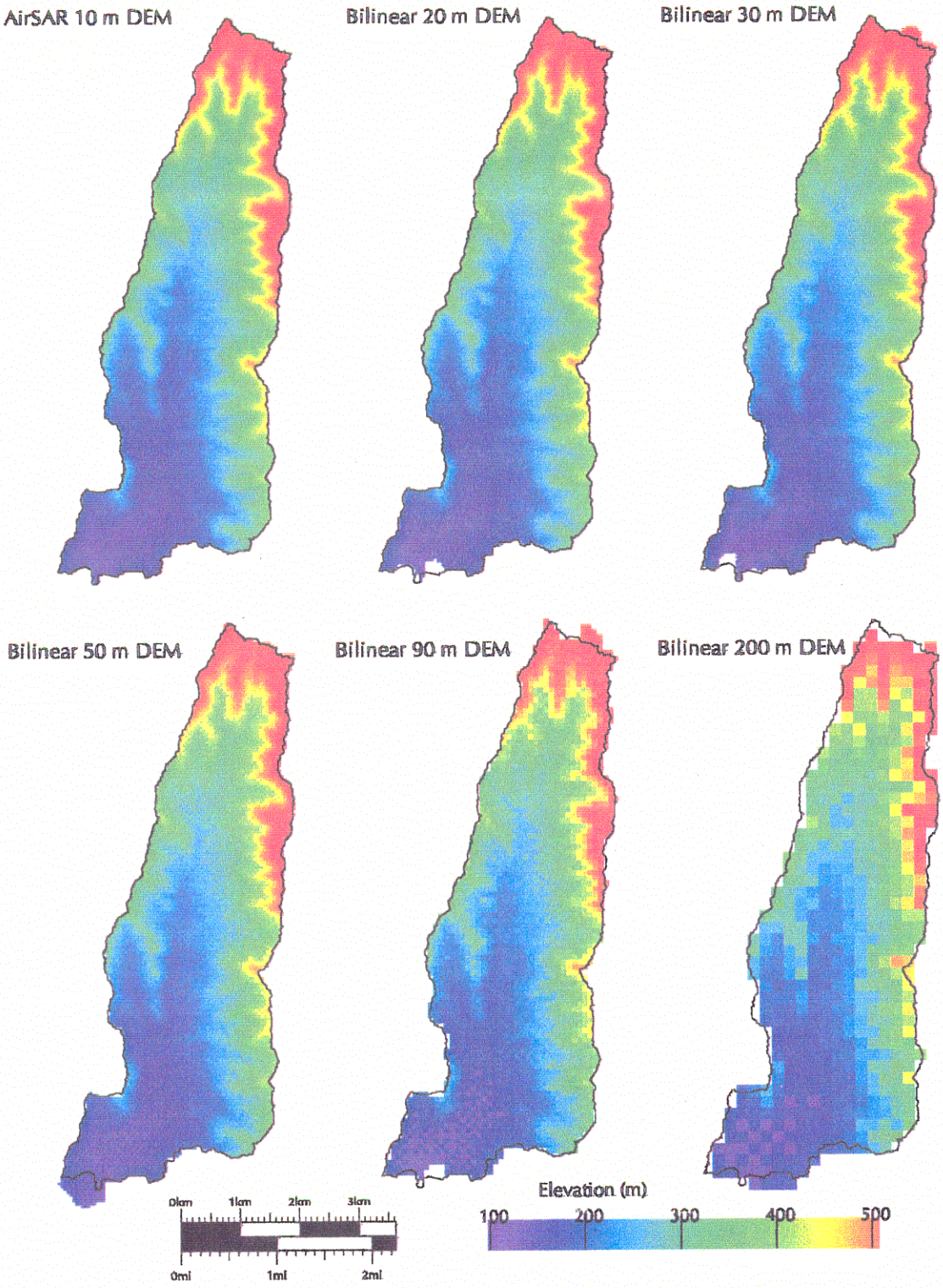

Figure 4.2a. DEMs aggregated using bilinear interpolation.

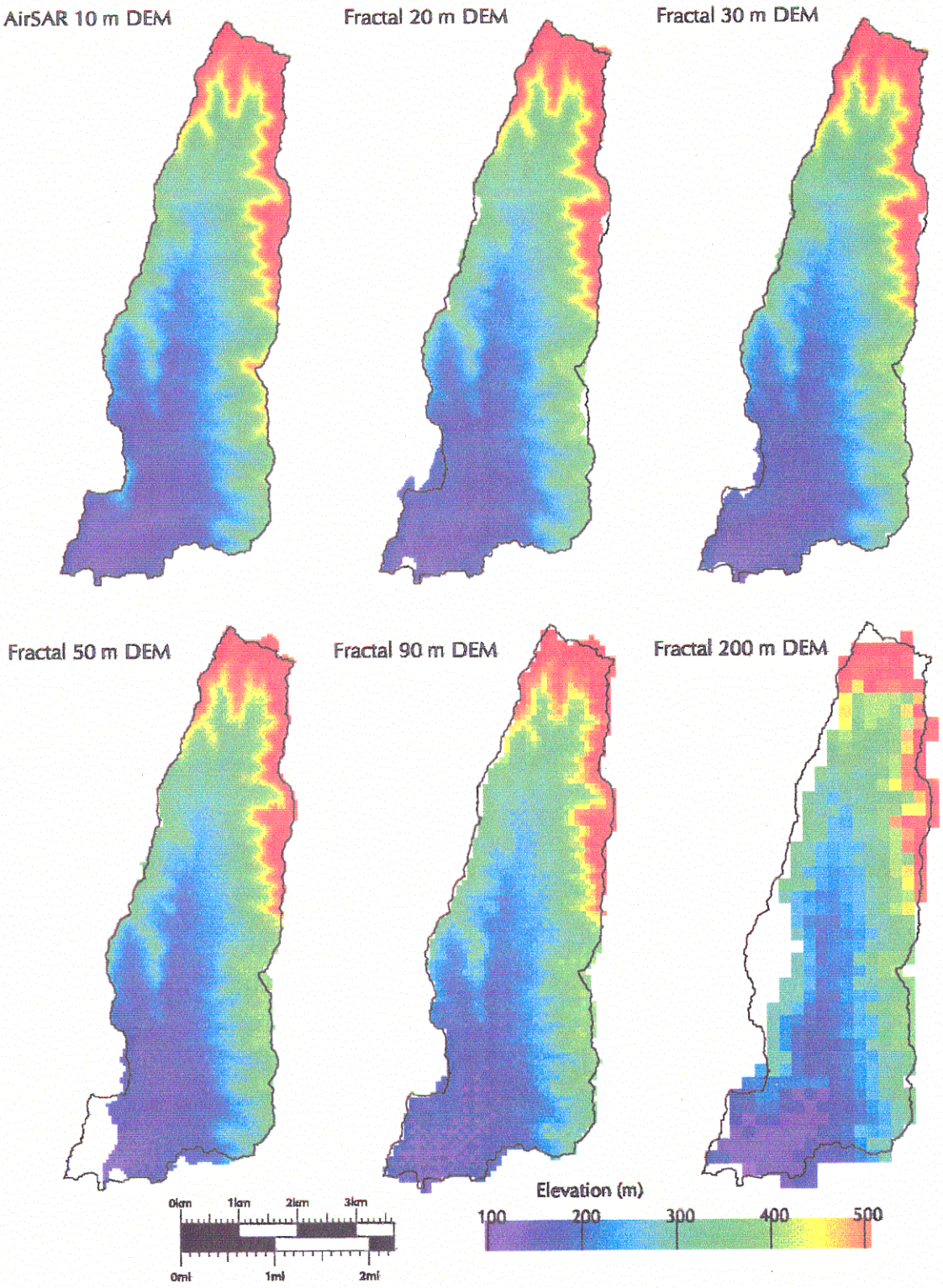

Figure 4.2b. DEMs aggregated using modified-fractal interpolation.

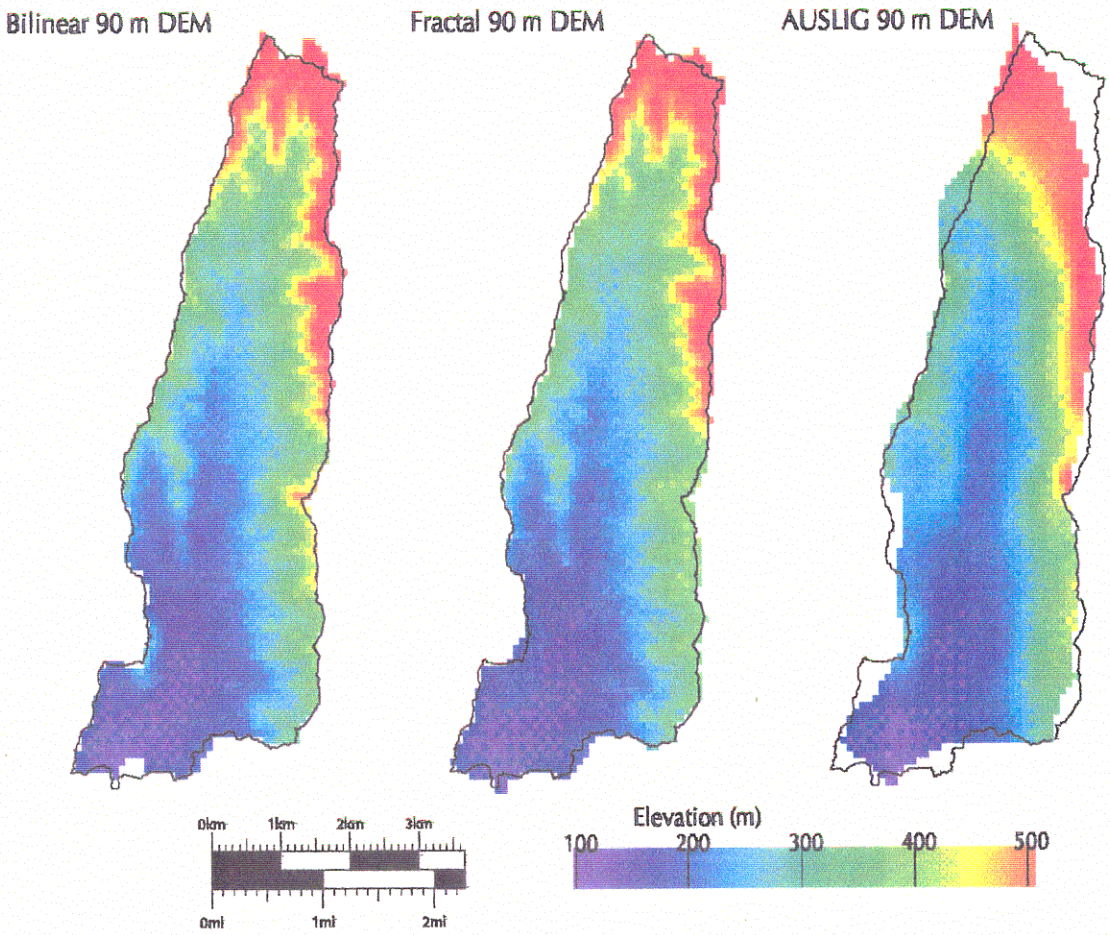

Figure 4.3. Comparison of the spatial structure of the 90 m DEMs.

BASIN SLOPE

In catchments where hydrologic response is driven largely by saturation excess, accurate representation of slopes is important for predicting the direction and rate of flow, and the areas of surface flow generation. Slope has been calculated based on the direction of steepest descent to any one of the eight surrounding pixels. In an attempt to highlight DEM representation of the transition from valley to hill slope, the cumulative distribution of slopes is plotted against fraction of catchment area for each DEM (Figures 4.4a and 4.4b). The distribution of fractal slopes diverges significantly from those of the AirSAR DEM for 20 m pixels and larger. The distribution of bilinear slopes diverge less from the AirSAR slopes than those derived from fractal DEMs (at the same resolution). Therefore, aggregating the AirSAR DEM to larger pixel sizes using bilinear interpolation results in less smoothing than a similar aggregation using the fractal interpolation. A smaller portion of the catchment has near-zero slopes for the bilinear DEMs than the fractal DEMs. This difference has substantial implications for soil moisture distributions calculations based on these DEMs. From this analysis, DEMs aggregated via bilinear interpolation preserve the topographic gradients of the AirSAR DEM more accurately than the modified-fractal scheme DEMs. The distribution of AUSLIG slopes plot nearest to the 200 m DEMs. Along with mean and maximum elevations, and standard deviation shown in Table 4.1, the cumulative distribution of AUSLIG slopes suggests that a greater fraction of topographic features are retained by the aggregated 90 m AirSAR DEMs than the 90 m AUSLIG DEM.

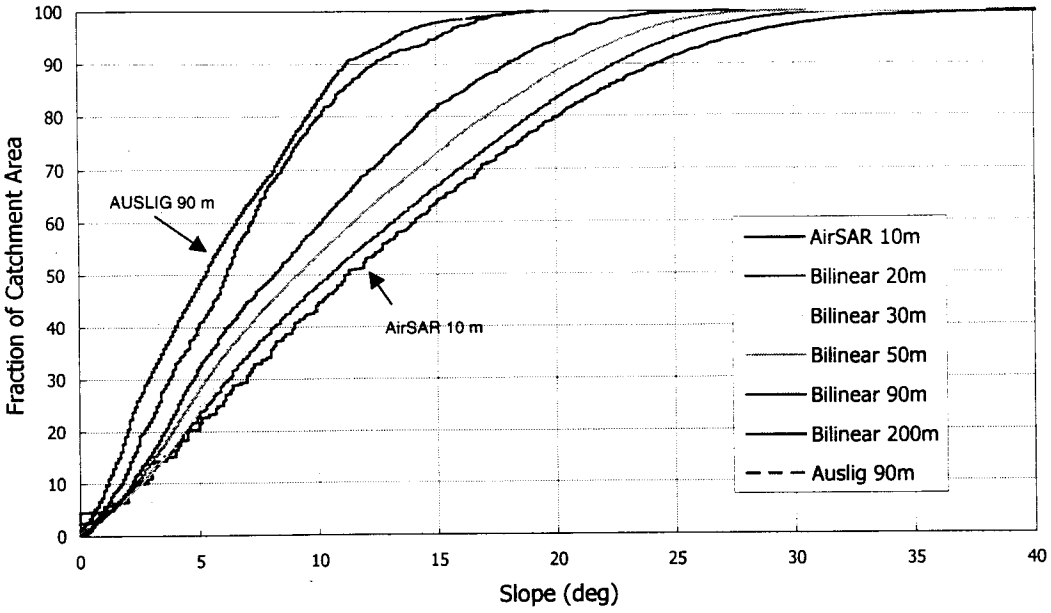

Figure 4.4a The distribution of slopes for DEMs created using the fractal interpolation scheme. The AirSAR DEM is also shown as a reference. The AUSLIG DEM slopes are also shown.

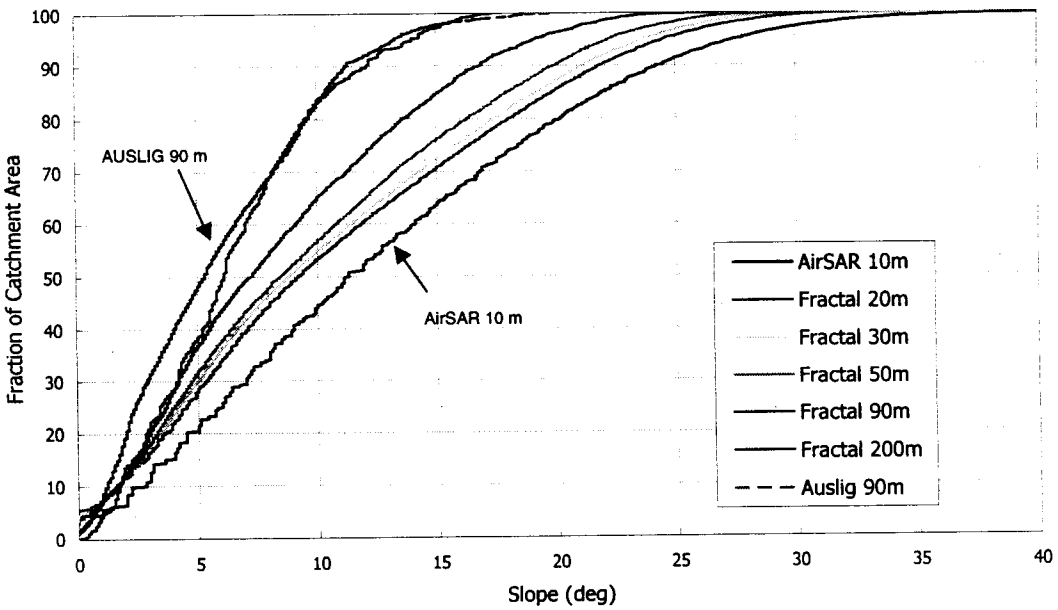

Figure 4.4b The distribution of slopes for DEMs created using bilinear interpolation.

The spatial distribution of slopes provides greater insight into the differences between the two aggregation methods applied to Paul Creek (Figure 4.5). At several locations near the boundary to the catchment, the slopes calculated from fractal DEMs drop to zero. Typically, extended areas with zero slope are an indication of a filled sink – often generated in areas with low-relief. Aggregated DEMs were created from an unmasked DEM. It is possible that in some locations, pixels on the far side of the ridges comprising the basin divide were used to calculate aggregated pixel values with the modified-fractal interpolation scheme. This would account for some of the dramatic smoothing evident on narrow ridge tops. Regardless of the reason for the artificial plateaus along the catchment boundary, their presence will increase the tendency for water to pond in these areas of the catchment, introducing a systematic discrepancy between modeled and *actual* conditions. Again, the bilinearly interpolated DEMs appear to preserve more accurately the topography of the AirSAR 10 m DEM.

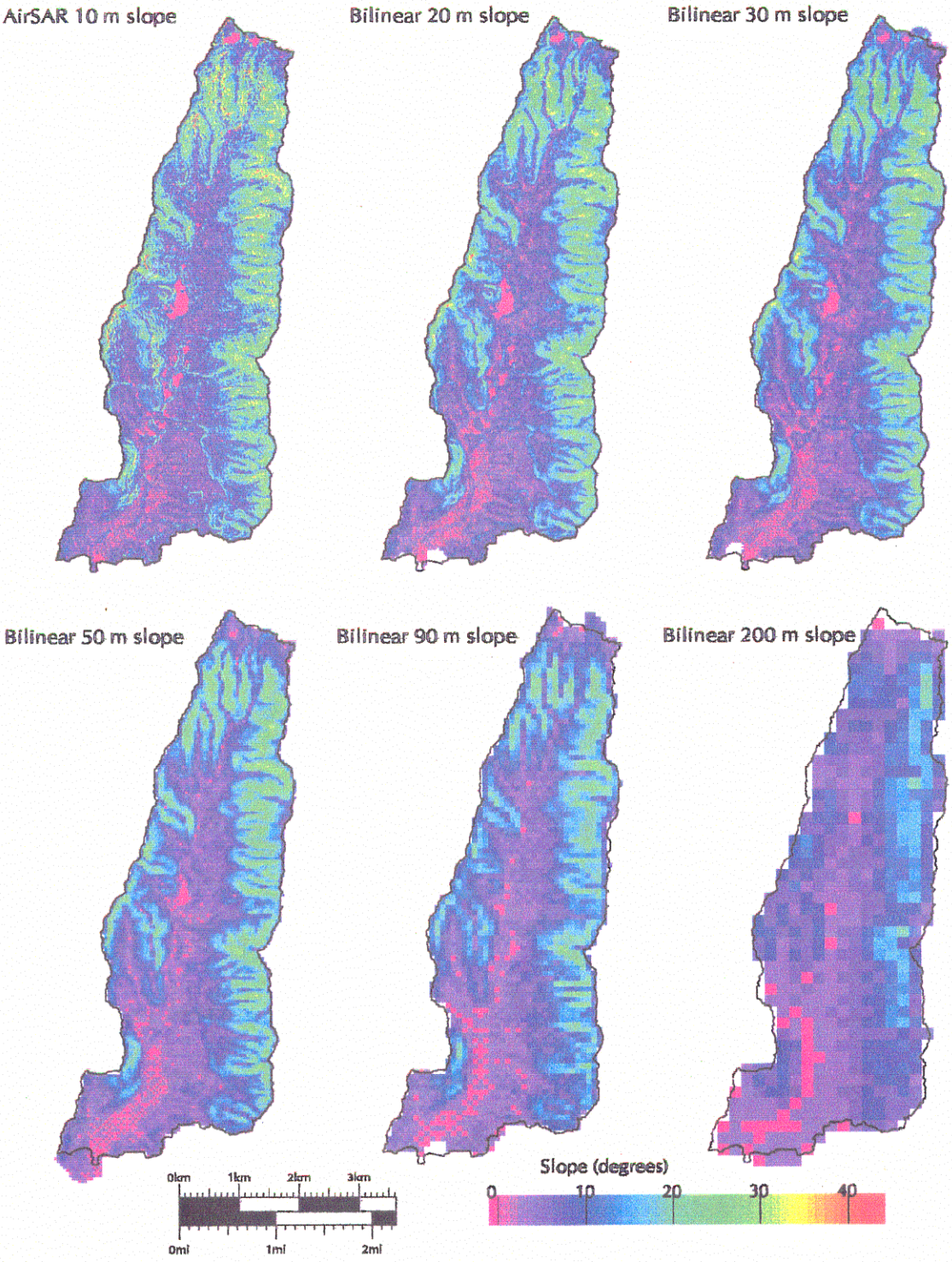

Figure 4.5a. Slopes calculated from bilinear DEMs.

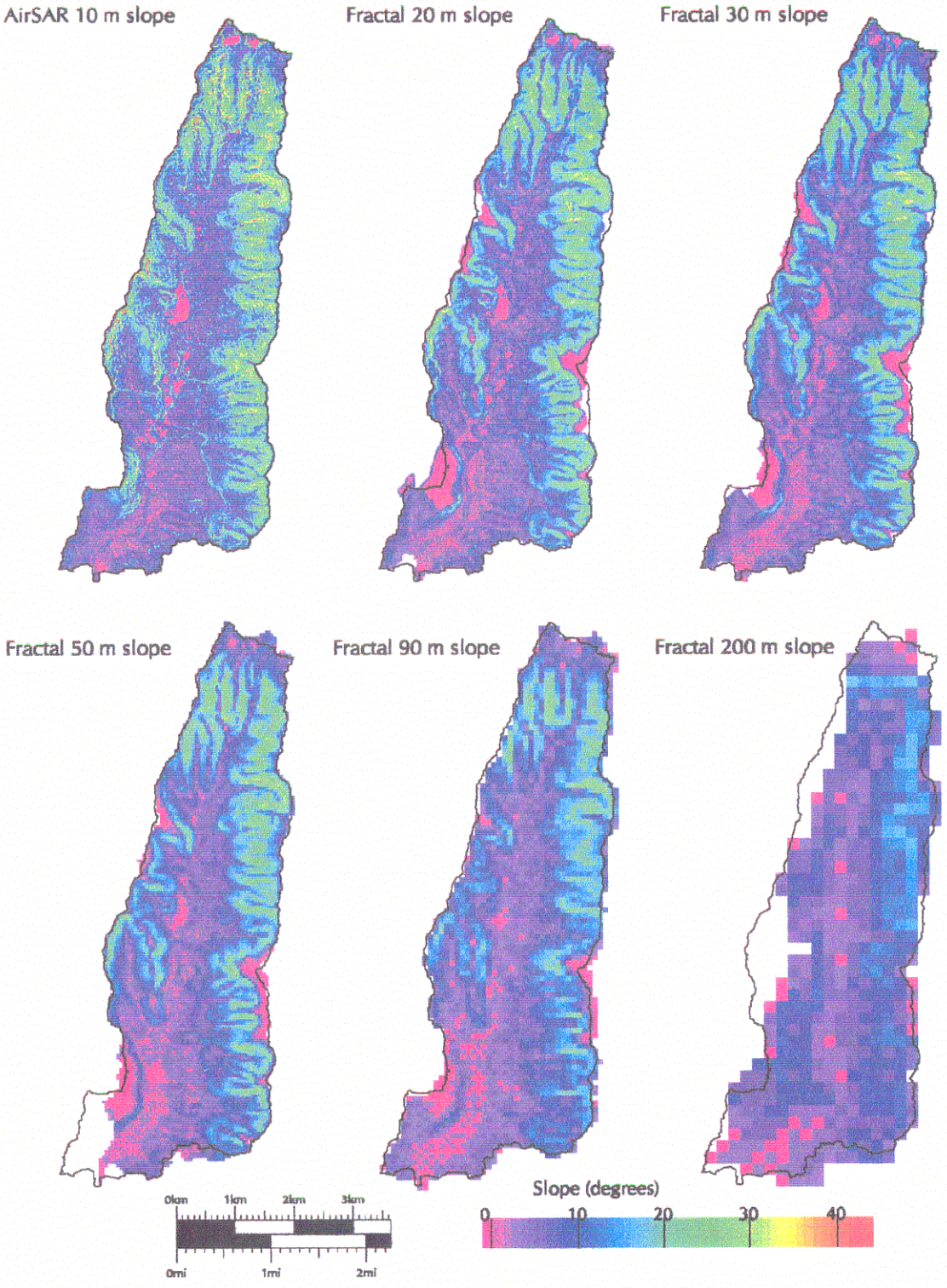

Figure 4.5b. Slopes calculated from modified-fractal DEMs.

4.2.3 IN-CHANNEL FLOW LENGTH

Stream channel networks, network topology, stream segment characteristics and sub-watershed boundaries are derived more efficiently by applying automated techniques to DEMs than using traditional methods with contour maps (Garbrecht and Martz, 1994). A number of algorithms have been developed for calculating the contributing area draining to each pixel (Tarbarton et al., 1991; Gyesi-Agasi et al., 1995; Costa-Cabral and Burges, 1994), but without the benefit of field verification (i.e. mapping the surface stream network) there was no opportunity to evaluate the appropriateness of each method for the Paul Creek catchment independently.

For the Paul Creek watershed, the lateral direction of flow for each pixel was calculated using an 8-direction method of steepest descent: water is assumed to flow towards the neighboring cell for which the elevation gradient is largest. The area contributing to each pixel in the catchment was calculated from the flow direction map. Pixels with contributing areas greater than the threshold value of 5 Ha were used to generate a preliminary stream network. Stream segments with contributing areas barely above the threshold located in low relief regions of the catchment were removed. This follows the variable contributing area concept described by Montgomery and Foufoula-Georgiou (1993). Rather than applying Montgomery's mathematical criteria directly, judgment was used to determine which segments should be removed. Stream network similarity was preserved as much as possible from DEM to DEM, i.e. the same stream segments were removed from the preliminary stream network at each resolution. It should be stressed once again that the purpose of this study is to assess the differences in predicted hydrological behavior as a function of spatial resolution. Therefore consistency in the method used to derive stream networks at each resolution is more important than exact replication of the actual stream network of Paul Creek (provided a reasonable representation is obtained).

Flood hydrograph timing in DHSVM is directly related to the distance traveled by incident precipitation to the catchment outlet. Differences in the derived stream networks were evaluated in the following manner. A visual inspection of the each stream network shows the loss of detail the results from DEM aggregation (Figure 4.6). The complexity of surface flow paths should be analogous to that of subsurface flow paths, since the surface flow paths are simply defined in terms of an assigned threshold contributing area. It was postulated that lower resolution DEMs should yield straighter stream networks with a lower average distance from tributary headwaters to the outlet, because of a reduction in the number of meanders apparent at higher resolutions. This was quantified by calculating the distance from the headwaters to the outlet for a sampling of the major tributaries at each resolution (Figure 4.7; Table 4.3). Because it was shown in the previous two sections that the bilinear interpolation scheme yielded more hydrologically realistic DEMs, only stream networks created from bilinearly resampled DEMs were examined in this section. Table 4.3 and Figure 4.7 show increased pixel size does not necessarily result in shorter flow paths. A marked decrease in flow length from headwaters to outlet is evident from the 200 m DEM, but not from the others.

Table 4.3 In-stream distance (km) from headwater to outlet for a sampling of tributaries.

Tributary	10 m DEM	20 m DEM	30 m DEM	50 m DEM	90 m DEM	200 m DEM
1	4.0	4.0	4.1	4.2	3.8	3.4
2	5.7	5.6	5.8	5.9	5.2	5.0
3	6.6	6.4	6.6	6.9	6.5	5.9
4	7.6	7.4	7.7	7.8	7.4	6.7
5	8.8	8.6	8.8	9.1	8.6	7.9
6	9.6	9.4	9.7	9.8	9.3	8.8
7	11.7	11.4	11.6	11.8	11.2	10.7
8	11.8	11.4	11.9	11.7	11.4	10.8
9	10.7	10.4	10.7	10.8	10.4	10.1
10	9.8	9.7	9.9	10.1	9.5	9.0
11	9.1	8.5	8.6	9.0	8.6	8.0
12	8.1	8.0	8.2	8.4	7.8	7.3
13	7.7	7.4	7.5	7.9	7.5	7.0
14	5.5	5.3	5.4	5.8	5.4	5.2
15	4.7	4.6	4.8	4.6	4.1	4.3

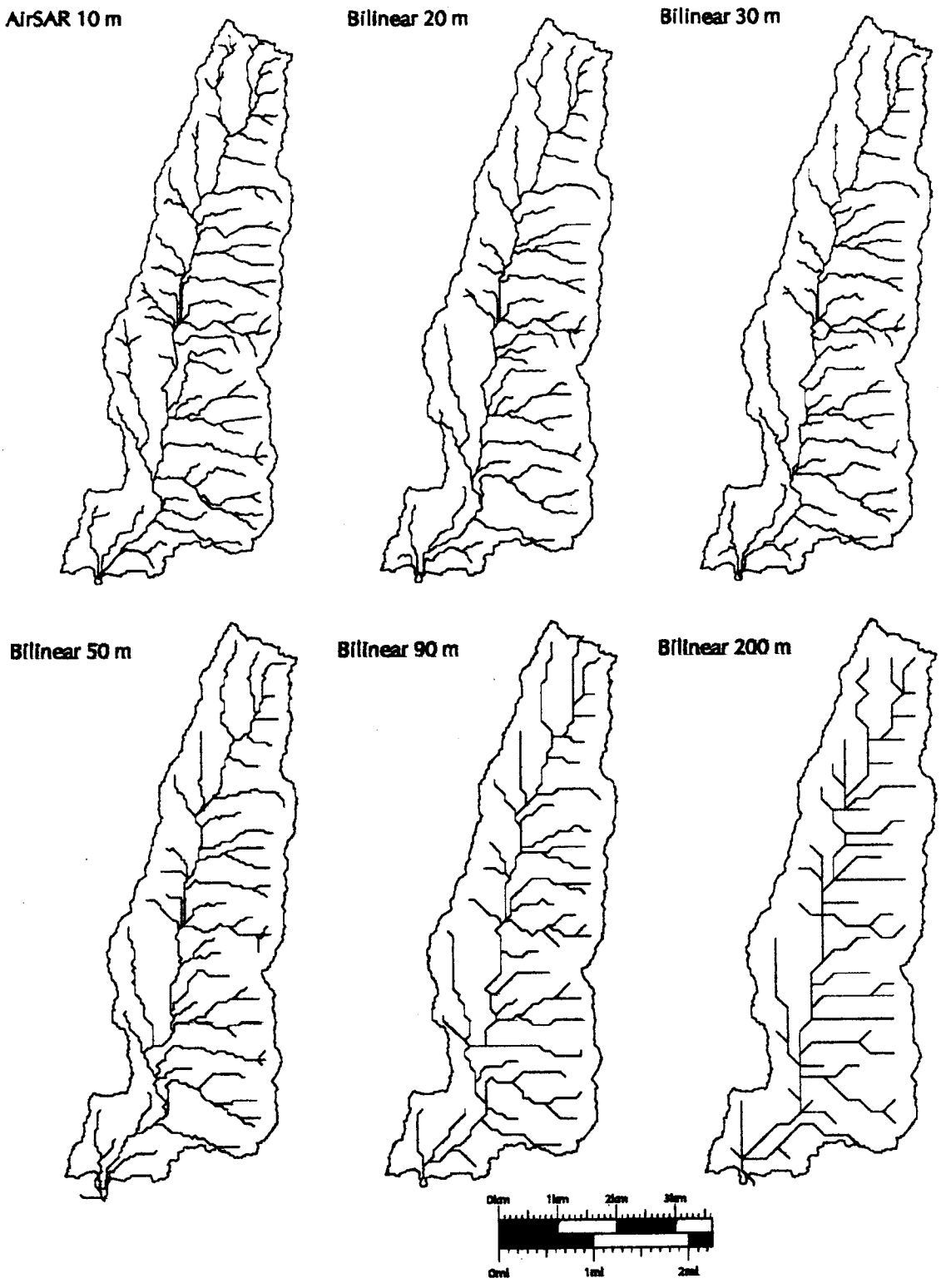

Figure 4.6a. Stream networks derived from bilinear DEMs.

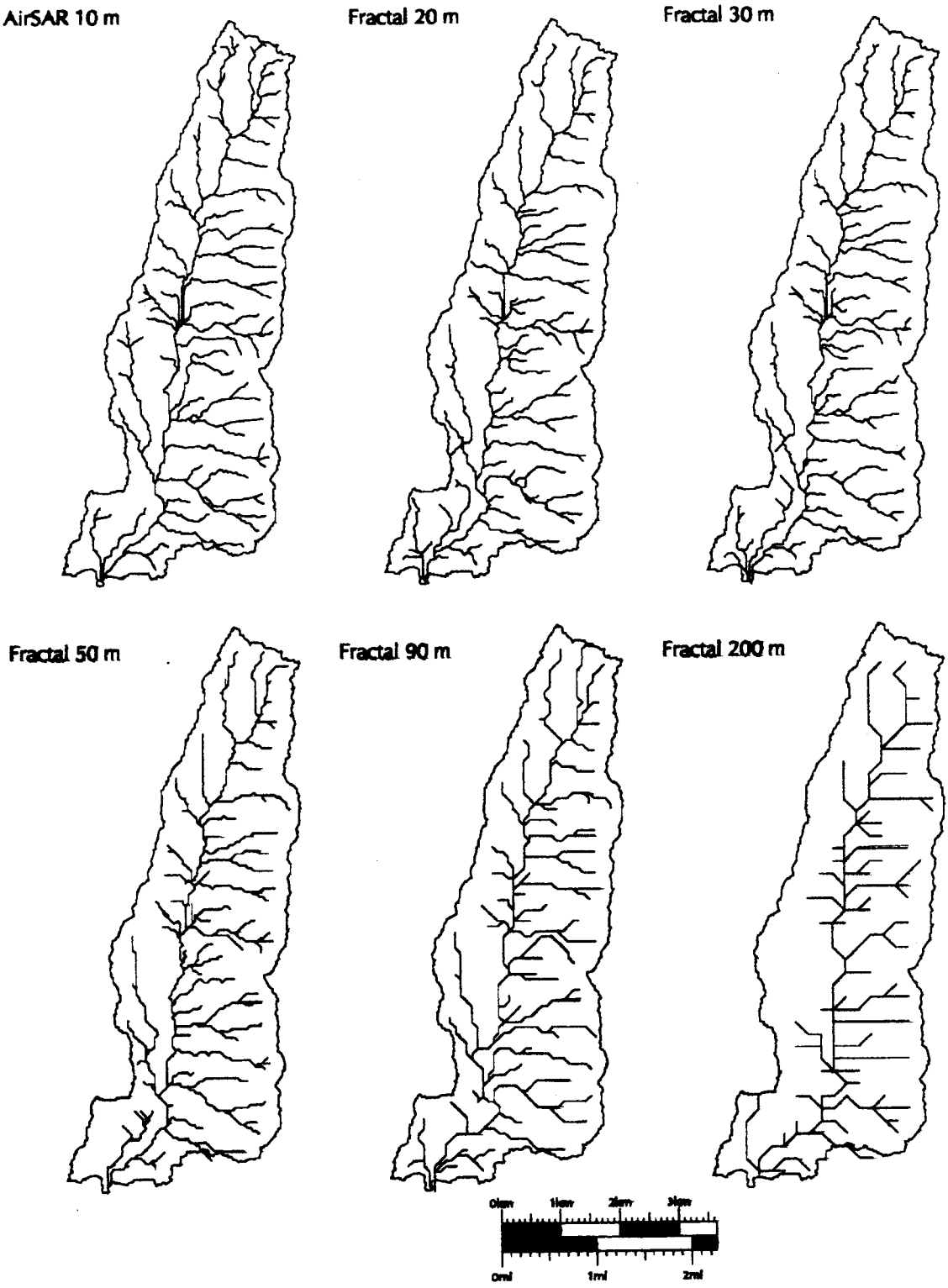

Figure 4.6b. Stream networks derived from modified-fractal DEMs.

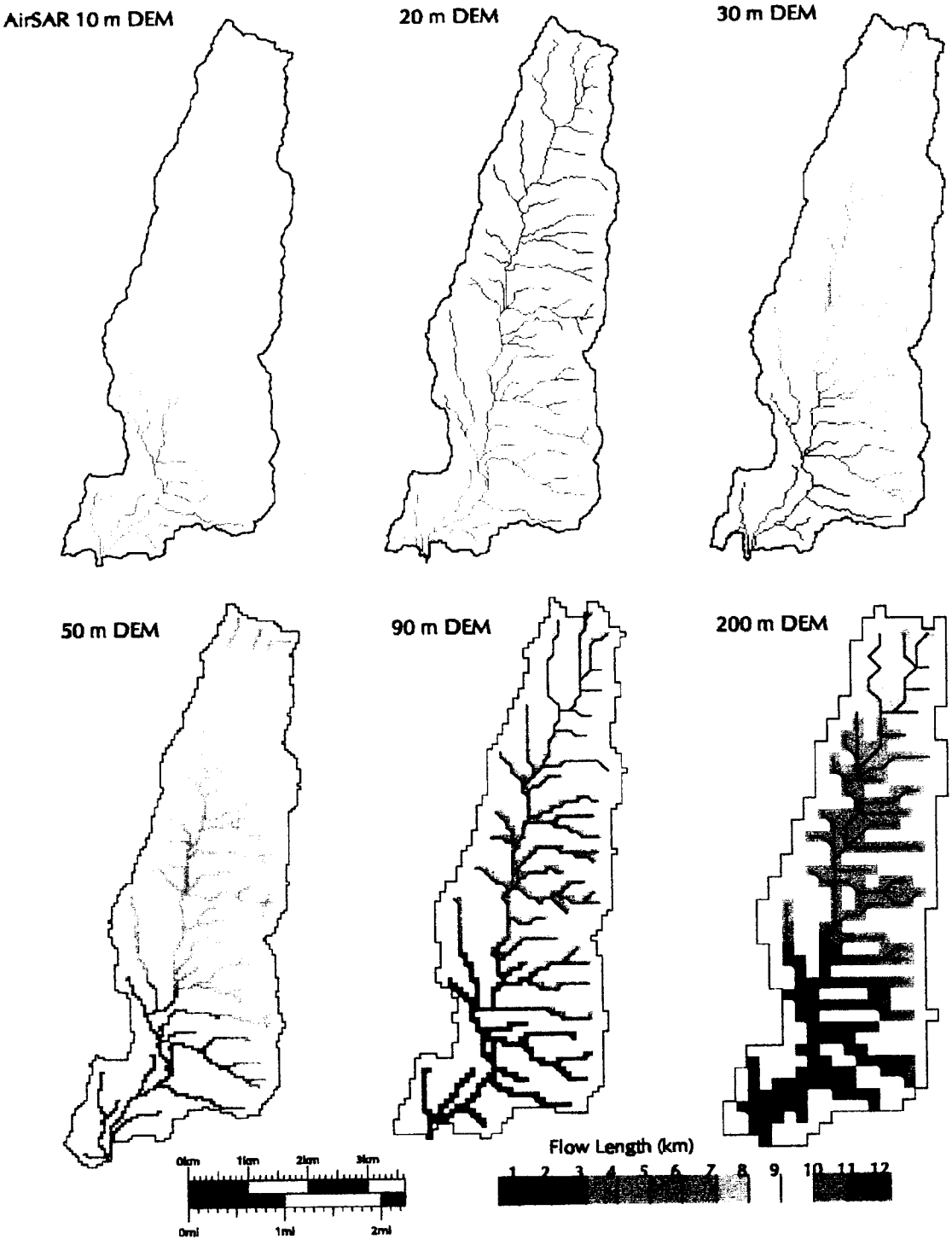

Figure 4.7. Flow length to outlet calculated from bilinear DEMs.Total flow length does not vary systematically with pixel size.

The observation that surface flow path complexity is not systematically related to average flow path length is significant in itself, but also calls into question the assumption of similarity between surface and subsurface pathways. However, there is a relationship between pixel size and DEM-derived stream density (Table 4.4).

Table 4.4 Stream density of Paul Creek catchment calculated at different resolutions.

Resolution (m)	Stream Density (km/km^2)
10	2.96
20	2.88
30	2.86
50	2.64
90	2.38
200	2.12

There is a clear decrease in stream density (and increase in average subsurface path length) for the lower resolution DEMs, meaning that on-average after infiltration water must travel a longer distance before encountering a stream channel. Since subsurface flow is much slower than streamflow, lower stream density will effectively retard modeled catchment response under subsurface flow dominated conditions. In the previous section, it was determined that average slope at each pixel also decreases at coarser horizontal resolutions. These two effects are additive and work to reduce head gradients from pixel to pixel.

4.2.4 Topographic Index

The TOPMODEL semi-distributed modeling system is a collection of concepts describing hydrologic processes using a *topographic index* as a measure of hydrologic similarity from pixel to pixel within a catchment (Beven and Kirkby, 1979; Quinn et al., 1995; Bruneau et al., 1995). The topographic index reflects the tendency of water to accumulate in regions with a large contributing area and relatively low relief. For the purposes of this study, the topographic index is defined as

$$\tau = \ln(a/\tan(\beta))$$

where a is the contributing area per unit contour length and tan β is the local slope in the direction of steepest descent. This equation is applied in a distributed fashion to individual pixels within a watershed. Similar topographic index values imply similar hydrologic behavior among pixels, with high topographic index values indicating a tendency for water to accumulate and generate overland flow. Even though TOPMODEL was not used in this study, there is some similarity between the topographic index and the method of moisture routing in DHSVM, so the relationship between pixel size and topographic index may provide some insight into DHSVM behavior.

The topographic index was calculated for DEMs at 10, 20, 30, 50, 90 and 200 m resolution. The algorithm used to fill sinks within the DEM increases the elevation of a sink pixel until it is equal to its lowest nearest neighbor. A side-effect of filling sinks is the creation of pixels with slope values of zero. The equation for topographic index approaches infinity for slopes approaching zero. In Figure 4.8, high values of topographic index are shown in red and low value are shown in dark blue. The finer resolution DEMs have more pixel-to-pixel variability than the coarser resolution DEMs. This suggests that head gradients are larger and as a result moisture will be more spatially concentrated in model runs using the coarser DEMs.

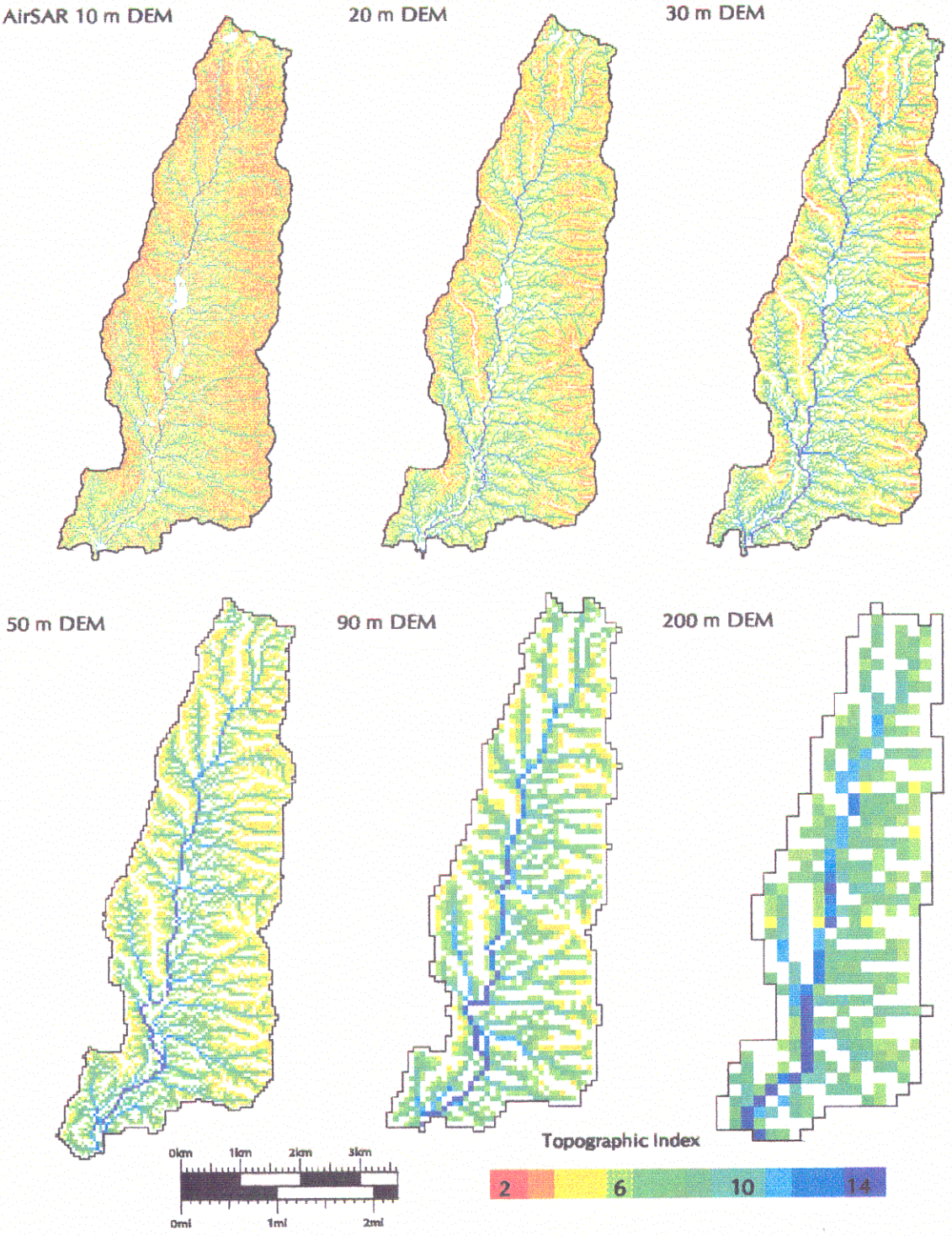

Figure 4.8. Topographic Index calculated from DEMs created via bilinear interpolation.

In conclusion, the DEMs prepared using the bilinear method reproduced hydrologically important topographic features more accurately than those prepared using the modified-fractal method. As a result, only the bilinear DEMs have been used for the DHSVM model experiments described in Chapter 6. As DEMs were aggregated to progressively coarser resolutions, average catchment slopes decreased and the range of slopes (from steepest to flattest) was noticeably reduced. The in-channel flow lengths estimated from DEM-derived stream networks did not vary systematically as a function of pixel size, but drainage density was reduced as pixel size increased, so the effective subsurface path length did increase. Analysis of topographic index values shows higher resolution DEMs have more pixel-to-pixel variability. These investigations of geomorphic parameters suggest that under saturated conditions, the reduced average slopes and increased subsurface path lengths of the coarser DEMs would retard and likely reduce simulated streamflows relative to finer scale model runs. The effect of increasing pixel size on topographic index reduces downslope water movement and may reduce simulated areas of saturation excess compared with model runs at finer resolution.

CHAPTER 5: MODEL CALIBRATION

The Distributed Hydrology Soil Vegetation Model (DHSVM) was calibrated using the Paul Creek observed streamflow record. Melbourne Water operated a gauge on Paul Creek from October 1978 to April 1983. Drought conditions persisted from 1982 through the end of the period of record, so 4 years with appreciable runoff were available for model evaluation. A split test was used for model testing on the remaining data: 2 years of model calibration and 2 years of model verification. It was assumed (and later verified) that the resolution chosen for model calibration would greatly affect model predictions at other resolutions, and that the best model performance would occur at the calibrated resolution and not necessarily the finest resolution. For calibration/verification, the model was run at 50 m resolution with 3 hour time steps. The resolution allowed for relatively short model simulation times and catchment parameters that were approximately the average of the finest and coarsest DEMs. The modeling setup, calibration and results will each be described in detail in this chapter.

5.1 DHSVM INPUT FILES

Distributed, physically based hydrology models require a substantial amount of input data to characterize the hydrologic system. DHSVM requires input files for topography, soils, vegetation, meteorology and stream routing. Each of these is described in this chapter with the exception of topography which was described in detail in Chapter 3.

5.1.1 VEGETATION CHARACTERISTICS

A set of digital maps describing the vegetation characteristics of the Paul Creek catchment area were provided by Natural Resource Systems of Victoria, Australia (NRS; http://www.nrsc.com.au). Among the vegetation characteristics included in these data

sets are dominant species, sub-dominant species, vegetation height and fractional canopy coverage at 1:100,000 scale. These data were derived from a combination of Landsat imagery, ground surveys and other pre-existing data sets.

The NRS maps include some vegetation data collected during the 1990's. There was some concern that the NRS data would not accurately represent conditions during the period of modeling, because of post-1981 land use changes. Potential land-use changes were investigated by comparing the detailed NRS vegetation maps with separate NRS data showing forested extent in 1972 and 1987. No changes in forest cover were observed from 1972 to 1987, or 1987 to present, so it was assumed for this investigation that the detailed NRS vegetation data accurately reflect the vegetation conditions during the 1978 – 1981 simulation period. Figure 5.1 and Table 5.1 show the distribution and description of vegetation classes used to model the Paul Creek catchment. Additional vegetation parameters required by DHSVM were derived from published field values (see Roden and Ball, 1996; Stoneman et al., 1996; Vertessy et al., 1995; Myers et al., 1996)

Table 5.1 Parameters extracted from NRS vegetation data.

Vegetation Class	Dominant Species	Height (m)	Sub-dominant Species	Canopy Closure
1	Red Stringybark (Eucalyptus macrorhyncha)	12	Broad Leaf Peppermint (E. dives)	0.35
2	Red Stringybark (E. macrorhyncha)	12	Unclassified	0.35
3	Forest Red Gum (E. tereticornis)	25	Unclassified	0.35
4	Messmate Stringybark (E. obliqua)	25	Narrow Leaf Peppermint (E. radiata)	0.65
5	Messmate Stringybark (E. obliqua)	25	Unclassified	0.65
6	Messmate Stringybark (E. obliqua)	35	Mountain Grey Gum (E. cypellocarpa)	0.90
7	Messmate Stringybark (E. obliqua)	35	Unclassified	0.90
8	Mountain Ash (E. regnans)	45	Unclassified	0.90
9	Grass-land	0.1	Unclassified	N/A

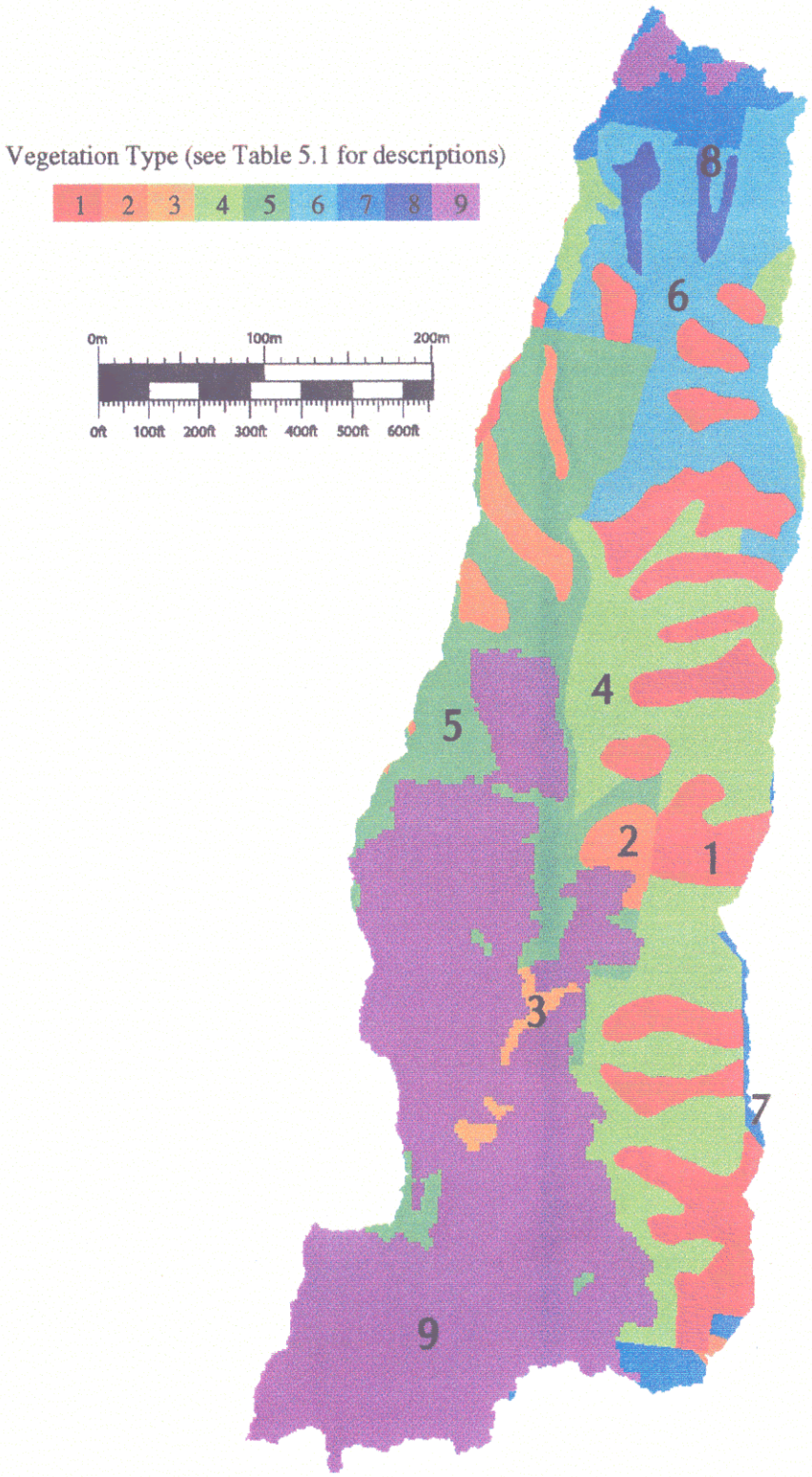

Figure 5.1 Distribution of vegetation types within the Paul Creek catchment.

5.1.2 PAUL CREEK SOIL CHARACTERISTICS

Soil characteristics were obtained from a study entitled *An Agricultural Land Use Capability Survey of the Yarra Glen Area* by J.J. Maher (1952). This publication was provided by Tom Imhof and Ruth Lourey of the Victoria Bureau of Natural Resources and Environment (Victoria NRE). A series of 97 soil samples and general features in the underlying geology were used to create a series of 1:50,000 scale maps (15'x15' in extent) delineating trends in agricultural potential in the Yarra Glen Area. One of these maps, describing soil types, was digitized and imported into Arc/Info. Figure 5.2 and Table 5.2 show the distribution and description of soil types and depths within the Paul Creek catchment. Addition soil parameters required by DHSVM were derived using published relationships (Rawls et al., 1993; Bowling and Lettenmaier, 1997).

Table 5.2 Soil Classification and Depth

Soil Number	Soil Description Upper / Lower	Soil Depth (m)
1	Silt-Clay Loam / Medium Clay	1.2
2	Silt Loam / Medium Clay	1.2
3	Silt Loam / Heavy Clay	1.2
4	Sandy Silt Loam / Medium-Heavy Clay	1.4
5	Silt Loam / Light-Medium Clay	0.7
6	Silt Loam / Light-Medium Clay	1.1
7	Silt Loam / Heavy Clay	0.8
8	Silt Loam / Heavy Clay	0.5

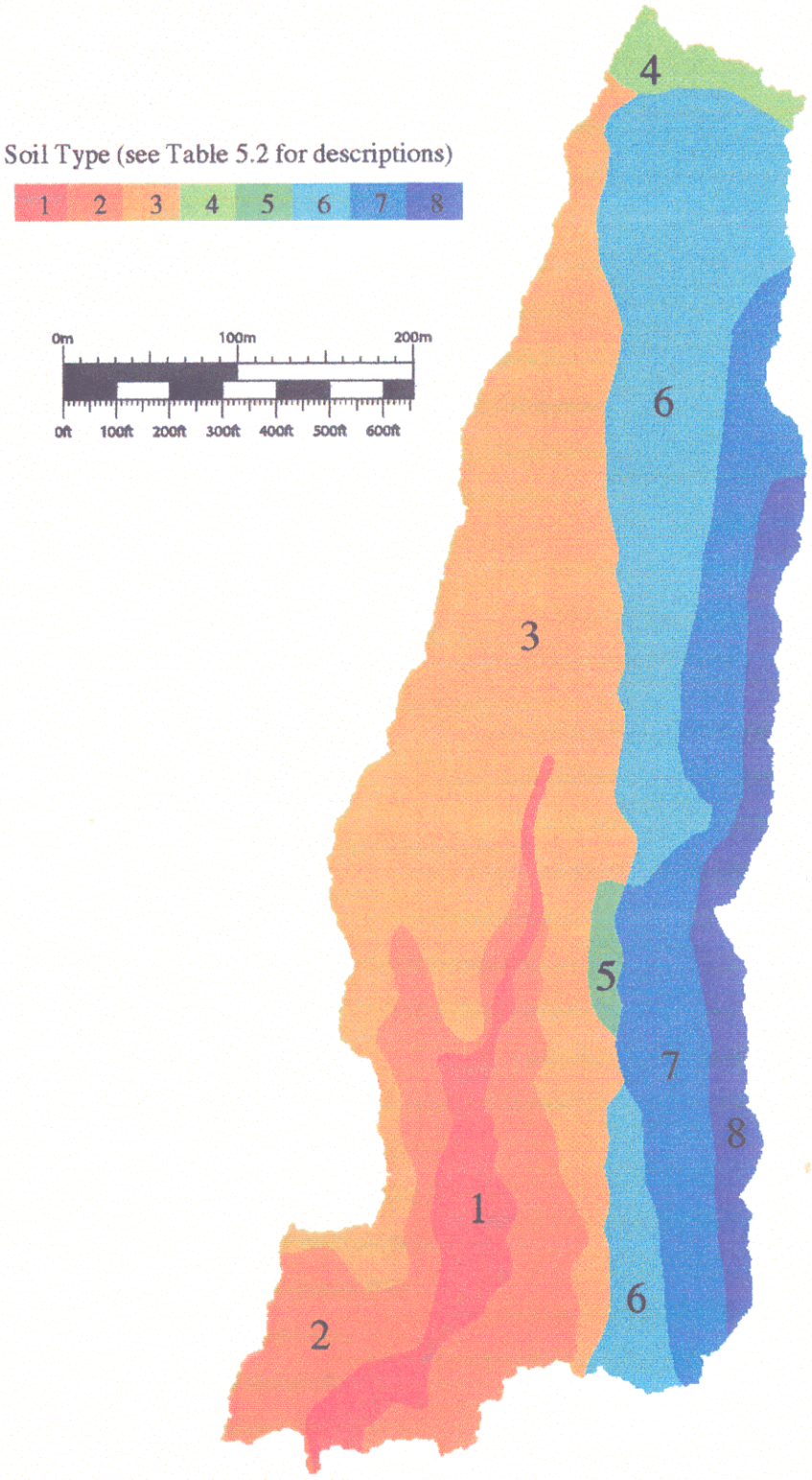

Figure 5.2 Distribution of soil types and depths within the Paul Creek catchment.

5.1.3 METEOROLOGY OF PAUL CREEK

The Australian Bureau of Meteorology (Australian BOM) maintains the Mount St. Leonard Experimental Research Station (37.6 S; 145.5 W; 603 m) located approximately 4 km east of the catchment boundary. At Mount St. Leonard, a continuous recording pluviograph was in operation during the period of modeling. The pluviograph data were subsequently digitized by the Australian BOM into 10 minute intervals. The pluviograph coverage is greater than 90% on days when rainfall occurred[4]. For the meteorological input file, the pluviograph data were aggregated to 3 hour intervals and any missing data were filled from a separate daily precipitation data series which is available for Mount St. Leonard.

Because the Mount St. Leonard weather station is located outside the basin boundary, there was some concern that the observed precipitation at Mount St. Leonard may be poorly correlated with the timing and volume of precipitation within the Paul Creek catchment. To address this concern, the following checks were performed to test the meteorological connection between Mount St. Leonard and Paul Creek:

- An automated weather station has recorded precipitation at 6 minute intervals in the Tarrawarra catchment since August, 1996 (Western and Grayson, 1998). The timing and volume of precipitation at Mount St. Leonard stations were compared to that at Tarrawarra from August, 1996 to August, 1997. It was observed that the timing of precipitation at the 2 sites was consistently similar, suggesting that Tarrawarra and Mount St. Leonard are generally located along the same storm tracks. The similarity of precipitation timing established that a meteorological connection exists between Mount St. Leonard and Tarrawarra. Since the Paul Creek catchment is aligned between these weather stations, it was assumed that observations at either Tarrawarra or Mount St. Leonard are sufficient to determine whether precipitation is falling at

Paul Creek. The Mount St. Leonard Station consistently received a greater volume of precipitation, but the magnitude of the orographic effects varied from event to event. This suggests 2 precipitation stations are required to estimate the volume of precipitation at Paul Creek. However, the Tarrawarra station was not in operation during the period of modeling.

- The volume of daily precipitation at the Tarrawarra weather station was compared with data collected at the Maroondah Weir daily precipitation station (37.7 S, 145.5 W; 149 m) located approximately 15 km south east of the Paul Creek stream gauge for the period from August, 1996 to August, 1997. On a daily basis, the Tarrawarra and Maroondah Weir stations were found to receive similar volumes of precipitation. Since the Maroondah Weir precipitation station was in use during the model study period, the difference in daily precipitation volumes between Mount St. Leonard and Maroondah Weir and the difference in elevation were used to calculate a new precipitation lapse rate on a daily basis. It should be noted, the Maroondah Weir station was only used to calculate a precipitation lapse rate and not as a second weather station because only daily precipitation values were available.

Temperatures were estimated on three hour intervals from daily maximum and minimum readings (T_{max} and T_{min}) collected at Mount St. Leonard Station and Scoresby Research station (37.9 S; 145.25 W; 90 m) using the method described by Anderson (1968):

$$T_{0-3} = 0.19\,T_{min\,-1} + 0.81\,T_{min}$$
$$T_{3-6} = 0.05\,T_{min\,-1} + 0.95\,T_{min}$$
$$T_{6-9} = 0.02\,T_{min\,-1} + 0.68\,T_{min} + 0.30\,T_{max}$$
$$T_{9-12} = 0.40\,T_{min} + 0.60\,T_{max}$$
$$T_{12-15} = 0.213\,T_{min} + 0.763\,T_{max} + 0.024\,T_{min\,+1}$$
$$T_{15-18} = 0.025\,T_{min} + 0.95\,T_{max} + 0.05\,T_{min\,+1}$$
$$T_{18-21} = 0.0125\,T_{min} + 0.6275\,T_{max} + 0.36\,T_{min\,+1}$$
$$T_{21-24} = 0.33\,T_{max} + 0.67\,T_{min\,+1}$$

---

[4] Data coverage was based on comparison with separate Mount St. Leonard daily precipitation data.

Relative humidity was calculated by assumpting that T_{min} corresponds to the dew point temperature (Shuttleworth, 1993). Wind speed was calculated based on a regression developed from measured temperature and time of day at the Tarrawarra automated weather station. The Tarrawarra wind measurements were collected at a height of 2 m in an open pasture land. Estimated wind speeds generally varied from 2 to 7 m/s.

Clear sky radiation data were calculated using a version of Solarflux for Arc/Info (Rich et al., 1995) which had been modified to match output specifications of DHSVM (Storck et al., 1998). This model computes direct and diffuse solar radiation based on latitude, date and time of day, pixel slope and aspect, and the effects of hill shading.

5.1.4 STREAM ROUTING

DHSVM uses an explicit flow routing scheme based with estimates of stream geometry and Manning's roughness coefficient required for each stream segment. Derivation of stream channel networks from DEMs was discussed in Chapter 4. DHSVM requires that channel segments be organized into stream classes. Field observations of channel width and depth were only available at the catchment outlet, so upstream channel geometry had to be estimated. Due to the linear configuration of the channel network (see Figure 4.6), the commonly used Strahler stream ordering scheme was not an appropriate method for estimating channel parameters. Specifically, the Strahler scheme classifies Paul Creek as a 4^{th} order catchment with the main stem of Paul Creek becoming 4^{th} order after draining approximately ~1/8 of the catchment area. Instead, stream classes were defined by approximating the source area contributing to each stream segment. This allowed the main stem to increase in size closer to the outlet. Table 5.3 shows the parameters assigned to each stream class. The same Manning's coefficient of friction was used for each stream class, because model predictions were relatively insensitive to this parameter.

Table 5.3 Paul Creek channel parameters

Stream Class	Width (m)	Depth (m)	Manning's n
1	0.4	0.15	0.023
2	1.0	0.4	0.023
3	1.6	0.65	0.023
4	2.2	0.90	0.023
5	2.8	1.15	0.023
6	3.4	1.40	0.023
7	4.0	1.65	0.023
8	4.6	1.90	0.023
9	5.2	2.15	0.023
10	5.8	2.40	0.023
11	6.4	2.65	0.023

5.2 DESCRIPTION OF THE HYDROLOGY OF PAUL CREEK

The Paul Creek catchment is subject to infrequent periods of intense rainfall. Although the total yearly precipitation averages 1.0 m, more than 80% of the annual precipitation falls in just 14 days. There is rarely snow and prolonged periods with sub-freezing temperatures were not observed in the meteorological data record. The fraction of precipitation observed at the channel outlet is extremely low, approximately 5% from 1978 - 1981. Melbourne Water operated the Paul Creek gauge for water resource and diversion purposes, so low flow readings are relatively inaccurate (Andrew Western, *personal communication*). The upper portion of the catchment is situated in a land preserve and contains few roads. The lower portion of is largely agricultural and also contains few roads. There are a few ponds visible in both AUSLIG maps and AirSAR polarimetric images, but there are no residential regions or published diversions above the gauge.

From a DHSVM modeling standpoint, the Paul Creek catchment presents a few challenges. One challenge arises from the infrequency of precipitation and typically dry antecedent conditions. As precipitation begins to fall, the catchment progresses from dry

to wet, and streamflow is difficult to model while the moisture storage in the catchment is undergoing a rapid change. Maher (1952) observed perched water tables tend to form in the lower, flatter portion of the catchment during the wet season. The current configuration of DHSVM assumes the water table builds from the bottom of the deepest soil layer. The rapid translation of precipitation into streamflow as observed from the measured hydrograph response suggests that overland flow is generated either by saturating the relatively thin, friable soil layer overlaying the perched water table or by the Hortonian mechanism of precipitation excess.

5.3 MODEL CALIBRATION

DHSVM has been applied in humid, temperate catchments of the Pacific Northwest (Strock et al., 1995; Bowling and Lettenmaier, 1997). The rapid and infrequent hydrologic response of Paul Creek is dissimilar from previous model applications. The following steps were used for model calibration:

1. Leaf area index and stomatal resistances were adjusted until the observed and simulated water balances were sufficiently similar.

2. Soil conductivity and infiltration rates were adjusted until simulated hydrograph magnitude and timing were similar to observations.

It was recognized that accurate soil moisture initialization is important in hydrologic modeling. At various times during the calibration process, initial soil moisture was estimated by running a model simulation in which the meteorological data from the year preceding the observed streamflow record (October 13, 1977 to October 12, 1978) were used in a continuous loop to drive DHSVM until the soil moisture in each soil layer converged to a specific value. The results of model calibration experiments for 1978 and 1979 are shown in Figure 5.3 and Figure 5.4. The two wet seasons are shown on separate plots to increase clarity. There was no appreciable runoff in the period between those shown in the figures.

The observed streamflow on 12/26/1978 (see Figure 5.3) is much greater than simulated streamflow. The observed precipitation for the duration of the storm was approximately 60 mm compared with 20 mm of runoff. This runoff fraction was considerably higher than what was observed for other storm events during the period of record, which may explain why the model under-predicted the hydrologic response. It is possible that the storm driving this peak event followed a different track, depositing a significantly larger volume of precipitation in Paul Creek than at the Mount St. Leonard Station.

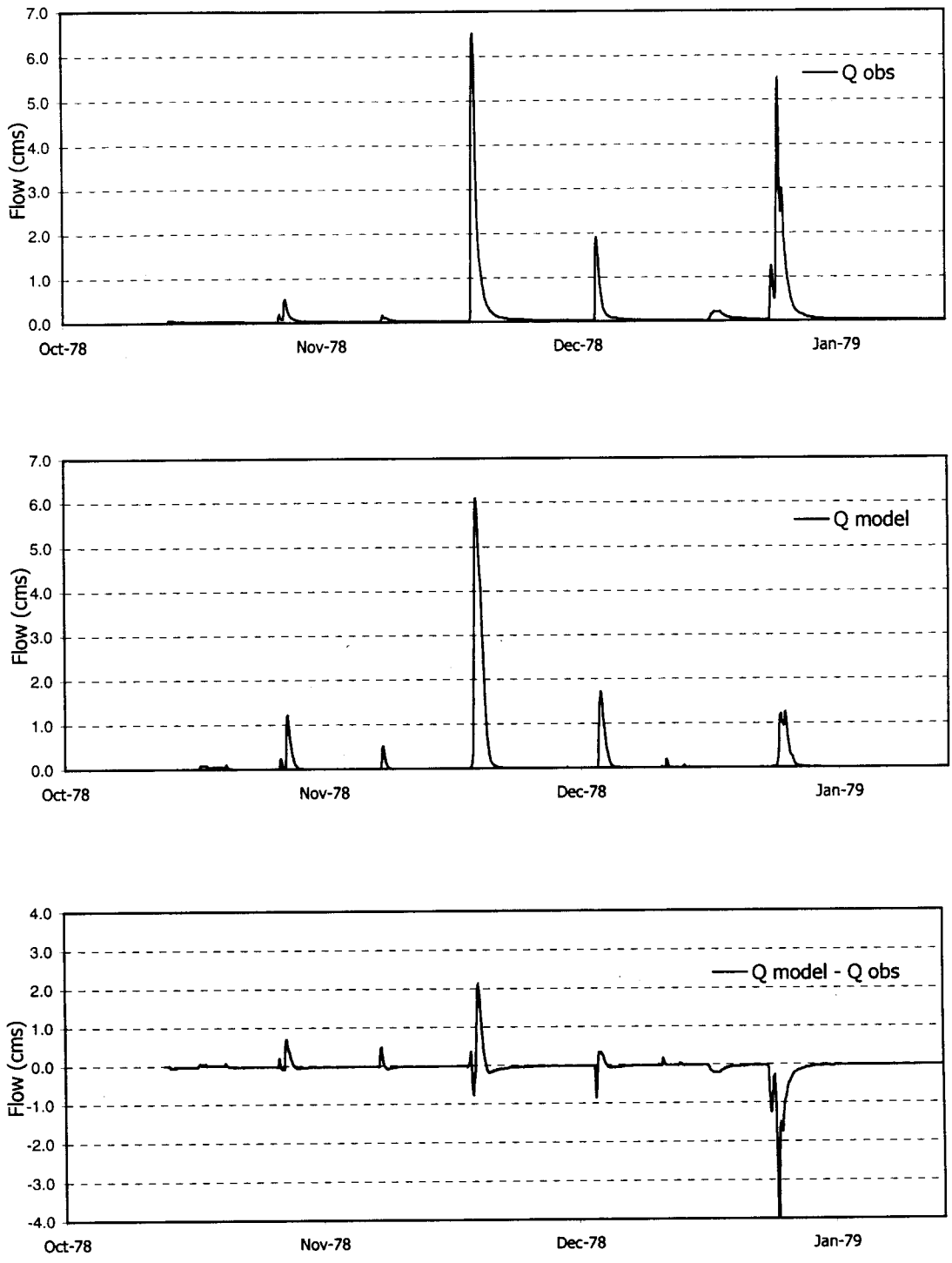

Figure 5.3 DHSVM streamflow calibration for the 1978 wet season.

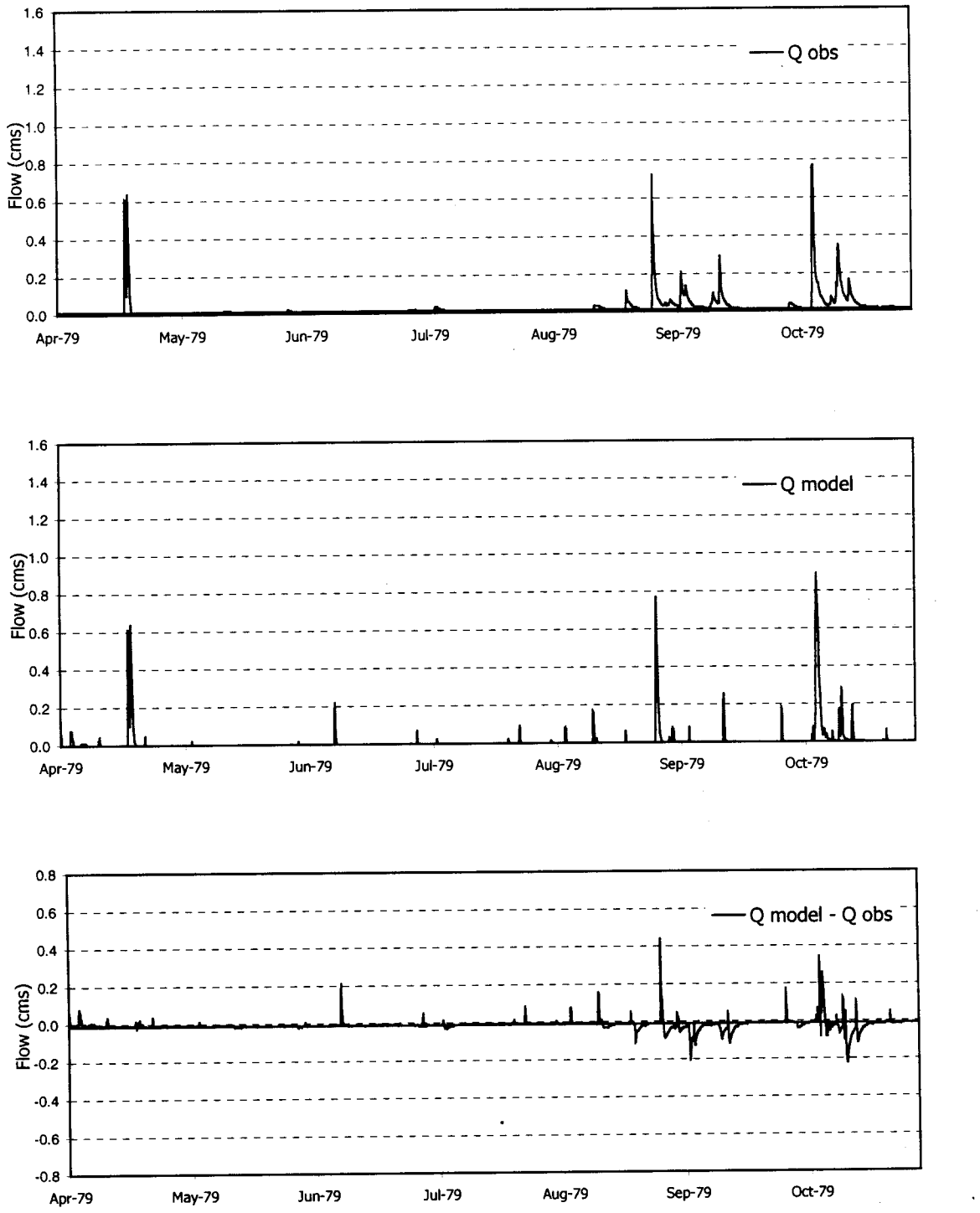

Figure 5.4 DHSVM streamflow calibration for the 1979 wet season.

CHAPTER 6: MODEL RESULTS

The results from a variety of DHSVM simulations at resolutions of 10, 20, 30, 50, 90 and 200 m are presented in this chapter. The results are presented in the following order:

- The model calibration is verified by comparing observed and simulated streamflows from 1980 and 1981.
- Specific storm events are investigated to evaluate the importance of rainfall rates and antecedent conditions on runoff.
- The effect of pixel size on monthly averaged discharge and storm flows for specific events is investigated.
- The effect of pixel size on streamflows is examined given initially wetter soil conditions. The wetter soils are intended to increase the generation of lateral subsurface flow.

6.1 MODEL VERIFICATION

Using the calibrated 50 m parameter set, the results of model simulations at 50 m were compared with observed streamflow data from 1980 and 1981 in order to verify that DHSVM was representing the hydrologic behavior of Paul Creek with sufficient accuracy. These results are shown in Figures 6.1 and 6.2. As in Figures 5.3 and 5.4, in order to improve clarity, only the periods with appreciable runoff production are shown.

The hydrology of Paul Creek is characterized by infrequent, high storm flows, quick hydrograph recession and very low baseflow. To model this type of response, soil infiltration rates were varied during calibration to allow for surface ponding during heavy precipitation events and complete infiltration during lighter precipitation events. Within DHSVM, ponded water moves from pixel-to-pixel in the direction of steepest decent at a rate of 1 pixel per model time step, with infiltration occurring if the destination pixel does not contain surface water. Since heavy precipitation events generally occur for only at most a few model time steps, only pixels located near a stream would contribute to runoff

via the model's overland flow mechanism. It should be noted that the overland flow algorithm is both time step and pixel size dependent.

DHSVM adequately models storm response during 1980, a year which was meteorologically similar to 1978 and 1979. The timing and magnitude of peak flows are in general well reproduced. However, for some storm events the simulated stream response to precipitation occurred somewhat less rapidly than observed storm response. This lead time was generally no more than 1 model time step (3 hours). A consistent problem during model calibration was the occurrence of simulated streamflow peaks when no changes in streamflow were observed. In order for overland flow to develop, the rainfall rate must surpass an infiltration threshold. Since this threshold between increased streamflow and constant streamflow is narrow, small differences between model precipitation and actual precipitation can have an exaggerated effect on simulated streamflows. This was observed for two precipitation events during early October, 1980 (see Figure 6.1). Despite the noted differences between simulated and observed streamflows during 1980, the results verify that DHSVM calibration performed for 1978 and 1979 was adequate to reproduce the hydrologic response of Paul Creek during 1980.

The simulated streamflow record for 1981 deviates from the observed streamflow record more than the 1980 simulated data. More precipitation was received during the 1981 wet season than in any of the previous 3 years. In particular, a rapid succession of storms from mid-July through the end of August produced a series of peak flows. Between storm events the observed streamflows remained significantly higher than the baseflow conditions observed in other years. During this period, the DHSVM consistently underpredicted streamflows. It is likely that the relatively more intense 1981 wet season was sufficient to saturate a significant fraction of the basin intermittently, allowing saturation excess to become a viable runoff generation mechanism, and enabling a greater portion of the catchment to contribute to streamflow. Because these conditions were not seen during the calibration period, DHSVM simulations did not adequately reproduce the extensive wetting and subsurface lateral moisture transport evident during 1981.

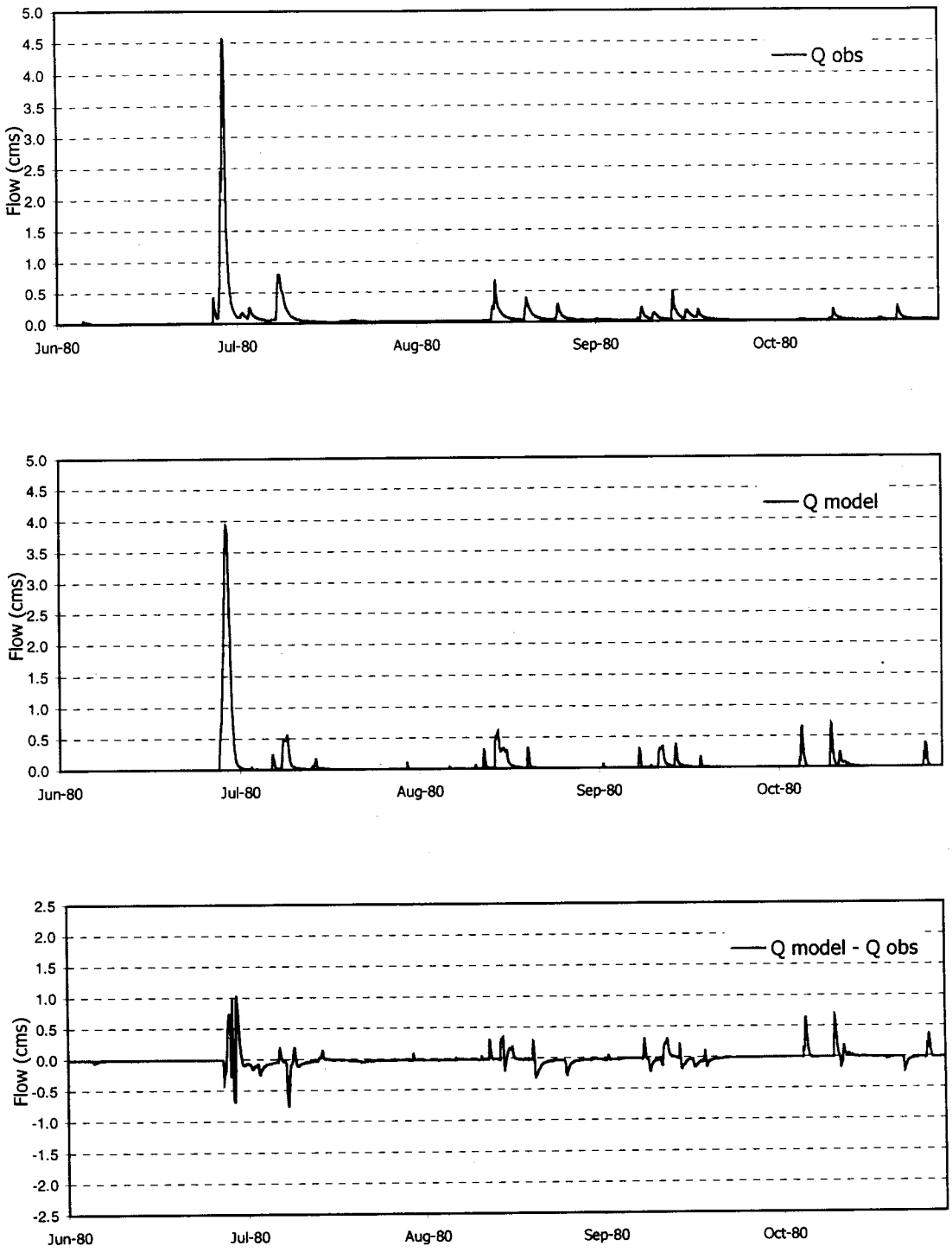

Figure 6.1 Observed and simulated streamflows for the 1980 wet season.

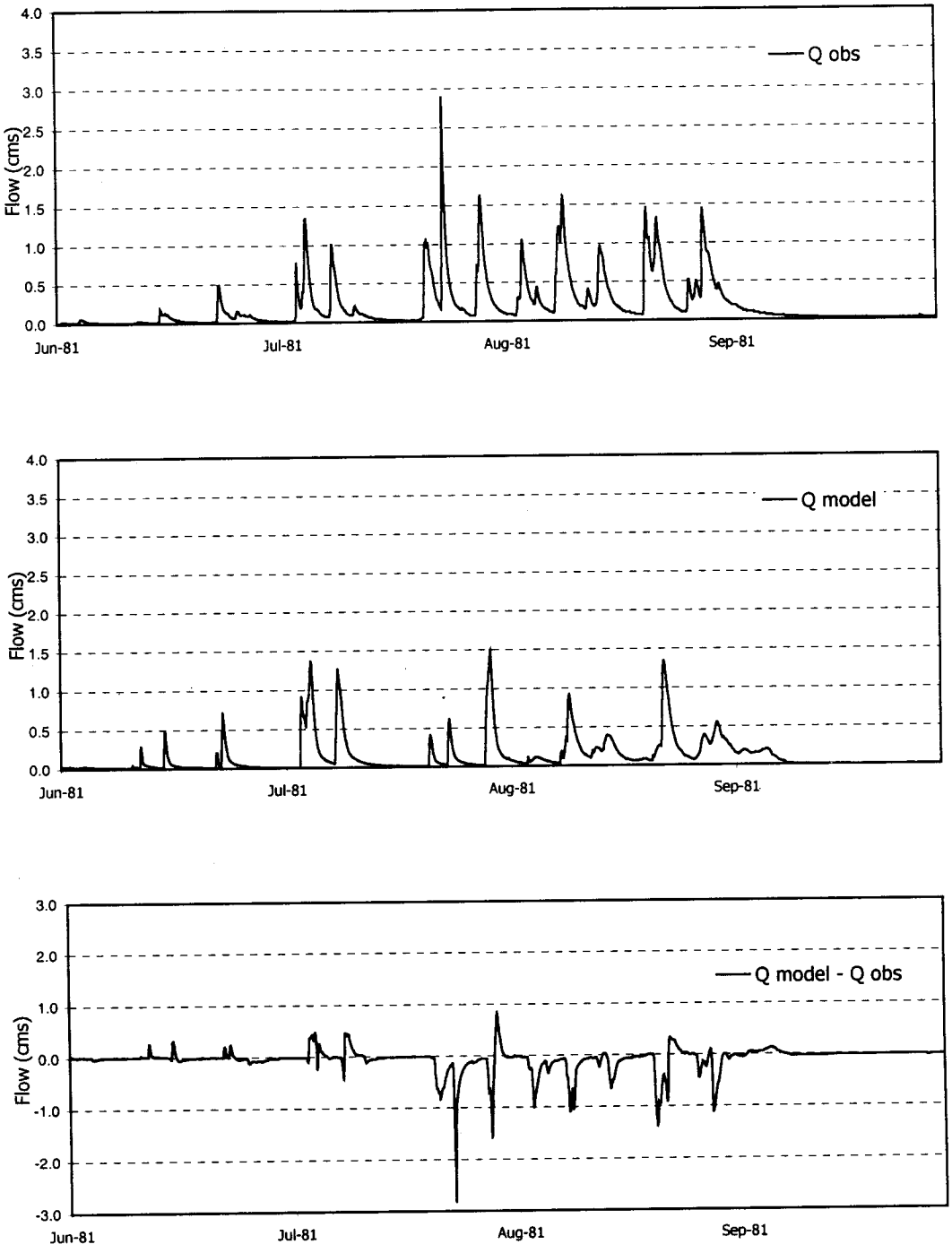

Figure 6.2 Observed and simulated streamflows for the 1981 wet season. Paul Creek received significantly more rainfall in 1981 than the calibration years.

6.2 DISTRIBUTION OF PRECIPITATION AND RUNOFF

Table 6.1 shows the integrated performance of DHSVM by summarizing the average monthly precipitation, observed and simulated (50 m) discharge from October 1978 to December 1981. The long term average annual precipitation is approximately 1 m with somewhat higher precipitation observed during the period of study. DHSVM tended to overpredict certain storm events and consistently underpredict the observed baseflow. The gauge on Paul Creek was used for water resource purposes and the low flow readings are not as accurate as storm flows (Andrew Western, *personal communication*). Thus there was no way to verify the accuracy of model baseflow predictions.

Table 6.1 Monthly average precipitation, observed and simulated discharge.

Month	Precipitation (mm)	Observed Discharge (mm)	Simulated Discharge (mm)
January	66.8	1.6	2.0
February	43.8	1.0	1.3
March	138.3	0.9	2.3
April	55.2	1.7	1.9
May	83.9	1.7	7.5
June	68.2	8.8	9.0
July	76.2	16.0	13.3
August	100.4	21.8	17.8
September	60.6	5.4	3.4
October	128.0	4.5	4.3
November	105.6	11.1	9.9
December	116.9	11.3	8.8
Total	**1044**	**85.8**	**81.5**

The amount of precipitation falling at Paul Creek is generally higher in the wet winter and spring season (May - November), although precipitation is less temporally concentrated than discharge. Model simulations suggest the increased concentration of higher streamflows occurs because (1) precipitation rates high enough to generate either overland flow are concentrated in the wet season, and/or (2) increased near stream soil moisture storage during the wet season allows some saturated response. An example emphasizing each of these phenomena is shown below.

Within Paul Creek, infiltration rates vary from 1 to 60 mm/hr[5]. In general, precipitation rates in excess of approximately 2.5 mm/hr (7.5 mm per model time step) were required by DHSVM to generate increased streamflow, although this threshold was somewhat lower in the winter. Table 6.2 shows the number of model time steps with precipitation in excess of 7.5 mm during the modeling period. There is some concentration of heavy precipitation events from May to November, but during July and August, the months with the most observed runoff, the rainfall rates for specific storms tended to be lower than in May or November. The fraction of precipitation observed at the catchment outlet was particularly low in May and November, probably due to dry antecedent conditions in May and higher evaporative losses in November.

Table 6.2 Number of precipitation events exceeding DHSVM threshold of 7.5 mm per time step.

Month	Number of Events
January	3
February	3
March	8
April	6
May	14
June	8
July	7
August	8
September	5
October	11
November	15
December	6

During the summer months, the soil moisture storage is reduced more quickly after precipitation because of increased evapotranspiration. Figures 6.3 and 6.4 demonstrate the dependence of runoff production on antecedent conditions by showing the simulated time evolution of catchment averaged soil moisture in the top 1.0 m of the soil column

[5] These values are based on observations (Maher, 1952) and subsequent model calibrations.

and simulated streamflow in response to a series of precipitation events that took place in April, 1979 (dry antecedent conditions) and August, 1979 (wet antecedent conditions).

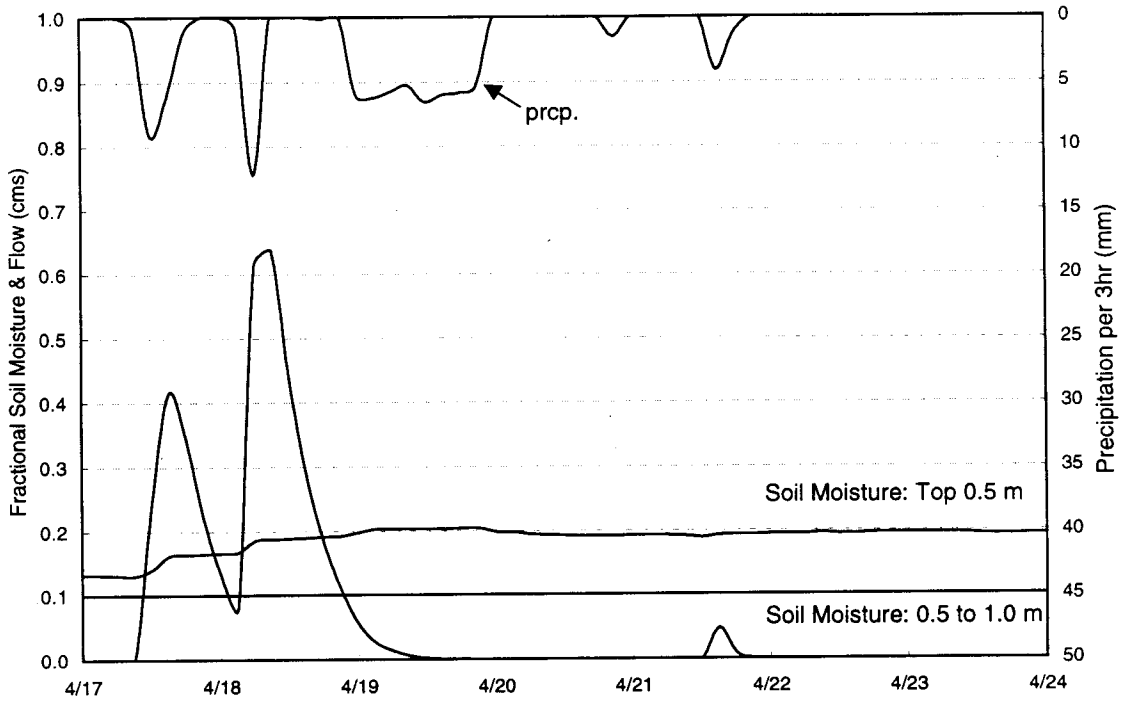

Figure 6.3 Simulated streamflow and catchment averaged soil moisture with dry antecedent conditions.

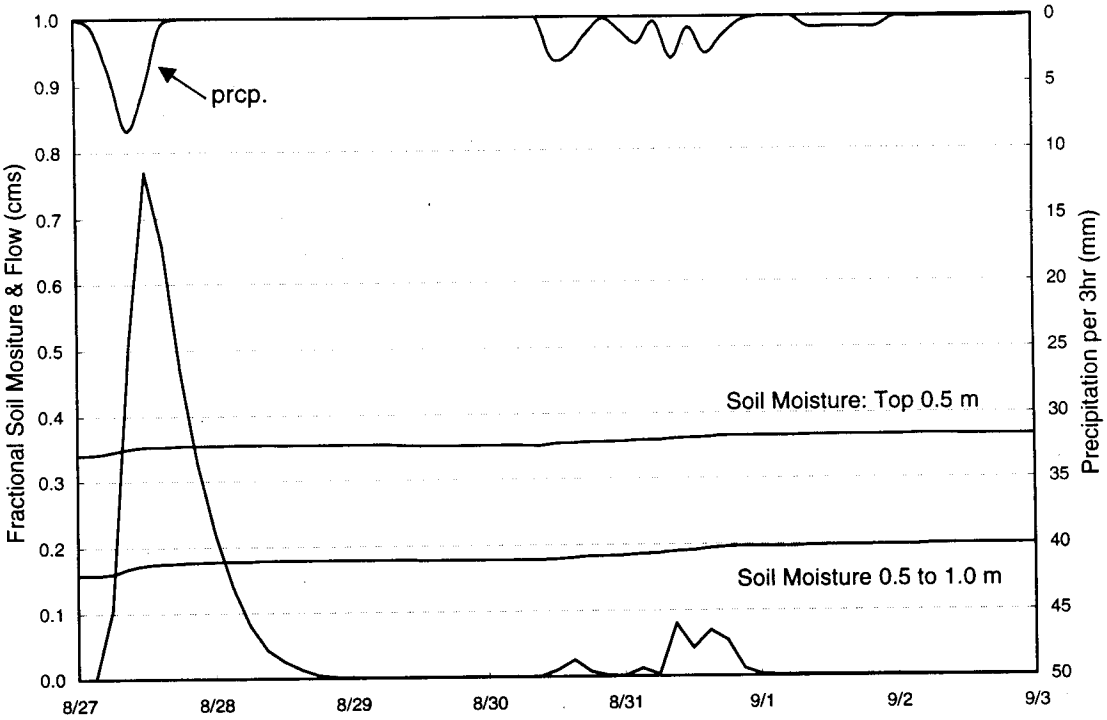

Figure 6.4 Simulated streamflow and catchment averaged soil moisture with wet antecedent conditions.

Even though infiltration excess generated overland flow is the dominant mechanism contributing to streamflow for these events, streamflow is nevertheless influenced by antecedent soil moisture. The total runoff volumes in Figures 6.3 and 6.4 are very similar even though nearly twice as much rain fell during the April event compared with the August event. The differences in storage, and (by inference) evapotranspiration account for the discrepancy in runoff production. During the April event, the dry soils retained a greater fraction of precipitation than the wet soils of the August event. Table 6.3 compares the runoff, change in storage, and evapo-transpiration volumes for the two events shown above.

Table 6.3 Rainfall partitioning under different antecedent conditions.

	Precipitation (mm)	Runoff (mm)	Δ Storage (mm)	ET* (mm)
April 17-20, 1979 (dry soils)	84.5	7.5	30.8	46.2
August 27-30, 1979 (wet soils)	46.4	7.2	20.0	19.2

* Evapo-transpiration has been calculated by differences.

On April 19, 1979, rain fell at a rate of more than 5 mm / 3hr for a period of 24 hours, however there was no simulated hydrograph peak corresponding to this precipitation even though the soils had been wetted by two previous rainfall events (see Figure 6.1). The rainfall rate on April 19, 1979 was not high enough to surpass the threshold necessary for generating infiltration excess and overland flow. These rainfall events highlight the importance of rainfall rate as well as the effect of antecedent conditions for driving hydrologic response within the Paul Creek catchment.

6.3 EFFECT OF PIXEL SIZE ON SIMULATED HYDROLOGIC RESPONSE

The effect of pixel size on simulated hydrologic response was evaluated by applying DHSVM to the Paul Creek catchment at resolutions of 10, 20, 30, 50, 90 and 200 m. Each of the model runs used the calibrated parameter set developed at 50 m resolution, so it was expected that of the simulated streamflows, those calculated at 50 m resolution would reproduce most closely the observed streamflow time series. Table 6.4 lists the monthly averaged discharge modeled at each resolution. While differing average catchment elevations and areas have some effect on the lapsed model precipitation, the differences (see Table 4.1) are too small to account for a significant fraction of the observed variations among the model simulations.

Table 6.4 Monthly averaged discharge at each resolution (mm).

Month	10 m	20 m	30 m	50 m	90 m	200 m
January	1.0	1.3	1.5	2.0	2.5	3.1
February	0.7	0.8	1.1	1.3	1.6	1.9
March	1.4	1.7	2.0	2.3	2.4	2.6
April	1.0	1.2	1.3	1.9	2.5	3.4
May	5.3	5.8	6.4	7.5	7.5	7.6
June	4.0	5.0	7.3	9.0	9.5	9.7
July	6.6	7.9	10.2	13.3	13.1	14.3
August	13.6	12.7	13.4	17.8	18.2	18.1
September	1.9	2.1	2.1	3.4	3.3	3.9
October	2.3	2.8	3.4	4.3	4.2	4.9
November	5.7	6.8	8.3	9.9	10.3	11.0
December	4.8	5.9	7.4	8.8	9.9	10.9
Total	**48.3**	**54.0**	**64.5**	**81.5**	**85.1**	**91.5**

Monthly averaged discharge generally increased with increasing pixel size. The increases were more pronounced at transitions between 10 m and 50 m. However, monthly averages alone are not enough to explain the causes of these differences, i.e. do predictions vary because of differences in (1) the frequency of storm flows, (2) the magnitude of storm flows, and/or (3) the magnitude of base flows?

An examination of the simulated streamflow series (see Appendix B) shows that increased flows occurred for the same precipitation events, regardless of the model resolution. While the *magnitude* of storm flows was strongly dependent on pixel size, the *frequency* of storm flows was not. Therefore the differences in monthly discharge shown in Table 6.4 reflect an increase in the fraction of precipitation events resulting in increased streamflow. While base flow values do vary with pixel size, the total base flow volume in any of the simulations is far too small to influence the discharge values shown above. Instead, the differences in discharge must result from differences in simulated streamflow during storm events. To better characterize the influence of pixel size on model predictions, individual storms have been examined in detail.

Figure 6.5 shows observed and simulated streamflows for a storm in early December, 1978. Storm statistics are shown in Table 6.5. The simulated peak flows and total storm flow volumes for this event were more sensitive to pixel size than the simulated monthly averaged streamflows. Despite heavy precipitation during the preceding month, the catchment soils were unsaturated during this event. However, the precipitation rate was high enough to generate overland flow via the mechanism of infiltration excess. On the receding limb of the hydrograph, infiltration of ponded surface water may have led to a rise in the water table which contributed runoff to the streams after precipitation had stopped, particularly for higher resolution simulations. The calculated recession rates were similar for the 10 - 50 m simulations. The recession rates for the 90 and 200 m simulations were increased because a higher fraction of precipitation was delivered directly to the channel without infiltration, so less water was available for subsurface lateral transport to the channel. The rapid recession at 90 and 200 m may not only reflect a reduction in near-stream infiltration, but also an inability to transport water through the soils to the channel, because of reduced head gradients and longer subsurface path lengths typical for coarser DEMs (see Sections 4.2.3 and 4.2.4). In addition to its steep receding limb, the 200 m simulation streamflows increased more rapidly than at other resolutions. As pixel size is increased, the ratio of overland flow to subsurface flow is increased. The results of the analysis of this storm event suggest that 90 m resolution is too coarse to reproduce both the rising and falling limb of the hydrograph.

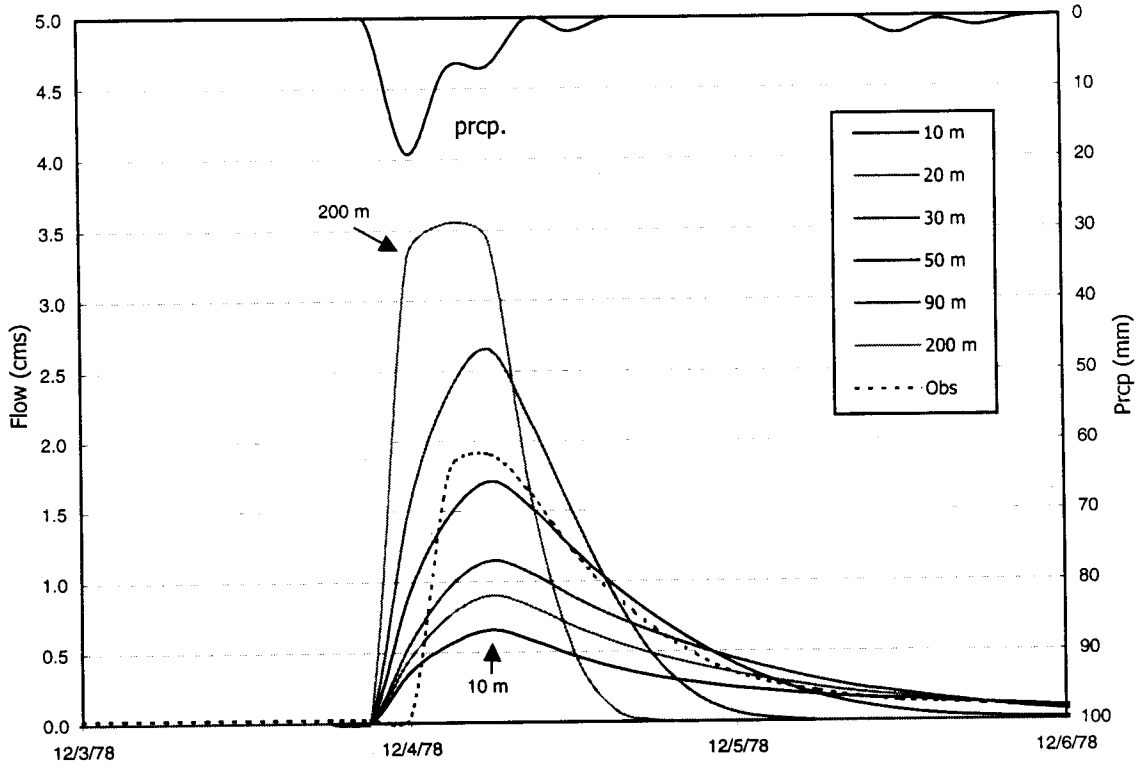

Figure 6.5 Simulated streamflows at 10 to 200 m resolution, December, 1978.

Table 6.5 Simulated streamflow summary for early December, 1978 storm.

	Peak Flow (cms)	Recession Rate K*	Total Storm Volume (1000 m^3)
10 m	0.66	0.942	60
20 m	0.90	0.950	77
30 m	1.15	0.954	95
50 m	1.71	0.939	112
90 m	2.65	0.887	127
200 m	3.55	0.665	135
Observed Flow	1.90	0.921	125

*Recession rates were calculated using $Q_9/Q_0 = K^t$, where Q_0 is the peak flow and Q_9 is the flow 9 hours later.

Under infiltration excess driven conditions, overland flow is routed by DHSVM at a rate of 1 pixel per time step in the direction of steepest descent until encountering a stream, or a pixel that is neither saturated nor holds ponded water. Under these conditions, simulated streamflow is a function of pixel size and stream density, but not slope. When the rainfall rate is higher than the infiltration rate, larger pixels can pond a greater volume of water than smaller pixels, so each pixel has more water available for delivery to streams. It was noted in Section 4.2.4 that stream density deceased for larger pixel sizes, increasing the average distance to a stream channel. For the 200 m DEM, the derived stream density was ~28% lower than that of the 10 m DEM (see Table 4.4). However, because the overland flow is routed by pixels instead of hydraulically by distance, the fraction of pixels located within a few pixels of a stream segment is considerably larger for coarser DEMs relative to the fine DEMs, i.e. the 28% decrease in stream density is more than made up by the 20-fold increase in pixel size, when comparing 10 and 200 m DEMs. For example, if ponded water must travel 180 m to intersect a stream channel, the distance would be covered in 2 to 3 model time steps with a 90 m DEM compared with 18 or 19 time steps with a 10 m DEM. Since heavy, infiltration excess producing, precipitation events do not last more than a few model time steps, precipitation falling 180 m from a stream would not contribute to hydrograph peaks for model runs using a 10 m DEM. However, for a heavy storm lasting approximately 9 hours, the same area would contribute to streamflow for a simulation run at 90 m resolution.

Figure 6.6 shows a schematic representation of the effect of pixel size on overland flow. In the top panel, overland flow is generated by heavy precipitation and moves 2 pixels (in 2 model time steps) towards the stream channel. On the third model time step, precipitation has stopped and the ponded water infiltrates, increasing the soil moisture. In the bottom panel, the length of each pixel is 3 times larger than those in the top panel. The heavy precipitation generates overland flow that reaches the stream channel on the 2^{nd} model time step. Thus a greater fraction of the precipitation falling near the stream is translated directly into streamflow and less infiltrates to the soils. The surface area (and

thus water volume) within 2 pixels of the stream is 3 times larger for the bottom panel. The ratio of peak flows for the 90 m/30 m simulations in the previous example (see Table 6.5) is 2.3 which is close but somewhat less than the ratio calculated from Figure 6.6. The reduction of this ratio is attributable to the decreased stream density at 90 m (see Section 4.2.4) and the increased importance of intercepted subsurface flow for the finer grid.

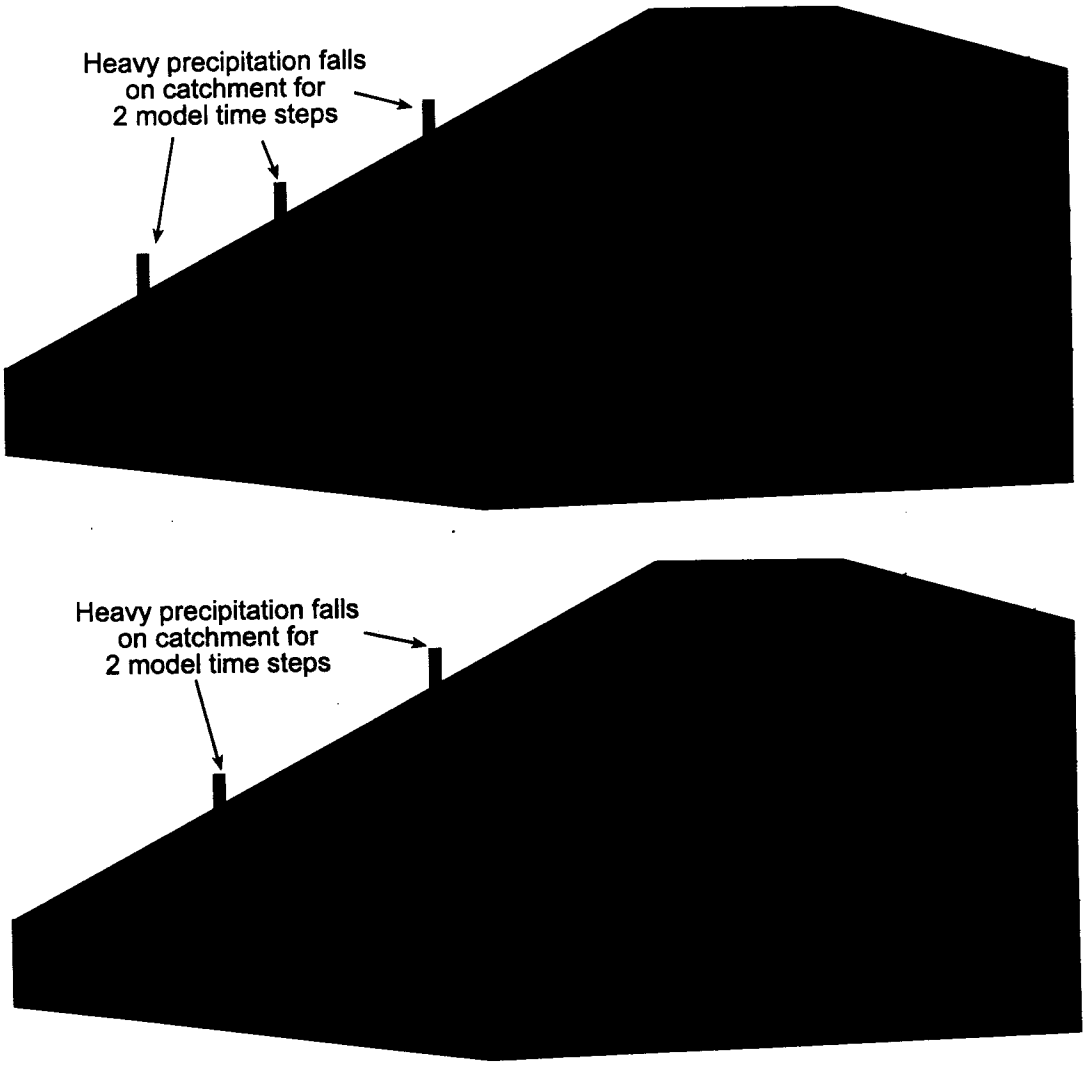

Figure 6.6 Schematic representation of overland flow. Precipitation falls for 2 model time steps. For the larger pixels shown in the bottom panel, water reaches the stream channel via overland flow, while ponded water in the top panel infiltrates after the precipitation stops.

The previous example made clear the effect of pixel size on simulated streamflows when infiltration excess drives hydrologic response, but it was apparent in the observed streamflow record for 1981 that subsurface transport can also be an important mechanism within the Paul Creek catchment[6]. Figure 6.7 and Table 6.6 show the simulated streamflows at each resolution from August 21 to August 26, 1981. This event was chosen because it occurred at the end of the wettest season of the modeling period, so some simulated subsurface transport was expected.

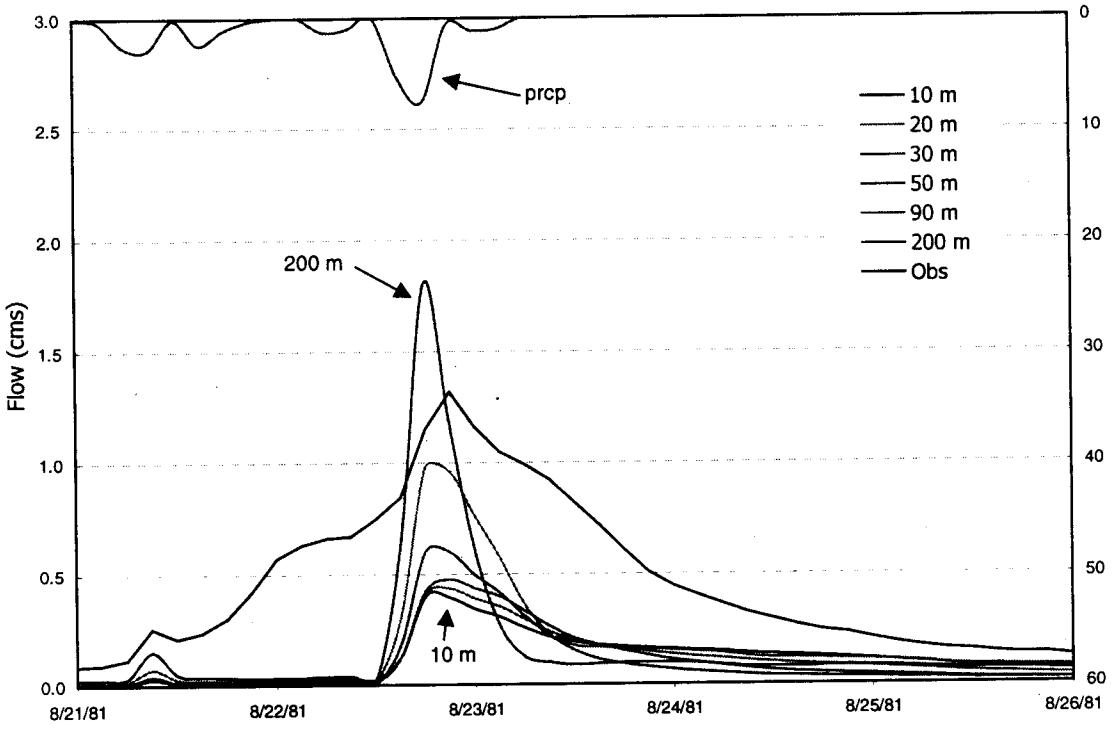

Figure 6.7 Simulated streamflows at 10 to 200 m resolution, August, 1981.

[6] The relative importance of subsurface flow was inferred from the slower observed hydrograph recessions and the relatively higher runoff fraction in August, 1981.

Table 6.6 Simulated streamflow summary for August 21 to 26, 1981.

	Peak Flow (cms)	Recession Rate K	Total Storm Volume (1000 m^3)
10 m	0.40	0.963	51
20 m	0.43	0.972	48
30 m	0.48	0.979	44
50 m	0.60	0.945	42
90 m	0.98	0.919	75
200 m	1.81	0.800	74

The results are generally similar to those in Figure 6.5 and Table 6.5: the peak flows are much higher for the coarse resolution simulations, and the 200 m simulation has a rapid recession. However, the simulated flows for this storm are somewhat less sensitive to pixel size than the December, 1978 event. For example, the 50 m/10 m ratio of simulated peak flow is 1.5 compared with 2.6 for December, 1978. Also, the hydrograph recession at 90 m was more similar to the other resolutions than 90 m simulation of the December, 1978 event. These differences are attributable to the higher catchment soil moisture during the August, 1981 event. As previously stated, the coarser resolution simulations are more resistant to subsurface transport, however the soils were sufficiently wetted for some subsurface flow to contribute to storm flows at all resolutions 90 m and finer.

Figure 6.8 shows the simulated depth to water table for August 23, 1981 at 3 am, the time at which catchment soil moisture was near its peak for this event. As should be expected for a catchment with a low runoff ratio, only precipitation falling near a stream segment, enters the channel and contributes to streamflow at the gauge. Simulations performed at coarser resolutions show shallow water tables that extend farther from stream segments than simulations at finer resolutions. This demonstrates that the effective area contributing to storm flows increases as the pixel size increases (see Figure 6.6). Figure 6-8 also shows that small pixel sizes (30 m or less) are preferable for resolving the water table gradients (see blue and green pixels on eastern side of catchment).

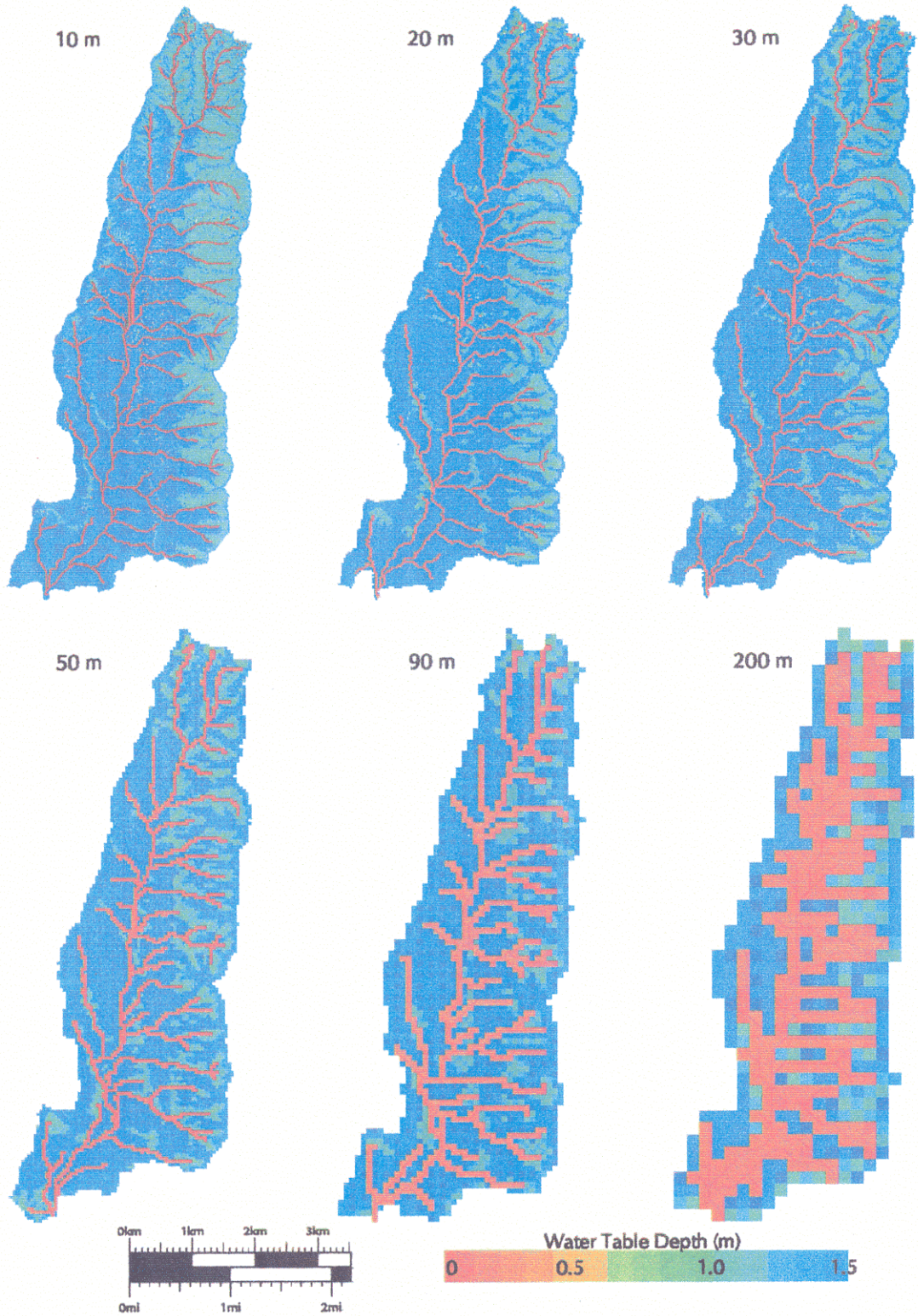

Figure 6-8. Simulated depth to water table (m) on August 23, 1981 at 3:00 am.

These examples clearly establish that under infiltration excess dominated conditions, simulated streamflow is strongly affected by pixel size. The peak storm flows in particular are affected by model resolution. It has also been noted that DHSVM has a relatively simple overland flow routing scheme. Since DHSVM has been applied mostly to humid catchments of the Pacific Northwest where overland flow is rarely observed in non-urban catchments, a more sophisticated overland flow routing scheme had not been necessary. The examination of the August 21 to 26, 1981 storm event suggested that as interception of subsurface flow by the channel becomes more important, the effect of pixel size is reduced. If saturated excess were the dominant mechanism of overland flow production in Paul Creek, then 90 m would probably be an acceptable model resolution. The effect of pixel size on topographic parameters as demonstrated in Chapter 4 implies that even though various model resolutions could be used to reproduce observed streamflows, substantially different model parameter sets would be required to do so.

6.4 EFFECT OF PIXEL SIZE WITH WETTER SOIL CONDITIONS

Results from the previous section indicate that the effects of pixel size become less important as saturation excess flow becomes the dominant runoff mechanism. However, the analyses in Chapter 4 suggested that changes in topographic gradients and topographically defined variables should influence the timing and magnitude of model runoff for saturation excess conditions. For the period of study, the only evidence of sizeable saturation excess flow within the Paul Creek catchment was for August, 1981, and the calibrated model did not reproduce observed flows accurately for this period. In this section, the storm events of August, 1981, have been revisited using a model setup designed to increase the proportion of streamflow fed by channel interception of lateral subsurface flow, while allowing overland flow to develop during heavy rain storms. The initial soil moisture was set to 0.35 uniformly within the catchment, but all other model parameters were unchanged.

Figure 6.9 and Table 6.7 show the simulated response for August 21 to 26, 1981. This is the same storm event examined in Figure 6.7 and Table 6.6. The peak flow and total storm volume at each of the model resolutions were noticeably increased as a result of the wetter soils. In addition, the receding limb of the simulated hydrographs at 90 m resolution and finer were attenuated in comparison with those in Figure 6.7. Both of these observations are an indication that saturation excess played a more significant role in this simulation than in the previous simulation of this event. Unlike the previous simulation, the timing of the hydrograph peaks is strongly affected by model resolution. The 10 m and 200 m resolution models respond the fastest, and the 50 m model responds the slowest. If hydrologic response were not influenced by overland flow, the 10 m simulation would be expected to respond the fastest and the 200 m simulation the slowest. The reversal in peak hydrograph timing suggests there is a change in the dominant runoff mechanism near 50 m resolution: at finer resolutions, the runoff is dominated by saturation excess and/or interception of subsurface flow, and at coarser resolutions, the runoff is dominated by overland flow.

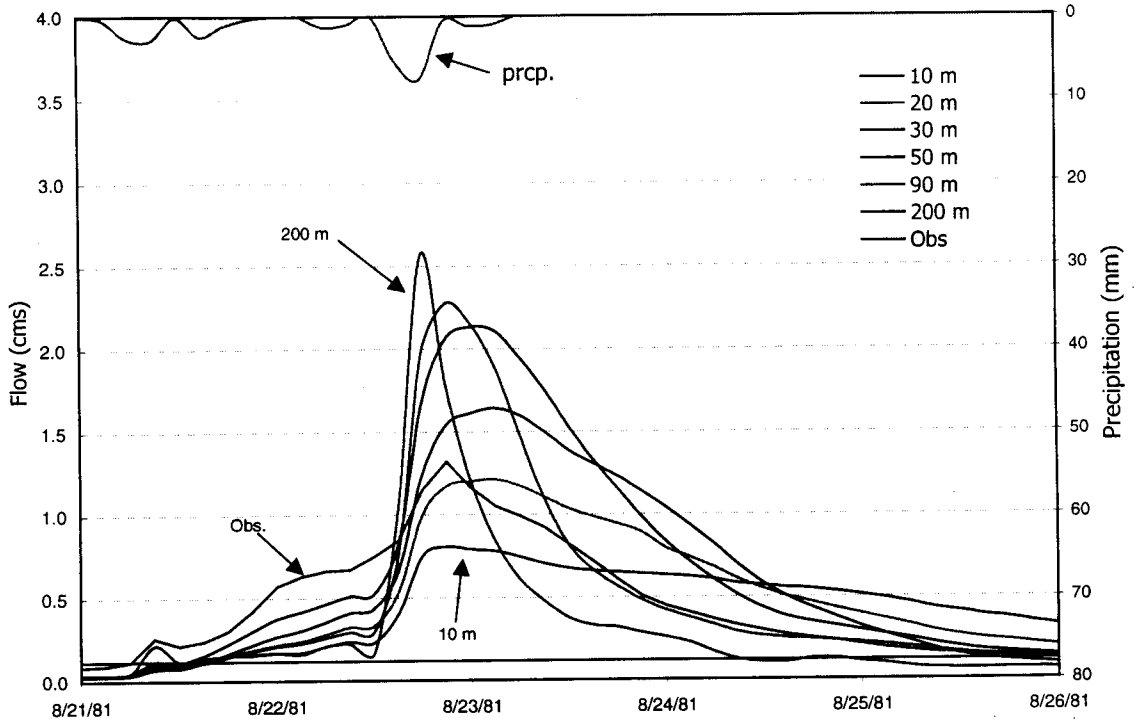

Figure 6.9 Simulated streamflows at 10 to 200 m resolution. Initial soil moisture was set to 0.35 uniformly within the catchment.

Table 6.7 Simulated streamflow summary for August 21 to 26, 1981.

	Peak Flow (cms)	Recession Rate K	Total Storm Volume (1000 m^3)
10 m	0.80	0.989	188
20 m	1.21	0.995	220
30 m	1.64	0.998	261
50 m	2.13	0.987	288
90 m	2.27	0.941	216
200 m	2.57	0.896	145

In conclusion, the model calibration developed from the 1978 and 1979 wet seasons was adequate to reproduce observed streamflows for the 1980 wet season. However, the

above average volume of rainfall in 1981 fell outside the range of calibration data and DHSVM consistently underpredicted the observed flows, particularly for the unusually wet August of 1981. A strong connection was found between pixel size and simulated runoff. The hydrologic response of Paul Creek is characterized by rapid response to precipitation (without saturation of the full soil column) which was modeled as infiltration excess overland flow. Under these conditions, coarse resolution model runs produced higher peak storm flows and total storm flows, although the dependence was somewhat decreased for wet antecedent conditions. In a separate set of model simulations conducted for 1981 with higher initial soil moisture, when saturation excess was the dominant mechanism of runoff production, higher resolution model runs reached peak flow rates faster than coarser resolution simulations, as predicted by the topographic analysis in Chapter 4.

CHAPTER 7: CONCLUSIONS

The past decade has seen advances in the development of spatially distributed, physically based hydrologic models. During this time, wider application of remote sensing technology has expanded the set of available spatial data. Kenward and Lettenmaier (1997) examined the influence of vertical DEM resolution on the predictions of DHSVM at Mahantango Creek, PA. However, with the exception of the aforementioned study, the relationship between topographic data quality and distributed, hydrologic modeling has not been thoroughly investigated.

A primary objective of this study was to test the aircraft-based, interferometric synthetic aperture radar (AirSAR) topographic data collected during the 1996 Pacific Rim mission, for the 21 km^2 Paul Creek and 10.2 Ha Tarrawarra catchments, located near Melbourne in Victoria, Australia. The 10 m AirSAR DEM was tested via comparison with other available topographic products. There was an 3.2 m vertical offset in the AirSAR data relative to the high quality reference DEM collected by Andrew Western and Rodger Grayson of Melbourne University. Once the offset was removed, the (1 σ) vertical error of the AirSAR DEM was ~ 1.3 m. The high frequency, elevation noise evident in the SIR-C DEM of Mahantango Creek, PA (Kenward, et al., 1997) were not apparent in the AirSAR data at Tarrawarra. In addition, the character of the hill slope gradients and ridge lines of Tarrawarra were clearly captured by the AirSAR DEM. Based on the limited analysis at Tarrawarra, the AirSAR DEM was a high quality topographic data set for hydrological studies of the Paul Creek catchment.

The 90 m AUSLIG DEM was offset from the reference DEM at Tarrawarra by only 1.6 m. However the standard deviation of the elevation differences was 4.9 m suggesting the observed errors in the AUSLIG DEM at Tarrawarra were a function of data resolution rather than a vertical bias in the AUSLIG data set. The drainage pattern was also different

for the AUSLIG DEM with flow lines leading to the outlet at the southwest corner rather than the south-central part of the catchment. The AUSLIG DEM was likely too coarse to resolve flow paths properly in areas of low relief.

A series of DEMs up to 200 m pixel size were produced from the 10 m AirSAR DEM using two different approaches to spatial aggregation: bilinear interpolation and a modified-fractal method. A set of geomorphic parameters were examined as a function of pixel size. Based on aggregated and spatial analyses of elevations, slopes, and catchment boundaries, the bilinear interpolation method preserved topographic gradients of the AirSAR DEM better than the modified-fractal method.

As DEMs were aggregated to progressively coarser resolutions, average catchment slopes decreased and the range of slopes (from steepest to flattest) was noticeably reduced. The in-channel flow lengths estimated from DEM-derived stream networks did not vary systematically as a function of pixel size, but drainage density was reduced as pixel size increased, so the effective subsurface path length did increase. Analysis of topographic index values shows higher resolution DEMs have more pixel-to-pixel variability. These investigations of geomorphic parameters suggest that under saturated conditions, the reduced average slopes and increased subsurface path lengths of the coarser DEMs would retard and likely reduce simulated streamflows relative to finer scale model runs. The effect of increasing pixel size on topographic index reduces down slope water movement and may reduce simulated areas of saturation excess compared with model runs at finer resolution.

A series of DHSVM simulations were conducted at resolutions ranging from 10 m to 200 m. All DEMs were produced via bilinear aggregation of the 10 m AirSAR DEM. DHSVM was calibrated using observed flow data from the 1978 and 1979 wet seasons and tested against observed flows from 1980 and 1981. The calibration adequately reproduced the 1980 flow series, but DHSVM consistently underpredicted the observed storm flows during 1981, particularly for the excessively wet August, 1981.

The hydrologic response of Paul Creek is characterized by rapid response to precipitation (without saturation of the full soil column) which was modeled as infiltration excess overland flow. Within DHSVM, ponded water generated by infiltration excess moves from pixel-to-pixel in the direction of steepest decent at a rate of 1 pixel per model time step, with infiltration occurring if the destination pixel does not contain surface water. Under these conditions, coarse resolution model runs produced higher peak storm flows and total storm flows, although the dependence was somewhat decreased for wet antecedent conditions. The extreme dependence of storm flows on pixel size when overland flow dominates hydrologic response suggests that a more sophisticated overland flow algorithm should be incorporated into DHSVM before the model is applied further in similar catchments. With the current model configuration, 90 m resolution is too coarse to represent the hydrologic response of Paul Creek under most conditions. Model simulations of the wettest periods imply that when saturation excess is the dominant mechanism of overland flow production in Paul Creek, then 90 m would probably be an acceptable model resolution.

In a separate set of model simulations conducted for 1981 with higher initial soil moisture, when saturation excess was the dominant mechanism of runoff production, higher resolution model runs reached peak flow rates faster than coarser resolution simulations, as predicted by the topographic analysis. However the increased storm peaks predicted based on topographic analyses were not observed because storm flows were generated by a mixture of saturation excess and infiltration excess mechanisms.

BIBLIOGRAPHY

Abbott, M.B., J.C. Bathhurst, J.A. Cunge, P.E. O'Connell and J. Rasmussen, An introduction to the European hydrological system, - Systeme Hydrologique Europeen, "She", 1: History and philosophy of a physically-based, distributed modelling system, *Journal of Hydrology,* 87, 45-59, 1986.

Anderson, E.A., Development and testing of snowpack energy balance equations, *Water Resources Research*, 4(1), 19-37, 1968.

Beven, K., Changing ideas in hydrology - the case of physically-based models, *Journal of Hydrology*, 105, 157-189, 1989.

Beven, K.J. and M.J. Kirkby, A physically based, variable contributing area model of basin hydrology, *Hydrological Sciences Bulletin*, 24, 43-69, 1979.

Bindlish, R. and A.P. Barros, Aggregation of digital terrain data using a modified fractal interpolation scheme, *Computers and Geoscience*, 22, 907-917, 1996.

Bowling, L. and D.P. Lettenmaier, Evaluation of the effects of forest roads on streamflow in Hard and Ware Creeks, Washington, *Water Resource Series Technical Report*, 155, University of Washington, Seattle, 1997.

Bruneau, P. C. Gascuel-Odoux, P. Robin, P. Merot and K. Beven, Sensitivity to space and time resolution of a hydrological model using digital elevation data, *Hydrological Processes*, 9, 69-81, 1995.

Carter, J.R., Relative errors identified in USGS gridded DEMs, *Auto-Carto 9: Ninth International Symposium on Computer Assisted Cartography*, 255-263, 1989.

Costa-Cabral, M.C. and S.J. Burges, Digital elevation model networks (DEMON): A model of flow over hillslopes for computation of contributing and dispersal areas, Water Resources Research, 30(6), 1681-1692, 1994.

Dawes, R.D., L. Zhang, T.J. Hatton, P.H. Reece, G.T.H. Beale and I. Packer, Evaluation of a distributed parameter ecohydrological model (TOPOG_IRM) on a small cropping rotation catchment, *Journal of Hydrology*, 191, 64-86, 1997.

Dubois, P.C., J.J. van Zyl and E.T. Engman, Measuring soil moisture with imaging radars, *IEEE Transactions on Geoscience and Remote Sensing*, 33, 1995.

Endreny, T.A., E.F. Wood and D.P. Lettenmaier, Satellite-derived digital elevation model accuracy – 1: Geomorphic analysis requirements, *in review*, 1998a.

Endreny, T.A., E.F. Wood and D.P. Lettenmaier, Satellite-derived digital elevation model accuracy – 2: Hydrological modeling requirements, *in review*, 1998b.

Evans, D.L., *Spaceborne aperture radar: Current status and future directions*, NASA Technical Memorandum 4679, 1995.

Evans, D.L., T.G. Farr, J.J. van Zyl and H.A. Zebker, Radar polarimetry: Analysis tools and applications, *IEEE Transactions on Geoscience and Remote Sensing*, 26(6), 774-788, 1988.

Fitch, J.P., *Synthetic aperture radar*, 170 pp., Springer-Verlag, New York, 1988.

Fread, D.L., Chapter 10: Flow Routing, in *Handbook of Hydrology*, D.R. Maidment ed., McGraw-Hill, New York, 1993.

Garbrecht, J. and L. Martz, Grid size dependency of parameters extracted from digital elevation models, *Computers and Geoscience*, 20, 85-87, 1994.

Garrote, L., R.L. Bras, A distributed model for real-time flood forecasting using digital elevation models, Journal of Hydrology, 167, 279-306, 1995.

Giacomelli, A., U. Bacchiega, P.A. Troch and M. Mancini, Evaluation of surface soil moisture distribution by means of SAR remote sensing techniques and conceptual hydrological modelling, *Journal of Hydrology*, 166, 445-459, 1995.

Goodrich, D.C., L.J. Lane, R.M. Shillito, S.N. Miller, K.H. Syed and D.A. Woolhiser, Linearity of basin response as a function of scale in a semiarid watershed, *Water Resources Research*, 33(12), 2951-2965, 1997.

Grayson, R.B., I.D. Moore and T.A. McMahon, Physically based hydrologic modeling 1. A terrain-based model for investigative purposes, *Water Resources Research,* 28(10), 2639-2658, 1992.

Grayson, R.B., I.D. Moore and T.A. McMahon, Physically based hydrologic modeling 2. Is the concept realistic?, *Water Resources Research*, 26(10), 2659-2666, 1992.

Gyasi-Agyei, Y., G. Willgoose and F.P. de Troch, Effects of vertical resolution and map scale of digital elevation models on geomorphological parameters used in hydrology, *Hydrological Processes*, 9, 363-382, 1995.

Harding, D.J., *SLICER: Scanning LIDAR imager of canopies by echo recovery instrument and data product description*, Draft: SLICER Instrument and Data Product Description, 1998.

Hutchinson, M.F. and P.E. Gessler, Splines - more than just a smooth interpolator, *Geoderma*, 62, 45-67, 1994.

Ichoku, C., A. Karnieli and I. Verchovsky, Application of fractal techniques to the comparative evaluation of two methods of extracting channel networks from digital elevation models, *Water Resources Research*, 32(2), 389-399, 1996.

Kenward, T. and D.P. Lettenmaier, Assessment of required accuracy of digital elevation data for hydrologic modeling, *Water Resource Series Technical Report*, 153, University of Washington, Seattle, 1997.

Lillesand, T.M. and R.W. Kiefer, *Remote sensing and image interpretation*, 2nd ed., John Wiley and Sons, 750 pp., 1994

Lin, D.S., E.F. Wood, K. Beven and S. Saatchi, Soil moisture estimation over grass-covered areas using AirSAR, *International Journal of Remote Sensing*, 15(11), 2323-2343, 1994.

Maher J.M., *An agricultural land use capability survey of the Yarra Glen area*, 44 pp., Research Project Series No. 65, Government of Victoria, 1952.

Montgomery, D.R. and E. Foufoula-Georgiou, Channel network source representation using digital elevation models, *Water Resources Research*, 29(12), 3925-3934, 1993.

Moore, I.D., R.B. Grayson and A.R. Ladson, Digital terrain modelling: A review of hydrological, geomorphological, and biological applications, *Hydrological Processes*, 5, 3-30, 1991.

Myers, B.J., S. Theiveyanathan, N.D. O'Brien and W.J. Bond, Growth and water use of Eucalyptus grandis and Pinus radiata plantations irrigated with effluent, *Tree Physiology*, 16, 211-219, 1996.

Pierce, L.E., F.T. Ulaby, K. Sarabandi and M.C. Dobson, Knowledge-based classification of polarimetric SAR images, *IEEE Transactions on Geoscience and Remote Sensing*, 32(5), 1081-1086, 1994.

Quinn, P., K. Beven, P. Chevallier and O. Planchon, The prediction of hillslope flow paths for distributed hydrological modelling using digital terrain models, *Hydrological Processes*, 5, 59-79, 1991.

Quinn, P.F., K.J. Beven and R. Lamb, The ln(a/tan b) index: How to calculate it and how to use it within the TOPMODEL framework, *Hydrological Processes*, 9, 161-182, 1995.

Rawls, W.J., L.R. Ahuja, D.L. Brakensiek and A. Shirmohammadi, Chapter 5: Infiltration and soil water movement, in *Handbook of Hydrology*, D.R. Maidment ed., McGraw-Hill, New York, 1993.

Refsgaard, J.C., Parameterisation, calibration and validation of distributed hydrological models, *Journal of Climate*, 198, 69-97, 1997.

Rich, P.M., W.A. Hetrick and S.C. Saving, *Modeling topographic influences on solar radiation: A manual for the SOLARFLUX model*, 33 pp., Los Alamos National Laboratory, Los Alamos, NM, 1995.

Roden, J.S. and M.C. Ball, The effect of elevated [CO_2] on growth and photosynthesis of two eucalyptus species exposed to high temperatures and water deficits, *Plant Physiology*, 111, 909-919, 1996.

Saulnier, G.M., K. Beven and C. Obled, Digital elevation analysis for distributed hydrological modelling: Reducing scale dependence in effective hydraulic conductivity values, *Water Resources Research*, 33(9), 2097-2101, 1997.

Seyfried, M.S. and B.P. Wilcox, Scale and the nature of spatial variability: Field examples having implications for hydrologic modeling, *Water Resources Research*, 31(1), 173-184, 1995.

Shuttleworth, W.J., Chapter 4: Evaporation, in *Handbook of Hydrology*, D.R. Maidment ed., McGraw-Hill, New York, 1993.

Stoneman, G.L., D.S. Crombie, K. Whitford, F.J. Hingston, R. Giles, C.C. Portlock, J.H. Galbraith and G.M. Dimmock, Growth and water relations of Eucalyptus marginata

(jarrah) stands in response to thinning and fertilization, *Tree Physiology,* 16, 267-274, 1996.

Storck, P., D.P. Lettenmaier, B.A. Connelly and T.W. Cundy, *Implications of forest practices on downstream flooding*, Phase II report to Water Forest Protection Association, King County Surface Water Management Division, Weyerhauser Co., and U.S. Forest Service, University of Washington, 1995.

Storck, P., L.Bowling, P. Wetherbee and D.P. Lettenmaier, Application of a GIS-based distributed hydrology model for prediction of forest harvest effects on peak storm flow in the Pacific Northwest, Hydrological Processes, 12, 889-904, 1998

Tarboton, D.B., R.L. Bras and I. Rodriguez-Iturbe, On the extraction of channel networks from digital elevation data, *Hydrological Processes*, 5, 81-100, 1991.

Treuhaft, R.N., S.N. Madsen, M. Moghaddam and J.J. van Zyl, Vegetation characteristics and underlying topography from interferometric radar, Radio Science, 31(6), 1449-1485, 1996.

van Zyl, J.J. H.A. Zebker and C. Elachi, Imaging radar polarization signatures: Theory and observation, *Radio Science*, 22(4), 529-543, 1987.

Vertessy, R.A., R.G. Benyon, S.K. O'Sullivan and P.R. Gribben, Relationships between stem diameter, sapwood area, leaf area and transpiration in a young mountain ash forest, *Tree Physiology*, 15, 559-567, 1995.

Western A.W. and R.B. Grayson, The Tarrawarra data set: Soil moisture patterns, soil characteristics and hydrological flux measurements, *Water Resources Research*, in review, 1998.

Wigmosta, M.S., L.W. Vail and D.P. Lettenmaier, A distributed hydrology-vegetation model for complex terrain, *Water Resources Research*, 30(4), 1665-1679, 1994.

Wolock, D.M. and C.V. Price, Effects of digital elevation model map scale and data resolution on a topography-based watershed model, Water Resources Research, 30(11), 3041-3052, 1994.

Wood, E.F., M. Sivapalan, K. Beven and L. Band, Effects of spatial variability and scale with implications to hydrologic modeling, *Journal of Hydrology*, 102, 29-47, 1988.

Woods, R.A. and M. Sivapalan, A connection between topographically driven runoff generation and channel network structure, *Water Resources Research*, 33(12), 2939-2950, 1997.

Zebker, H.A., J.J. van Zyl, S.L. Durden and L. Norikane, Calibrated imaging radar polarimetry: Technique, examples, and applications, *IEEE Transactions on Geoscience and Remote Sensing*, 29(6), 942-960, 1991.

Zebker, H.A., S.N. Madsen, J. Martin, K.B. Wheeler, T. Miller, Y. Lou, G. Alberti, S. Vetrella and A. Cucci, The TOPSAR Interferometric radar topographic mapping instrument, *IEEE Transactions on Geoscience and Remote Sensing*, 30(5), 1992.

Zhang, W. and D.R. Montgomery, Digital elevation model grid size, landscape representation, and hydrologic simulations, *Water Resources Research*, 30(4), 1019-1028, 1994.

APPENDIX A: SPATIAL VARIABILITY OF SOIL AND VEGETATION CHARACTERISTICS

The coarse resolution of commonly available soil and vegetation data does not reflect a lack of field-scale variability. To the contrary, the characteristics of both have been shown to vary on very small scales. Seyfried and Wilcox (1996) provide field examples of sources of hydrologic variability occurring over scales ranging from centimeters to kilometers. For example, they observed changes in soil characteristics in a sage brush environment where soils beneath plants are loose and quickly drain, while soils between plants are hard crusted with much lower infiltration rates. This example illustrates how surface hydrologic characteristics can vary at spatial scales as small as 1 m, or less.

The difficulty in relating hydrologic model parameters to measurable physical quantities has been noted by several investigators (Beven, 1989; Grayson et al., 1992b). Two general concerns have been raised. Physically based models require a much larger amount of field data for model initialization than lumped-parameter models and purely stochastic models. Spatial coverage of measured field parameters is frequently sparse or absent – certainly much coarser than typical model resolution. Second, the relationship between point-scale field measurements and the effective values required by models is not well understood. Even a finely spaced series of point measurements requires interpolation, but if the scale of spatial variability is finer than the spacing of measurements, the interpolated areal value very possibly will not provide a good estimate of the effective value required by a model. If model parameters are poorly related or unrelated to observable quantities, the physical significance of model parameters is lost and physical models behave like more complex (and cumbersome) versions of lumped-parameter models. Interpolation methods are arguably appropriate to relate some variables (soil depth, leaf area index) to useable scales. However, the difficulty is more

serious for variables that must be based on sparsely spaced point measurements (precipitation, hydraulic conductivity, infiltration rate).

Perhaps the most common problem of spatial variability in hydrology is the heterogeneity in the hydraulic properties of soils in the field as compared with a classical soil matrix. Soils with sparsely spaced soil pipes (macropores) can discharge significantly more water than a matrix soil with the same spatially averaged hydraulic conductivity (Nieber and Warner, 1992). Under carefully controlled field conditions, Western and Grayson (1998) observed spatial trends in soil properties but also significant deviation between saturated hydraulic conductivity measurements spaced only 5 m apart. In rare circumstances where measurements exist at such scales, the area of coverage is generally very limited. The scale of spatial variability makes accurate determination of effective hydraulic conductivity unlikely for the scale at which digital topographic data are available. An alternative approach to exhaustive field data collection is required to arrive at an effective hydraulic conductivity for use in physical hydrology models. In previous applications of distributed hydrology models, hydraulic conductivity has been treated in a semi-distributed manner with a single value being used to characterize large areas if not an entire catchment (Kenward and Lettenmaier, 1997; Bowling and Lettenmaier, 1997; Refsgaard, 1997). In catchments where saturation excess is the primary mechanism for surface flow generation, lateral hydraulic conductivity in large part controls the timing of the outlet hydrograph, and to a lesser degree the partitioning of sub-surface moisture. Since predicted discharge is very sensitive to lateral hydraulic conductivity, this quantity is effectively varied to optimally reproduce the observed streamflow. Even though effective saturated conductivity retains only a tenuous connection to measurable field data values, it nonetheless can vary strongly with model spatial resolution. Using TOPMODEL simulations, Saulnier et al. (1997) observed a marked increase in calibrated saturated conductivity values as pixel size increased. These changes were interpreted as a way for the model to compensate for the tendency of individual pixels to accumulate rather than distribute water. Pixels tended to accumulate more water because the

aggregation process flattens topographic gradients that drive moisture distribution. These problems are related to the difficulty of relating field-scale measurements to pixel-scale effective values. Since variations in soils characteristics may occur on the order of 1 m, sub-grid variability is similarly difficult to quantify with 10 m and 100 m pixels. Since soil parameters typically are not well known, they are often treated as calibration parameters used to optimize the agreement between observed and simulated streamflows.

APPENDIX B: SIMULATED STREAMFLOWS FROM 10 TO 200 M RESOLUTION

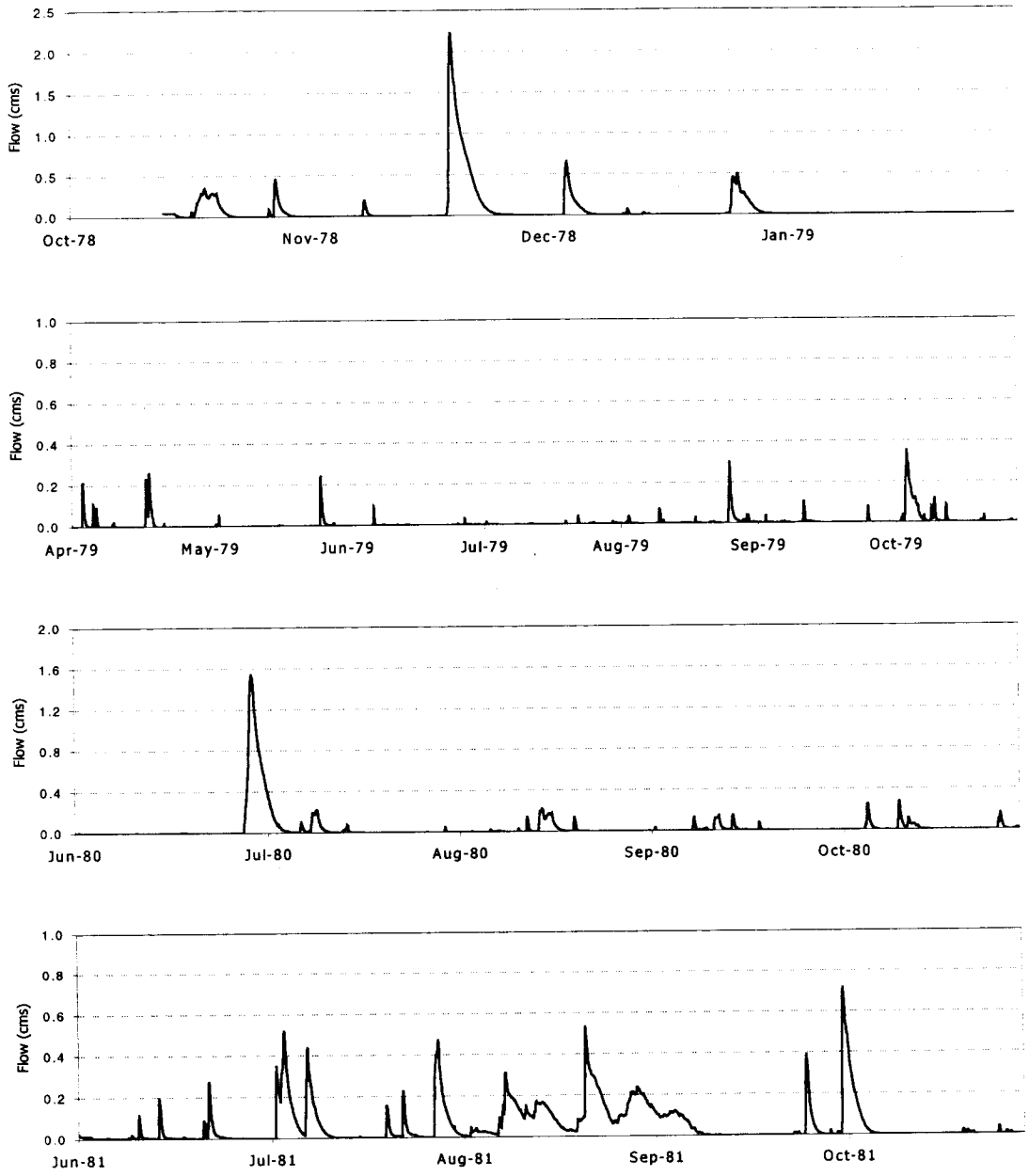

Figure B.1 DHSVM simulated streamflows at 10 m resolution.

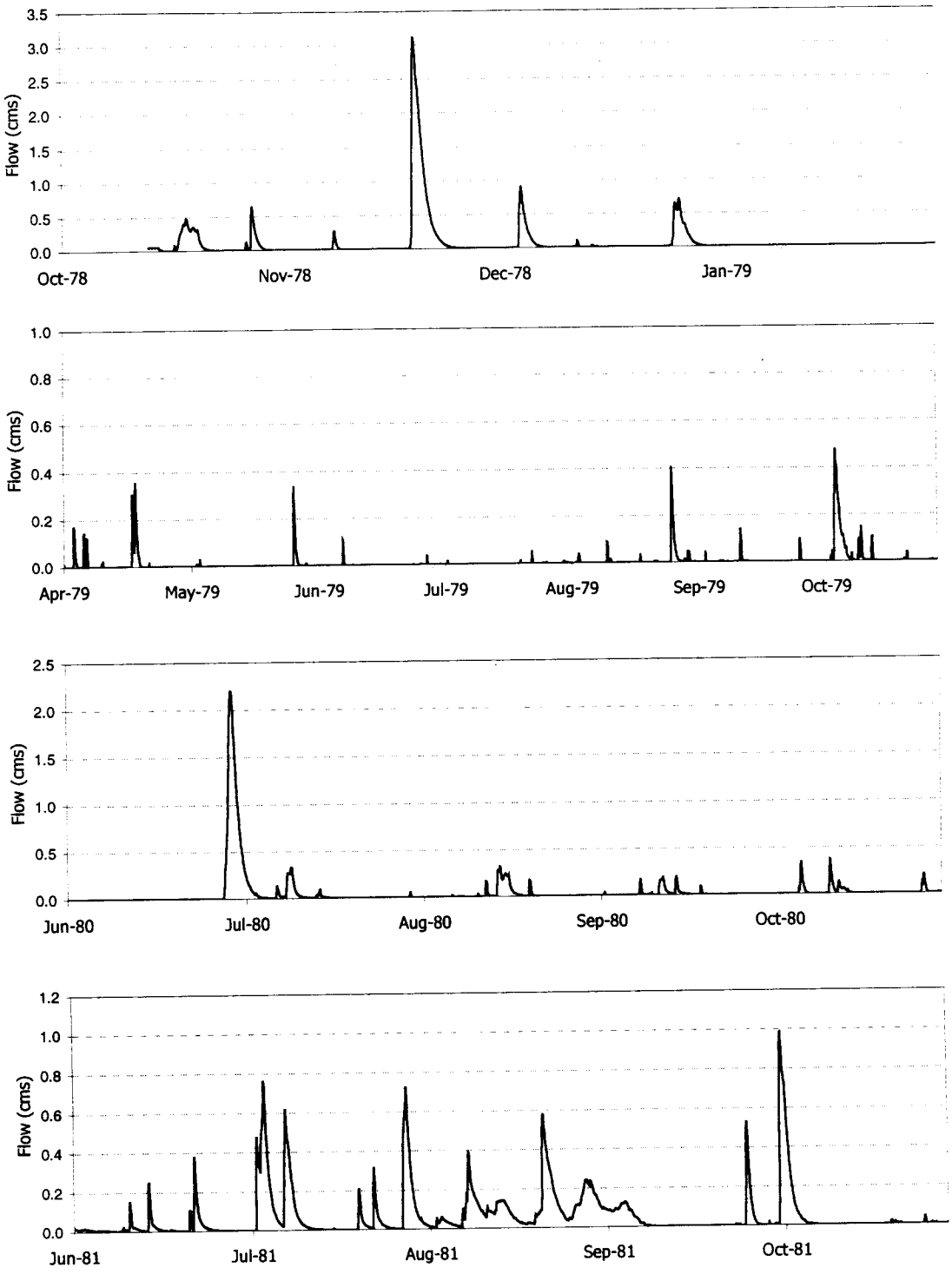

Figure B.2 DHSVM simulated streamflows at 20 m resolution.

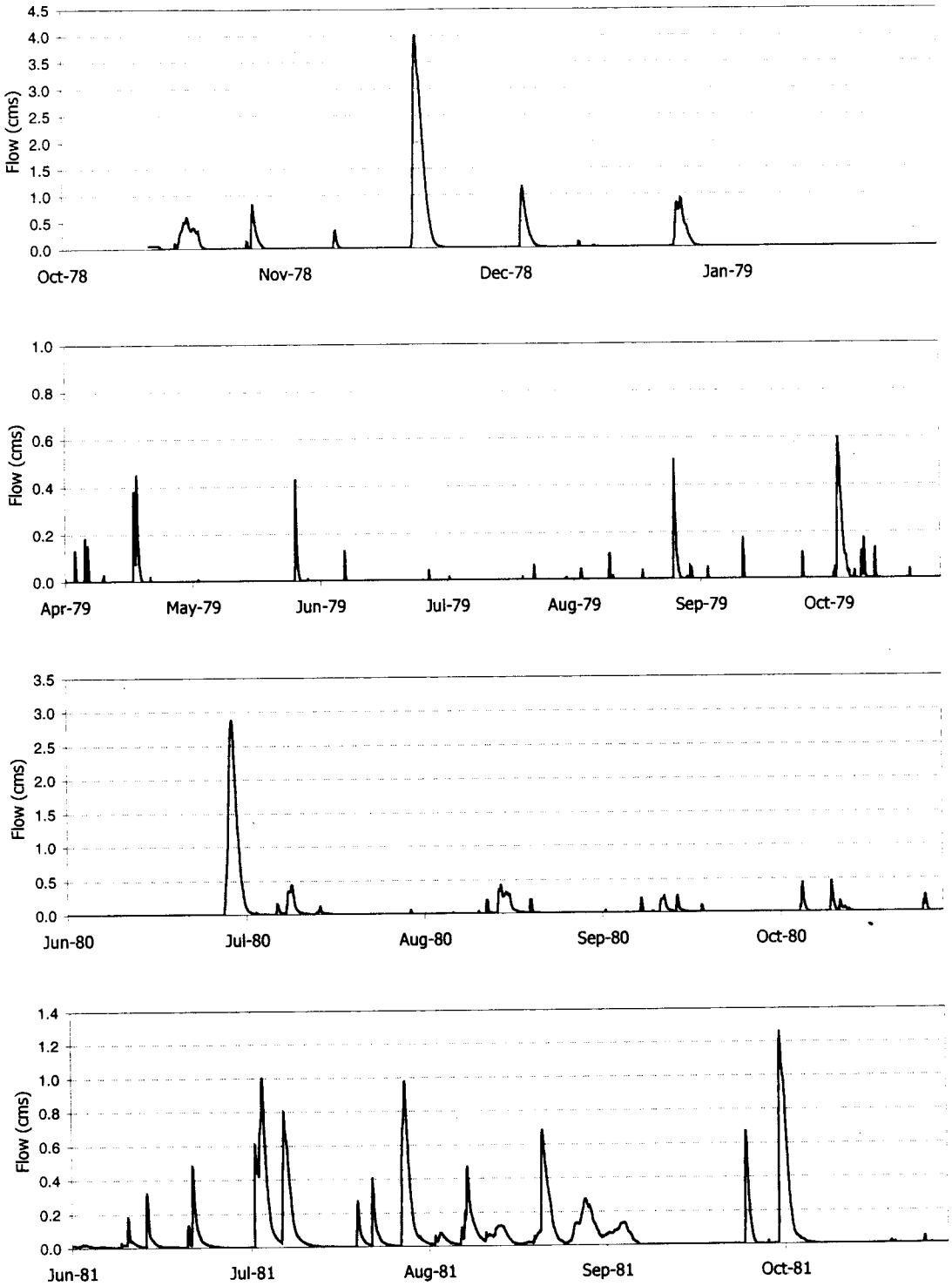

Figure B.3 DHSVM simulated streamflows at 30 m resolution.

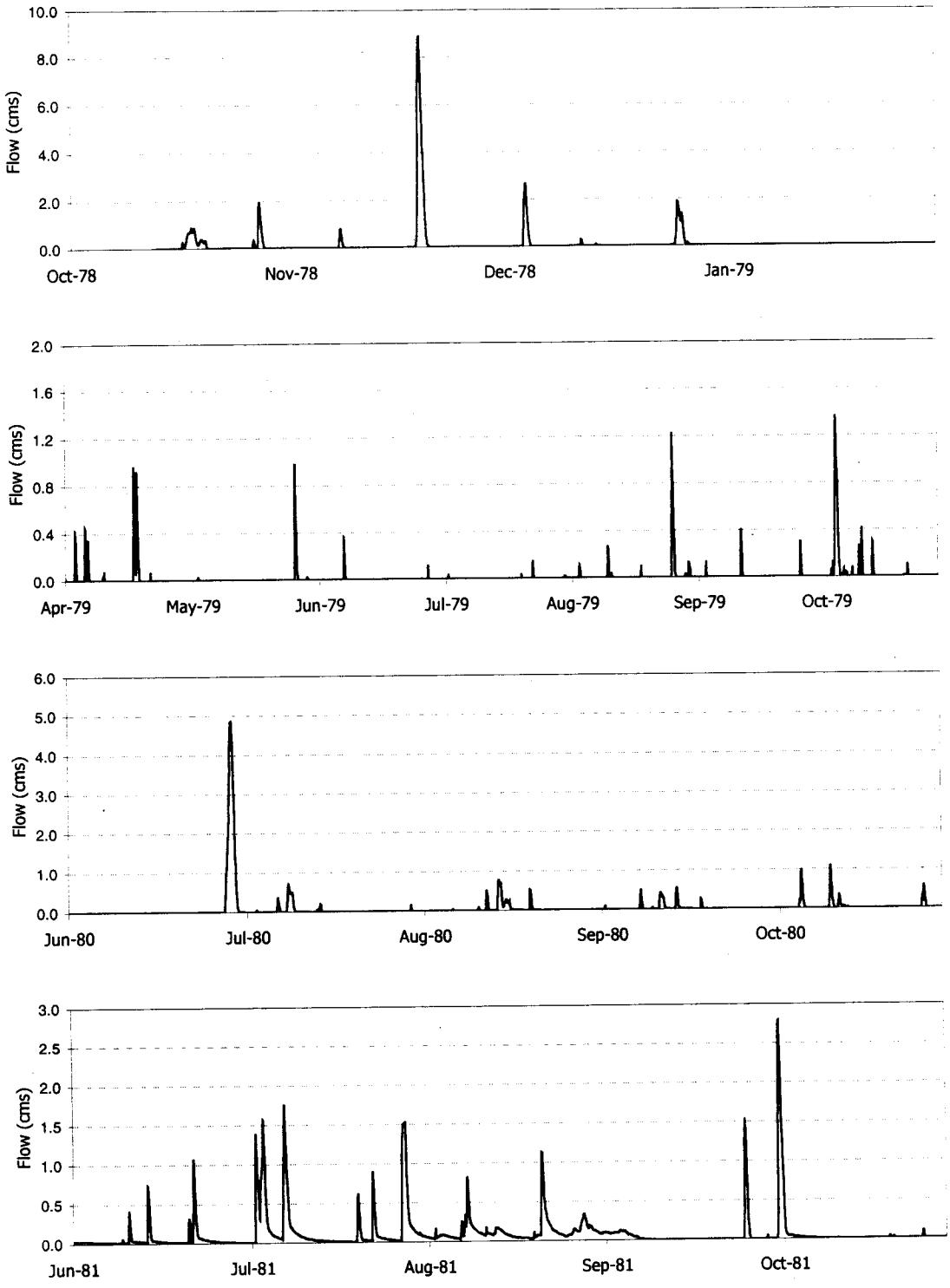

Figure B.4 DHSVM simulated streamflows at 90 m resolution.

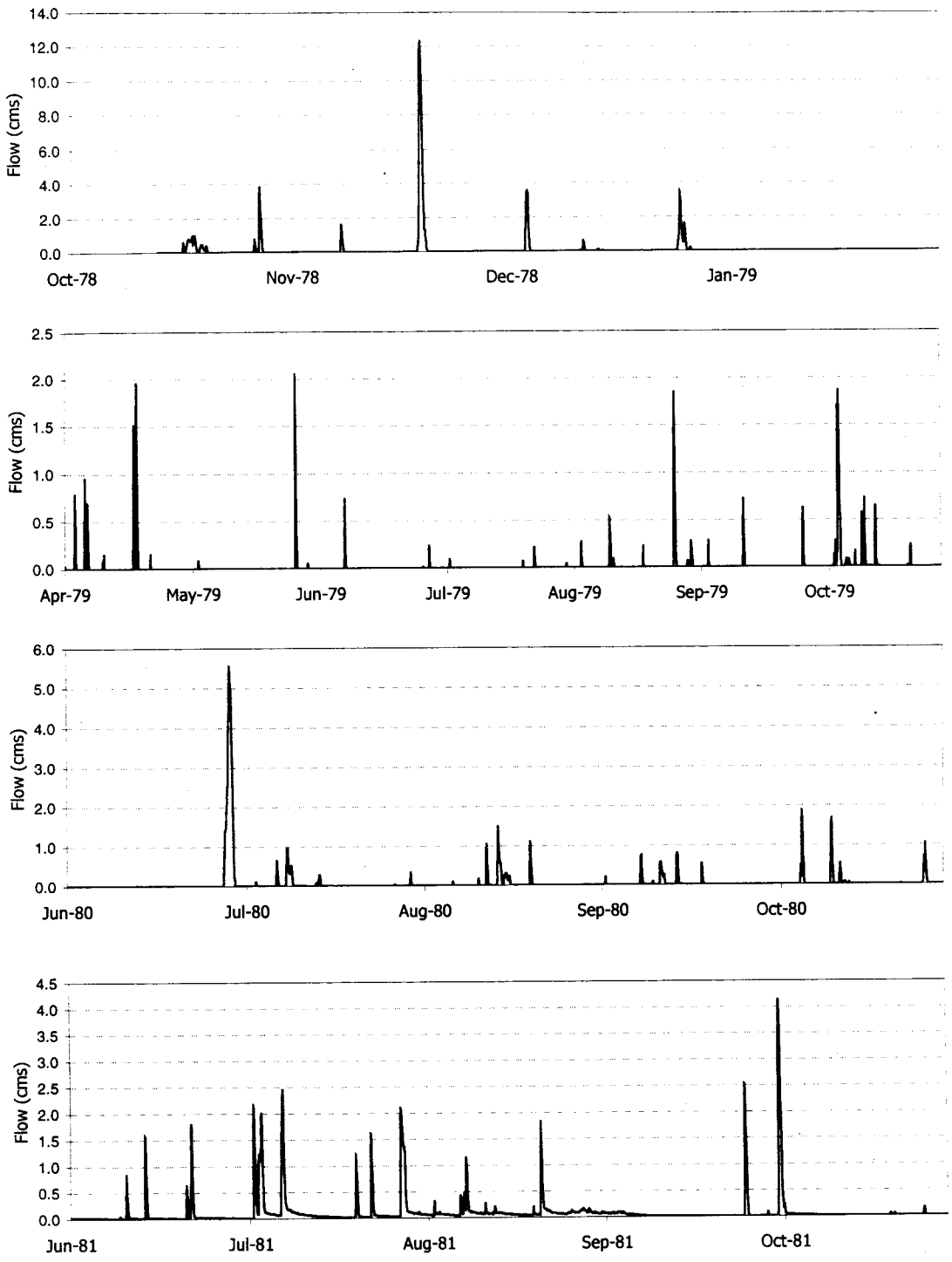

Figure B.5 DHSVM simulated streamflows at 200 m resolution.